Development and Application of Operando Spectroscopy for Vanadium Oxide Catalysts in ODH Reactions: A Comparison of O2 and CO2 as Oxidising Agents

Rogg, Simone Erika

(2020)

DOI (TUprints): https://doi.org/10.25534/tuprints-00011891

Publikationstyp: Ph.D. Thesis

Fachbereich: 07 Department of Chemistry

Quelle des Originals: https://tuprints.ulb.tu-darmstadt.de/11891

Development and Application of Operando Spectroscopy for Vanadium Oxide Catalysts in ODH Reactions: A Comparison of O_2 and CO_2 as Oxidising Agents

Entwicklung und Anwendung der Operando Spektroskopie an Vanadiumoxidkatalysatoren in ODH Reaktionen: Ein Vergleich von O_2 und CO_2 als Oxidationsmittel
Vom Fachbereich Chemie der Technischen Universität Darmstadt zur Erlangung des Grades
Doctor rerum naturalium (Dr. rer. nat.)
Dissertation von M. Sc. Simone Erika Rogg aus Würzburg

1. Gutachten: Prof. Dr. Christian Hess
2. Gutachten: Prof. Dr. Dipl.-Kfm. Bastian J. M. Etzold

Darmstadt 2020

TECHNISCHE
UNIVERSITÄT
DARMSTADT

Fachbereich Chemie
Eduard-Zintl-Institut für Anorganische und Physikalische Chemie

Development and Application of Operando Spectroscopy for Vanadium Oxide Catalysts in ODH Reactions: A Comparison of O_2 and CO_2 as Oxidising Agents
Entwicklung und Anwendung der Operando Spektroskopie an Vanadiumoxidkatalysatoren in ODH Reaktionen: Ein Vergleich von O_2 und CO_2 als Oxidationsmittel

Dissertation von M. Sc. Simone Erika Rogg aus Würzburg

1. Gutachten: Prof. Dr. Christian Hess
2. Gutachten: Prof. Dr. Dipl.-Kfm. Bastian J. M. Etzold

Tag der Einreichung: 4. Mai 2020
Tag der mündlichen Prüfung: 15. Juni 2020

Darmstadt 2020

Bitte zitieren Sie dieses Dokument als:
URN: urn:nbn:de:tuda-tuprints-118917
URL: https://tuprints.ulb.tu-darmstadt.de/11891

Erklärung zur Dissertation

Ich erkläre hiermit, dass ich meine Dissertation selbstständig und nur mit den angegebenen Hilfsmitteln angefertigt und noch keinen Promotionsversuch unternommen habe.

Darmstadt, den 4. Mai 2020

(S. Rogg)

Erklärung der Übereinstimmung

Ich erkläre hiermit, dass die elektronische Version der Doktorarbeit mit der schriftlichen Version übereinstimmt. Die elektronische Version liegt dem Prüfungssekretariat vor.

Darmstadt, den 4. Mai 2020

(S. Rogg)

Scientific contributions

Publications

A. Ott, S. Rogg, S. Lauterbach, H. Kleebe, C. Hess, G. Mera, Novel 0D-Nanocarbon-Based Silica Ceramic Composites: Sol-Gel- Based Synthesis and High-Temperature Evolution, **submitted**

P. Ober*, S. Rogg*, C. Hess, Direct Evidence for Active Support Participation in Oxide Catalysis: Multiple *Operando* Spectroscopy of VO_x/Ceria, *ACS Catal.* **2020**, *10*, 2999–3008.

P. Ruff, L. Schumacher, S. Rogg, C. Hess, Atomic Layer Deposition-Assisted Synthesis of Embedded Vanadia Catalysts, *ACS Catal.* **2019**, *9*, 6349.

Presentations

S. Rogg, M. Mathes, C. Hess, The structural dynamics of supported vanadia catalysts: a comparative study of CO_2 and O_2 during propane ODH by using *operando* UV Raman spectroscopy.

17th International Conference on Carbon Dioxide Utilization, Aachen, Germany, **2019**

S. Rogg, P. Waleska, P. Ober, C. Hess, Targeted Resonance Raman spectroscopy on supported vanadia catalysts during ODH reactions.

51. Katalytikertagung, Weimar, Germany, **2018**

Poster

S. Rogg, M. Mathes, P. Waleska, C. Hess, Elucidating the structure of supported vanadia catalysts during ethanol and propane ODH using *operando* UV Raman spectroscopy.

14th European Congress on Catalysis, Aachen, Germany, **2019**

S. Rogg, P. Waleska, P. Ober, C. Hess, Targeted Resonance Raman spectroscopy on supported vanadia catalysts during ODH reactions.

51. Katalytikertagung, Weimar, Germany, **2018**

---

* Both authors contributed equally

Acknowledgment

My sincere thanks go to Prof. Dr. Christian Hess, who gave me the opportunity to do my research work in his group. I would like to thank him for his belief in me throughout the entire time. He helped me not only in scientific and technical questions, but took also care of my professional and personal development. I would like to thank him for having given me the opportunity to attend various conferences, events, and seminars. He encouraged me to join the 17th International Conference on Carbon Dioxide Utilization as these topics have attracted my particular interest. The experiences and insights obtained during the PhD will accompany me in my future.

I would like to thank my predecessor, Philipp Waleska, who introduced me into the setup and its individual measurement devices. He provided me the necessary knowledge to initiate my project. Due to his empathy, commitment, and helpfulness, he facilitated my entry.

Moreover, I would like to take the opportunity to thank my bachelor's and master's students, whom I supervised during their theses or internship, Patrick Ober, Moritz Mathes, Leon Schumacher, and Filip Rivic. The order represents the temporal sequence. Their dedication was outstanding. I could not only learn with them but also from them. I am glad that Patrick Ober and I have achieved a joint scientific contribution. Especially, I would like to mention Leon Schumacher, who, in addition, has been my graduate assistant. He has never lost courage in case of any technical problem. I am very grateful to have him as my successor, and I wish him great success in his scientific work.

I would like to thank my colleagues, Anastasia Filtschew, Christian Schilling, Philip Ruff, Marcel Heber, Sebastian Berka, Jun Shen, Marc Ziemba, and Jakob Weyel. They not only supported me in technical issues, but also emotionally. Moreover, I would like to mention Karl Kopp, our technical assistant. Without his skills, knowledge, and experience, I would not have accomplished my technical implementations. Many thanks also go to Claudia Jochem, who is the soul of our group. I have really enjoyed the time working in our research group, and I will also look back on great moments in our leisure time.

Furthermore, I would like to thank Mr Hofmann from Agilent Technologies, Inc., who helped me with the installation of the gas chromatograph. My further progress with the new device can be attributed to Martin Lucas, research group Rose. I would like to thank him for his help and time. In this context, I would also like to mention the financial support of the Deutsche Forschungsgemeinschaft (DFG), which enabled the acquisition of the gas chromatograph. In addition, I would like to thank Silvio Heinschke, research group Schneider, who performed the BET measurements.

The TU Darmstadt is a great work place. It provides a lot of seminars and trainings, especially for PhD students.

Finally, I would like to thank my friends, my family, and my husband, Francisco. Their emotional support gave me a lot of strength, energy, and love.

Zusammenfassung

Die oxidative Dehydrierung (ODH) stellt eine attraktive Route für die Herstellung von Propylen dar, um dessen steigende Nachfrage bedienen zu können. Aufgrund der Folge- und Paralleloxidation von Propan wurden bisher nur geringe Propylen-Selektivtäten erzielt. Diese Arbeit beinhaltet die Entwicklung und Anwendung verschiedener *operando*-Techniken mit dem Ziel, molekulare Struktur-Aktivitäts-/Selektivitätsbeziehungen von Vanadiumoxidkatalysatoren in ODH-Reaktionen aufzudecken.

Es wurde ein neues *operando*-Gaschromatograph/Fourier-Transformations-Infrarot-Spektroskopie (GC/FT-IR) Experiment aufgebaut, welches mit der Multiwellenlängen-Ramanspektroskopie (256,7 nm, 385 nm und 515 nm) kombiniert wurde. Der *operando* Aufbau ist, meines Wissens nach, der Erste seiner Art. Um mögliche lokale Überhitzungen und laserinduzierte Probenschäden zu vermeiden, wurde die Wirbelbettmethode etabliert, mit der die Probe während der Messung kontinuierlich durchmischt wird. Laserinduzierte Effekte spielen insbesondere bei der Anregung im ultravioletten (UV) Bereich eine bedeutende Rolle. Im Vorfeld der *operando* Experimente wurden die kommerziellen *in situ/operando* Reaktoren hinsichtlich ihres Einsatzes bewertet. Dabei wurde insbesondere der Temperaturgradient entlang des Reaktorbettes der Raman Zelle untersucht. Der Temperaturcontroller wird über ein integriertes Thermoelement geregelt, welches allerdings nicht im direkten Kontakt mit der Probe ist. Um einen Zusammenhang zwischen der eingestellten Temperatur und der Probentemperatur herzustellen, wurde diese mithilfe eines externen Thermoelements entlang des Reaktorbettes für einen gewissen Temperaturbereich bestimmt. Eine selbstgemachte Halterung diente zur Fixierung des Thermoelements und ermöglichte die Messungen in der geschlossenen Zelle unter Gasfluss und im Wirbelbettmodus. Der Aufbau wurde anschließend in der ODH von Propan mit einem siliziumdioxidgeträgerten Vanadiumoxidkatalysator getestet.

Der Katalysator zeigt katalytische Aktivität bei Temperaturen >300°C, wobei die Selektivität zu Propylen mit steigendem Umsatz fällt. Für die *operando* Versuche wurde eine Reaktionstemperatur von 502°C gewählt. Dabei stimmen Umsatz und Selektivität mit Werten aus der Literatur überein, die in einem konventionellen Reaktor unter ähnlichen experimentellen Bedingungen ermittelt wurden. Dies qualifiziert den Aufbau mitsamt der Raman Zelle und der Wirbelbettmethode für den *operando* Einsatz (d.h. die simultane Aufnahme von spektroskopischer Information und Aktivitätsdaten) und liefert zusätzlich eine Bestätigung für die Temperaturkorrektur.

Der experimentelle Ansatz beinhaltet die Anwendung der Multiwellenlängen-Raman-, Diffuse-Reflexions-UV-Vis und Diffuse-Reflexions-Infrarot-Fourier-Transformations-Spektroskopie. Da beim Umschalten von oxidativen zu reaktiven Bedingungen keine großen strukturellen Veränderungen beobachtbar sind, wird die erste C-H Aktivierung als geschwindigkeitsbestimmender Schritt identifiziert. In der Abwesenheit von Sauerstoff wird der Katalysator stark reduziert, wie anhand der UV-Vis Spektroskopie gezeigt werden kann. Die Raman Spektren bei einer Anregungswellenlänge von 515 nm enthalten aufgrund der hohen Eigenabsorption keine strukturellen Merkmale der geträgerten Vanadiumoxidstruktur. Im Gegensatz dazu zeigen Raman Spektren, die mit 256,7 nm Anregungswellenlänge aufgenommen wurden, strukturelle Informationen von reduzierten Vanadiumoxidspezies. Zusätzlich wurde der Katalysator unter propan- und wasserstoffreduzierenden Bedingungen in Abhängigkeit der Temperatur untersucht. Während Vanadyl (V=O), verbrückte V-O-V und Interphasenschwingungen (V-O-Si) bei hohen Temperaturen deutlich abnehmen, werden SiO-H Banden sichtbar. Die gesamten

Ergebnisse liefern einen direkten Nachweis für mögliche Reaktionspfade der oxidativen Dehydrierung von Propan, die bereits über die Dichtefunktionaltheorie abgefragt worden waren. Wasserstoffabstraktion von Propan findet daher über terminalen Sauerstoff (V=O) statt und führt zur Bildung eines Propyl-Radikals, welches anschließend an demselben oder an einem anderen Vanadium-Zentrum weiterreagiert. Unter der Annahme, dass molekularer Sauerstoff für eine schnelle Reoxidation sorgt, liegt während der Reaktion eine volloxidierte (geringreduzierte) Vanadiumoxidspezies vor, wie sie auch spektroskopisch beobachtet wurde. Um weitere mechanistische Einblicke in ODH-Reaktionen zu erhalten, dient der direkte Vergleich zur selektiven Oxidation mit Ethanol zu Acetaldehyd. Spektroskopisch gesehen zeigt der Katalysator eine signifkante Abhängigkeit zum eingesetzten Substrat. Ethanol chemisorbiert und bildet in der Folge eine Ethoxy-Spezies an Vanadium (V) aus, was zu einer Reduzierung der Vanadiumoxidspezies vor dem geschwindigkeitsbestimmenden Schritt, der C-H Aktivierung, zur Folge hat. Im Gegensatz dazu adsorbieren Propan Moleküle nur schwach, was die fehlende Beobachtung einer Bindung des Moleküls in den Raman-Spektren erklärt.

Im Gegensatz zu Sauerstoff führt der Einsatz von Kohlenstoffdioxid (CO_2) als Oxidationsmittel zu einer verbesserten Selektivität zu Propylen. Die erfolgreiche Aktivierung von CO_2 in dem ODH Zyklus wird durch den Nachweis von Kohlenstoffmonoxid im Gasauslass sichergestellt. UV-Vis- und 256,7 nm Raman-Spektren zeigen die Anwesenheit eines stark-reduzierten Vanadiumoxidkatalysators unter *operando* Bedingungen. Nach der Reaktion reoxidiert CO_2 reduzierte Vanadiumoxidspezies, die mittels UV Raman-Spektroskopie (256,7 und 385 nm) nachgewiesen werden können. Es wird angenommen, dass CO_2 für die Wiederherstellung des Vanadylsauerstoffes über V^{3+} verantwortlich ist. Isomerisierungsprozesse mit Wasserstoff an terminalem, verbrücktem und Interphasen-Sauerstoff laufen somit parallel ab. Die ODH-Reaktion mit CO_2 folgt einem V^{5+}/V^{3+} Redoxzyklus, während mit Sauerstoff auch ein V^{5+}/V^{4+} Redoxpaar möglich ist. Es werden verschiedene Faktoren identifiziert, die die Selektivtät beeinflussen, welche in Korrelation zum Reduktionsgrad stehen. Die Katalysatorreduktion führt zur Abnahme des Oligomerisierungsgrades und der Verfügbarkeit aktiver Sauerstoffspezies, wodurch die Totaloxidation von Propan effektiv unterdrückt wird.

Ceroxidgeträgerte Vanadiumoxidkatalysatoren zeigen bereits bei niedrigeren Temperaturen eine hohe katalytische Aktivität in der ODH von Propan. Dies ist auf eine aktive Trägerbeteiligung von Ceroxid (CeO_2) zurückzuführen. Die entwickelte Multiwellenlängen-Ramanstudie ermöglicht es erstmals, CeO_2 Bulk- und Oberflächenmoden sowie Vanadiumoxidschwingungen je nach anregender Wellenlänge selektiv zu verstärken. Die Erweiterung mit der FT-IR Gasphasenanalyse ermöglichte die Durchführung von *operando* Experimenten. Die aktive Trägerbeteiligung von CeO_2 wurde in der ODH von Ethanol untersucht, die als Modellreaktion dient. Die beobachtete Reduktion von CeO_2 deutet auf eine Stablisierung von Vanadium in seinem Oxidationszustand 5+ hin, was im Einklang mit theoretischen Berechnungen ist. Die signifikante Abnahme der Interphasenschwingung (V-O-Ce) ist ein direkter Hinweis auf den vorliegenden Synergieeffekt.

Abstract

The oxidative dehydrogenation (ODH) of propane is considered an attractive route for the production of propylene in order to meet its rising demand. Due to consecutive and parallel overoxidation reactions, low propylene yields were obtained so far. To this end, this work presents the development and application of various *operando* techniques with the purpose to elucidate the molecular structure-reactivity/selectivity relationship of supported vanadium oxide catalysts in ODH reactions.

A new *operando* gas chromatograph/Fourier-transform infrared (GC/FTIR) setup was installed, which was combined with multiwavelength Raman (256.7, 385, and 515 nm) spectroscopy. It is, to my knowledge, the first of its kind. In order to prevent a local hot spot and laser induced sample damage, the fluidised bed mode was implemented, resulting in a continuous mixing of the powdery sample during the measurements. This overcomes laser-induced effects, which have been a drawback in the past, especially at excitation wavelengths in the ultraviolet (UV). In the preliminary stage of the *operando* experiments, the commercial *in situ/operando* cells were evaluated. Especially the temperature gradient along the sample bed of the Raman cell was addressed. The nominal temperature is controlled by the output of an integrated thermocouple, which, however, is not in contact with the sample. In order to establish a correlation between the set temperature and the sample temperature, a direct measurement by means of a thermocouple was performed. A self-made attachment, which fixes the external thermocouple in the sample bed of the Raman cell, proves to be useful in order to study the temperature dependency in the closed cell under flowing gas and fluidised bed conditions. The setup was subsequently tested in propane ODH with a silica supported vanadium oxide catalyst.

The catalyst shows catalytic activity at temperatures >300°C, and the selectivity drops with increasing conversion. For the *operando* experiments, a reaction temperature of 502°C was chosen. The conversion and selectivity data obtained at this temperature is in agreement with literature values acquired in a conventional reactor under similar experimental conditions. This qualifies the setup in conjunction with the Raman cell and fluidised bed method for the *operando* approach (i.e., the simultaneous recording of spectroscopic information and activity data), and verifies the temperature correction to be valid.

The experimental approach includes the application of multiwavelength Raman, diffuse reflectance (DR) UV-vis and diffuse reflectance infrared Fourier transform (DRIFT) spectroscopy. As no major structural arrangements are observable upon switching from oxidative to reaction conditions, the first C-H activation is determined to be the rate-determining step. In the absence of oxygen, the catalyst is highly reduced, as determined via UV-vis spectroscopy. Raman spectra, excited at 515 nm, are highly affected by the high self absorption in the visible range, not containing any information on the structure of reduced vanadium oxide species. In contrast, 256.7 nm Raman spectra reveal spectral features related to reduced vanadium oxide species. In addition, the catalyst was examined in propane and hydrogen reducing environments in dependency on the temperature. Whereas vanadyl (V=O), bridging V-O-V, and interface V-O-Si vibrations significantly decrease at high temperatures, SiO-H bonds become visible. The overall results give direct evidence for possible reaction pathways of the oxidative dehydrogenation of propane, as previously examined by density functional theory (DFT). Hydrogen abstraction from propane by terminal oxygen (V=O) results in the formation of a propyl radical,

which subsequently reacts at the same or another vanadium oxide site. Under the assumption of fast reoxidation via molecular oxygen (O_2), a fully oxidated (low reduced) vanadium oxide species is present under reaction conditions, as spectroscopically observed. In order to gain further mechanistic insights into ODH reactions, the selective oxidation with ethanol (as a substrate) towards acetaldehyde serves for comparison. From a spectroscopic point of view, the catalyst shows a significant dependency on the substrate. Ethanol is chemisorbed forming ethoxy species attached to vanadium (V), resulting in reduced vanadium oxide species prior to the rate-determining step, the C-H activation. In contrast, propane is weakly adsorbed, which explains the apparent absence of the binding of the molecule in the Raman spectra.

The use of carbon dioxide (CO_2) as an oxidising agent instead of molecular oxygen shows an enhanced selectivity towards propylene. The successful activation of CO_2 in the ODH cycle is proven by the detection of carbon monoxide in the outlet gas stream. UV-vis and 256.7 nm Raman spectra reveal the presence of a highly reduced vanadium oxide catalyst under *operando* conditions. After the reaction, CO_2 reoxidises reduced vanadium oxide species, observable via UV Raman spectroscopy (256.7 and 385 nm). Under the assumption that CO_2 is able to recover the vanadyl oxygen over a V^{3+} species, isomerisation processes with hydrogen attached to terminal, bridging, and interface oxygen may occur in parallel. Hence, the ODH reaction with CO_2 follows a V^{5+}/V^{3+} redox cycle, whereas with O_2 a V^{5+}/V^{4+} redox couple is also possible. Several selectivity-determining factors are identified, which are related to the degree of reduction. Catalyst reduction results in a decrease of oligomerisation and a decline of available active oxygen species, which effectively suppresses overoxidation reactions.

Ceria supported vanadium oxide catalysts show high catalytic activity in propane ODH already at low temperatures, which is attributed to the active support participation of cerium oxide (CeO_2). The developed multiwavelength Raman study allows CeO_2 bulk, surface, and vanadium oxide related modes to be selectively enhanced, dependent on the excitation wavelength. The approach is extended with FTIR gas phase analysis to allow for *operando* experiments. The active support contribution of CeO_2 was studied by using ethanol ODH as a prototype reaction. The observed reduction of CeO_2 points to the stabilisation of vanadium in its +5 oxidation state, in agreement with theoretical predictions. The significant decrease of interface bonds (V-O-Ce) is a direct indicator for a synergetic effect.

Contents

1 Introduction

Climate change is considered to be the biggest challenge facing humankind in the 21st century. Since the late 1800s, the average annual temperature at the earth's surface has risen, revealing a close correlation with directly measured atmospheric carbon dioxide (CO_2) concentration.[1] The Intergovernmental Panel on Climate Change's (IPCC) Fifth Assessment Report concluded that human activities, such as the burning of fossil fuels, are the main cause. In 2018, the IPCC reported on the rise of 1.5°C rise above pre-industrial levels and the impacts, emphasising that limiting global warming would require "rapid, far-reaching and unprecedented changes in all aspects of society".[2] The Paris Agreement in 2015 brought all nations together to undertake ambitious efforts to fight a common cause. It was determined that all Parties would contribute nationally and report regularly upon their respective greenhouse gas (GHG) emission.[3]

The chemical sector is one of the biggest industries in the world and by far the largest industrial consumer of energy. In 2012, its total worldwide energy consumption was estimated to be roughly 10%, which corresponds to 30% of the total industrial energy demand worldwide.[4] 7% of global GHG emissions were attributed to the chemical sector, which requires the development and implementation of energy-efficient processes. Catalysis may play a key role in this transformation as it is projected to save 1 gigatonne of carbon dioxide equivalent (CO_2-eq) per year by 2050.[5] So far, already around 90% of chemical production processes apply catalysts. However, a full understanding of catalytic processes, in particular for several "dream reactions", is still lacking.[6, 7]

As a result of an increasing global population combined with rising living standards, especially in developing/emerging countries like China, India and Southeast Asia, the demand for olefins, primarily for ethene and propene, is growing.[8, 9] Olefins are considered to be key components of the chemical industry. Propylene, for example, is the raw material of the plastic polypropylene, which is used in a wide variety of applications.[10] At the present time, main processes for olefin production are steam cracking, fluid-catalytic-cracking (FCC) and catalytic dehydrogenation. It is predicted that the supply from refinery FCC and steam-crackers will not cover future demand. Nowadays, dehydrogenation is an economically attractive technology to fill the gap.[9] The oxidative dehydrogenation (ODH), with its advantage to run exothermic, is an energy-saving alternative to these technologies. However, the industrial implementation of propane ODH has not yet succeeded due to low propene yields.[10, 11] Undesirable consecutive and parallel combustion reactions are attributed to the low propylene selectivities.

Vanadium oxide-based catalysts are used in a wide variety of technical processes [12–16] and represent the most studied catalytic material for the ODH of propane [10, 11]. During the reaction the catalyst is present in a solid state while the reactants and products are in a gaseous phase, which is referred to as heterogeneous catalysis. Besides bulk catalysts, supported vanadium oxide catalysts are widely employed. Thereby, the vanadium oxide phase is deposited on a high surface area oxide support like, e.g., SiO_2, Al_2O_3, TiO_2, and CeO_2.[17] According to the literature, various factors (e.g. synthesis procedure, loading and support) influence propylene productivity.[10] Structure-activity relationships, kinetic studies and theoretical calculations are reported in order to obtain insights into the overall reaction mechanism. The common vision involves a rational catalyst design. For that, a full understanding of the underlying reaction mechanism is still pending.[10]

In recent years, the potential of carbon capture and utilisation (CCU) is evaluated in the context of providing technological solutions to the problems of greenhouse-gas emissions and the increasing energy demand.[18–20] In particular, the use of carbon dioxide (CO_2) as a carbon source is considered. For ODH reactions, CO_2 has received significant attention as a mild oxidant. High olefin selectivities are obtained due to the inhibition of deep oxidation processes.[21–24] The use of CO_2 is attractive due to its abundant availability and low cost, but suffers from the limitation of its inertness.[21, 23–25] This research should contribute to the mechanistic understanding of supported vanadium oxide catalysts in ODH reactions. The dependency of the support and the oxidising agent is studied. For this reason, an *operando* approach was chosen. The combination of the spectroscopic characterisation of a catalytic material during the reaction with the simultaneous measurement of its activity is known as *operando* methodology [26–29]. In recent years, it has demonstrated its high potential for the understanding of catalytic processes.

In this work, *operando* Raman, UV-vis, and DRIFT spectroscopy was applied in order to study the dynamics of dispersed vanadium oxide structures in the ODH of propane and ethanol. The latter serves as a prototype reaction as it is characterised by a very high selectivity for the target product acetaldehyde at low temperatures (<200°C). Similarly to Waleska et al. [30], the resonance Raman effect is exploited in a targeted manner via a multiwavelength Raman approach.

The support dependency is studied using SBA-15 and CeO_2 as supports. SBA-15 (Santa Barbara Amorphous-15) is a mesopourous silica sieve with uniform hexagonal pores and narrow pore size distribution. Its special characteristic is its high internal surface area of typically 400-900 m^2/g with framework walls of about 3.1 to 6.4 nm, ensuring high hydrothermal and mechanical stability.[31] In comparison, ceria is known for its capability to store/release oxygen [32]. It has been proposed that CeO_2 actively participates in the reaction.[33] Additionally, two different oxidising agents, O_2 and CO_2, are used in order to address selectivity-determining aspects, as previously reported for O_2 and N_2O [34]. The role of CO_2 in ODH reactions is a subject of current discussion.

The thesis is divided into eight chapters. After giving an overview (chapter 1), the reader is introduced to the theory of Raman and resonance Raman effects in chapter 2 due to its particular relevance to this work. The experimental details in chapter 3 include the synthesis of the catalysts, the specifications of the characterisation equipment, and the experimental procedures. As the installation of the so-called *operando* Raman GC/FTIR setup was a significant part of this work, its details are described in a separate chapter (chapter 4). The abbreviations GC and FTIR refer to gas chromatography and Fourier-transform infrared spectroscopy, respectively. They enable the continuous measurement of activity and selectivity of the catalyst during the spectroscopic observation. The setup allows the performance of propane and ethanol ODH reactions with O_2 and/or CO_2 as an oxidant. Moreover, the design of commercial *in situ* cells is analysed in the context of the temperature profile in the catalyst bed. Chapter 5 presents the *operando* results of a silica supported vanadium oxide catalyst for the ODH with propane. Complementary experiments were conducted enabling a subsequent mechanistic discussion. This is followed by the results obtained for the ODH with CO_2 (chapter 6). In order to study active oxygen species, a pretreatment procedure [35] was implemented before starting the reaction. Ceria supported vanadium oxide was studied in the ODH with propane in comparison to blank ceria (chapter 7). In order to verify the active support participation, ethanol ODH was used as a test reaction. *Operando* spectra were obtained by developing a multiwavelength

Raman approach allowing the detection of cerium oxide and vanadium oxide-related features. Finally, a conclusion and outlook is given in chapter 8.

1.1 The oxidative dehydrogenation of alkanes and alcohols over vanadium oxide catalysts

The general reaction network of ODH reactions (figure 1.1) proceeds via a parallel-consecutive scheme. The direct combustion of propane and the consecutive overoxidation of propene are responsible for the low propene selectivity.

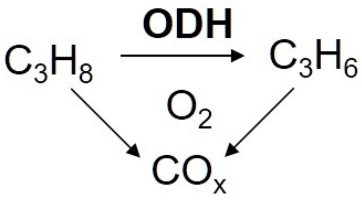

Figure 1.1: Reaction network of propane ODH

As direct combustion may play a minor role, the stoichiometric equations are described as follows.[36]

$$C_3H_8 + 0.5\ O_2 \rightarrow C_3H_6 + H_2O \tag{1.1}$$

$$C_3H_6 + 3.5\ O_2 \rightarrow 2\ CO + CO_2 + H_2O \tag{1.2}$$

For a kinetic description, mostly the Mars–van Krevelen mechanism is found to describe that some products of the reaction leave the solid catalyst's surface while taking one oxygen atom. Subsequently, the catalyst is reoxidised by molecular oxygen in a second step.[37] Recently, Carrero et al. [10] provided a review on the current state of research for the use of supported vanadium oxide catalysts in propane ODH. Special attention was given to aspects like catalyst synthesis, loading effects, structure-activity relationship, and support effects, emphasizing the demand for corresponding *in situ/operando* studies. The amount of referenced publications referring to a silica supported vanadium oxide catalyst clearly demonstrates that it has been the most studied catalytic material. In comparison to other supports, VO_x/SiO_2 shows higher activation energies. Significant support effects can be neglected, which in turn facilitates analysis and interpretation. Relatively constant TOF values for propane consumption as a function of surface vanadium oxide coverage indicate that the ratio of surface VO_4 oligomers/monomers does not affect the propane kinetics. It has been proposed that only one surface VO_4 site is involved in the rate-determining step of propane activation.

For a better understanding of alkane activation, the oxidative dehydrogenation of alcohols has been serving as a model reaction due to its high selectivity towards the desired product at temperatures below 200°C. Beck et al. [38] proposed similar reaction mechanisms for the ODH of ethanol and propane, based on a dimeric vanadium oxide structure.

The vanadium oxide catalysts showed the same reactivity across different supports for both reactions. Impedance spectroscopy provided a direct correlation of defect formation enthalpy with activation energy of propane and ethanol oxidation. By means of density functional theory (DFT) calculations, it is widely suggested that ethanol adsorbs dissociatively by breaking a V-O-S (S=support) or V-O-V bond, which consequently leads to ethoxy formation. The hydrogen atom is transferred to the V=O moiety and a $C_2H_5O^*$ radical is created resulting in the reduction of the V-site from +5 to +4. Subsequently, the rate-determining C-H activation proceeds at the same or at a neighbouring V-site, and acetaldehyde is desorbed. As a result, water is formed either after recombination of two V(IV)-OH groups or directly from the V(III) site. Molecular oxygen reoxidises the reduced catalyst, which closes the catalytic cycle. As illustrated in figure 1.2, a comparable mechanistic model has been proposed for the ODH of propane, which runs at higher temperatures. The first C-H activation leads to the formation of a propyl radical followed by the second H-abstraction and the desorption of a propene molecule. After the formation of water, the catalyst is reoxidised with gas phase oxygen. C-H activation is expected to constitute the rate-determining step.

Several theoretical calculations applying DFT calculations and microkinetic simulations have been executed to elucidate elementary reaction steps. Rozanska et al. [39] investigated possible reaction mechanisms over a monomeric vanadium oxide species supported on silica. As the first step, the physisorption of the propane molecule onto the surface site via van der Waals forces is considered, which explains the apparent absence of the binding of the propane molecule. Subsequently, the initial C-H activation step proves to be the rate-determining step. The vanadyl V=O is determined to be the active site yielding in a propyl radical and a HO-V^{IV} site. The radical rebounds as alkoxide or alcohol attached to a $V^{III}(OSi)_3$ surface site, and propene desorbes. However, C_3H_6 may also be directly formed from the diradical intermediate. Due to the reduction of the catalyst, HO-V^{IV} sites are left on the surface. The subsequent publication by Rozanska et al. [40] included dimeric and polymeric vanadium oxide species into possible reaction mechanisms as they theoretically determined that a mixture of monomeric, dimeric, and oligomeric species is likely to exist at submonolayer coverage. Therefore, the second hydrogen abstraction may either be abstracted at the same vanadia site or at a different one. The V(V)/V(IV) redox cycle, yielding two HO-V^{IV} species, is preferred over the V(V)/V(III) cycle, yielding one $H_2O \cdot V^{III}$ species. Furthermore, mikrokinetic simulations revealed lower Arrhenius activation barriers for a dimeric site than for a monomeric one. Direct calculations of the reaction energy in dependency with the vanadium oxide cluster size point to an increase of reactivity with increasing oligomeric size.

Selectivity and its relation to the active oxygen site has been addressed in the literature. Dinse et al. [36] pointed out that the activation energy of the oxidative dehydrogenation is higher than that of the total oxidation of propene. Therefore, it is recommended to perform the ODH of propane at a temperature as high as possible. Unselective gas phase reactions are expected at temperatures above 550°C. A further theoretical study of the deep oxidation reactions over the $V_2O_5(001)$ surface has revealed that, as the vanadyl oxygen is the most active species for any kind of oxidation reaction, the bridging V-O-V is the most selective one.[41] Isopropoxide formation is responsible for deep oxidation byproducts. Furthermore, Rozanska et al. [42] studied the reoxidation of vanadyl oxygen species by O_2 in comparison to N_2O. Due to the fact that molecular oxygen consists of two oxygen atoms, peroxovanadate species may be formed. They concluded that peroxovanadates are highly reactive for consecutive propene oxidation. Ovsitser et al. [43] related the improved C_3H_6

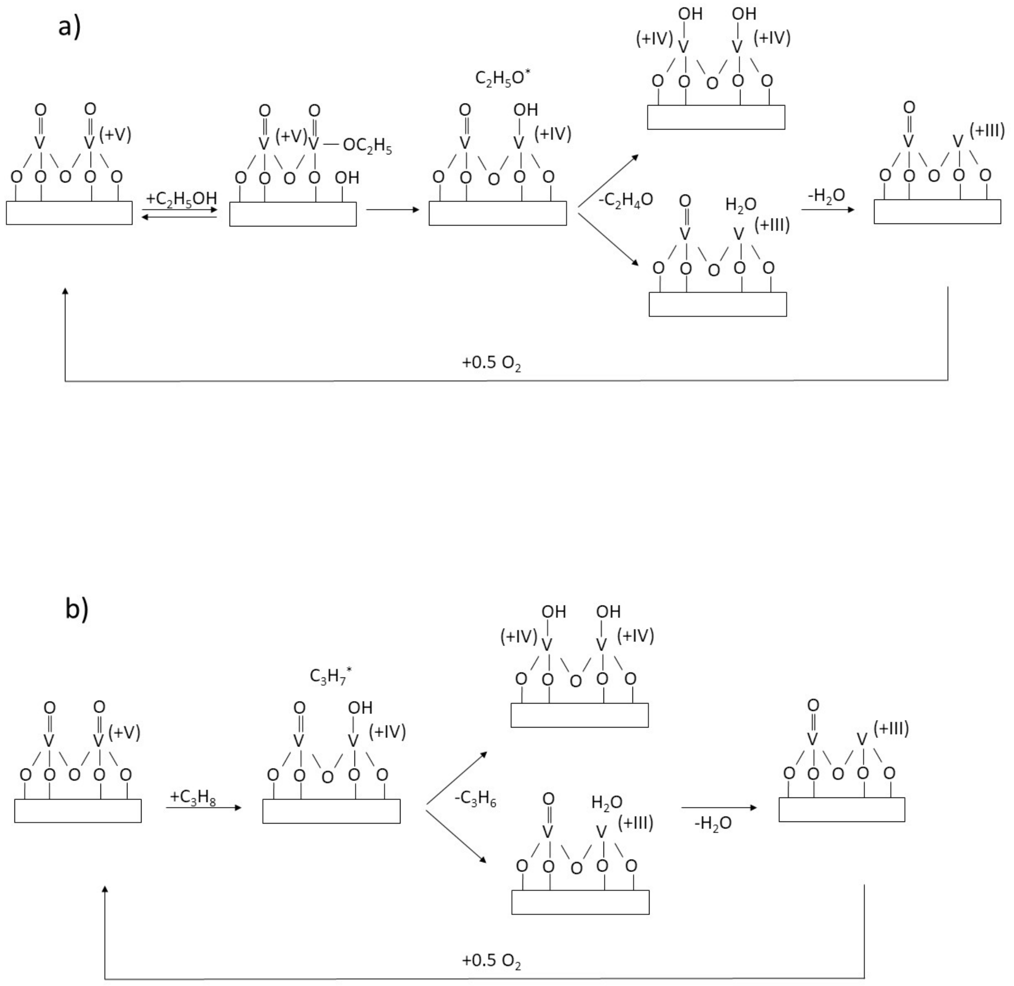

Figure 1.2: Proposed mechanistic model of the ODH of a) ethanol and b) propane by Beck et al. [38]

selectivity with N_2O to the increased degree of catalyst reduction in accordance with their *in situ* UV-vis experiments. As N_2O reoxidises reduced VO_x species slower than O_2, the surface density of active oxygen species is reduced. They concluded that these are spatially separated in the presence of N_2O.

1.2 The support effect

A strong impact of the support material has been reported for the ODH of alcohols and alkanes affecting selectivity, activation energies, and turn over frequencies inter alia.[44] It has been correlated to Sanderson electronegativity [45], the reducibility [44] and the oxygen defect formation energy [38]. The support behaves as a ligand and thus affects characteristics of the surface VO_4 sites via the bridging V-O-S bond. Various investigations allow the ranking of the catalytic activity of supported vanadium oxide species with the support material as follows [44, 46, 47].

$$TiO_2 > ZrO_2 > CeO_2 > Al_2O_3 > SiO_2$$

In comparison to other supports, ceria itself shows catalytic activity in oxidation reactions. Dinse et al. [44] reported even lower conversion values on V-CeO_2 than on the bare support. The catalytic material is known for its high oxygen mobility, and its performance is attributed to the ability in stabilising reduced states by accommodating electrons in localised f-states. For ODH reactions it has been assumed that ceria directly participates in the redox process as it stabilises vanadium in its oxidation state +V, whereas ceria becomes reduced.[32, 48, 49]

1.3 The use of carbon dioxide as a soft oxidant

Carbon dioxide has gained considerable interest regarding its utilisation as an oxidant in recent years, including the dehydrogenation of alkanes to olefins, the dehydrogenation of ethylbenzene to styrene, and CO_2 reforming, to mention a few.[23] At present, only a few processes have been technically implemented based on CO_2 as a soft oxidant. In 2012, Park et al. [21] summarised current results on the utilisation of CO_2 as a soft oxidant and promoter. For ODH reactions, different oxidising agents like N_2O, SO_2, and CO_2 have already been tested. In comparison to oxygen, selectivity towards the desired product is significantly improved using milder oxidants. CO_2 is currently considered for ethane, propane, n-butane, and ethylbenzene ODH.[23] One of the major concerns is the activation of CO_2. The bending of the linear molecule with two equivalent C=O bonds is considered as an essential step. It requires catalytically active sites involving the electron donation from the catalyst surface to the antibonding orbital of CO_2 (acid sites).[50–52] Different coordination types are theoretically identified on metal and metal oxide surfaces.[51, 53] In contrast, ODH reactions require the H-abstraction from the substrate, which is facilitated by basic sites.[25] Hence, the correct balance of surface acidity/basicity is an important factor of catalyst design.

Different metal oxides like Cr [54–56], Ga [57], and V [58–60] supported on inorganic oxides (SiO_2, Al_2O_3, TiO_2), mesoporous sieves, and carbonaceous materials have been tested. For the ODH of propane, only few studies have been published, mainly applying chromium based catalysts [61–64].
The reaction can be described as follows.

$$C_3H_8 + CO_2 \rightarrow C_3H_6 + CO + H_2O \tag{1.3}$$

Besides, a two-step pathway is also considered, which includes the dehydrogenation of propane followed by the reverse water gas shift reaction.

$$C_3H_8 \rightarrow C_3H_6 + H_2 \tag{1.4}$$

$$CO_2 + H_2 \rightarrow CO + H_2O \tag{1.5}$$

The overall reaction network is schematically illustrated in figure 1.3.

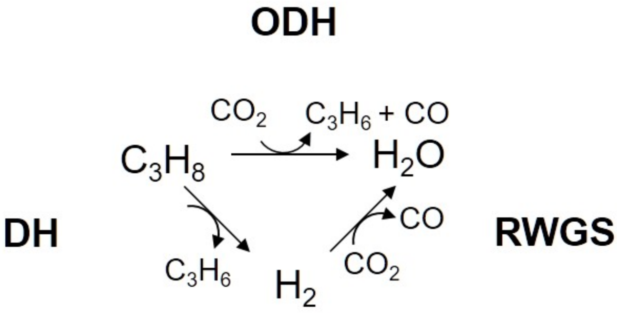

Figure 1.3: Reaction network of ODH using CO_2 as an oxidising agent according to Ascoop et al. [35]

Carbon dioxide is also considered to participate in the decoking process via the Boudouard reaction (see equation 1.7).

$$C_3H_8 \rightarrow 3\ C + 4\ H_2 \tag{1.6}$$

$$C + CO_2 \rightarrow 2\ CO \tag{1.7}$$

So far, the role of CO_2 in the oxidative dehydrogenation of propane is still under discussion.

Takahara et al. [65] studied the dehydrogenation of propane over a silica supported vanadium oxide in the presence and absence of CO_2. The catalytic activity was enhanced using CO_2 as a soft oxidant. It has been suggested that in the presence of CO_2 vanadium is in its oxidation state +5. Ascoop et al. [35] explicitly explored the role of CO_2 experimentally and theoretically over a WO_x–VO_x/SiO_2 catalyst. Isothermal reduction profiles provided the conclusion that CO_2 is not able to completely reoxidise the catalyst. By co-feeding D_2 into the gas mixture of C_3H_8 and CO_2, only 45% of the resulting water contained D_2O. They suggested that propane dehydrogenation in the presence of CO_2 proceeds simultaneously via direct oxidative dehydrogenation and non-oxidative dehydrogenation followed by the reverse water gas shift reaction. Moreover, C-H activation was determined to be the rate-determining step while reoxidation of the catalyst with CO_2 is probably occurring faster. These results are based on the DFT-calculated Gibbs free energy profile at 600°C using a cubic silsesquioxane cluster with an isolated V^{5+}–O–V^{3+} unit as a model for the active site.[39]

The literature shows that the nature of the support also plays a role for propane ODH with CO_2. The effect of acid-base properties and the ease of oxygen-transfer are specifically mentioned.[21, 24, 25] In some cases, the support itself is also working as a catalyst. Surface/lattice oxygen participates in the abstraction of H_2 by the formation of water. CO_2 in turn serves as a supply for the reoxidation of surface/lattice oxygen.[25] Wang et al. [66] studied the ethane ODH with CO_2 over various supports including silica, alumina, zirconia, and titania. Whereas silica supported chromium oxide shows the highest catalytic activity, a low performance was obtained with titania. It was suggested that TiO_2 affects the redox cycle of Cr^{6+}/Cr^{3+} due to an electronic exchange between distant Cr^{3+} ions. Due to the potential to activate carbon dioxide [67] ceria is considered a promising candidate for several chemical routes [68]. It has already been tested in the ODH of ethane [69], propane [70, 71], butane [72, 73], and ethylbenzene [74–76]. Liu et al. [77] demonstrated that ceria has a promoting effect on vanadium, suggesting that the ODH of ethylbenzene occurs via a redox cycle of vanadium from +5 to +4. CeO_2 stabilises vanadium to +5, which is accompanied by the reduction from Ce^{4+} to Ce^{3+}. CO_2 is responsible for its subsequent reoxidation from +3 to +4, completing the full cycle. The mechanism of propane ODH utilising CO_2 as a soft oxidant was studied on a Pd/$CeZrAlO_x$ catalyst by Nowicka et al. [70]. Temperature-programmed desorption of NH_3 and CO_2 has revealed that the catalyst contained acidic and basic sites. DRIFT spectra showed that CO_2 is able to dissociate over the reduced catalyst surface, suggesting however that the presence of a noble metal plays a crucial role. The experimental results indicated that the reaction over the ceria-based catalyst occurs via a Mars-van Krevelen mechanism and a non-oxidative dehydrogenation route, followed by a hydrogen consumption step via the reverse water gas shift reaction.

1.4 The *operando* and multiwavelength approach

Determining the active site in a catalyst material is a big challenge, which would allow for the rational design of catalysts. In particular the field of "*operando* spectroscopy" is gaining more attention for this purpose.[26] This term refers to a methodology that combines spectroscopic characterisation with a simultaneous measurement of catalytic activity/selectivity. It has been introduced into the catalysis literature in 2002. *Operando* (Latin for working) differ from *in situ* techniques which are "on site" characterisations under a certain environment, even under reaction conditions relevant to catalytic operation.[27] The ability of a simultaneous catalytic measurement demands an appropriate reaction cell and acquisition device for the catalytic data. *Operando* approaches may include, e.g., sample characterisation via infrared (IR), Raman, UV-vis, electron paramagnetic resonance (EPR), and X-ray diffraction (XRD) combined with activity measurements via FTIR, GC or MS (mass spectrometry) gas phase analysis.[29] Each of these techniques is facing certain limitations. Hess [78] emphasised the potential of Raman spectra providing detailed structural information of a catalytic material. In comparison to IR, gas phase contributions are negligible due to the weak light scattering from the low density of molecules in the gas phase.

A reactor for fundamental *operando* spectroscopy studies should at best fulfil several requirements: low dead volume, flexible space velocity to vary conversion, and a uniform temperature profile allowing isothermal measurements.[27] In particular, the latter is discussed for commercial reactor cells and self-designed cells. Meunier [79] emphasised exemplarily in the case of DRIFT studies that the temperature of the very surface of the sample bed may differ significantly from the corresponding temperature in the depth of the sample holder. The temperature variation was determined to 100°C at a set temperature of 460°C.[80] Chua and Stair designed a Raman cell resembling a fluidised bed reactor. It avoids potential sample damage by UV photons during UV Raman spectroscopy.[81] Beato et al. [82] recently reported a more compact version whereby particles are kept in a fluidised mode by the back pulse of a membrane pump. The development is also considered to be relevant for highly exothermic reactions or catalysts that rapidly deactivate due to carbon deposition or coking.

Several *operando* studies have been reported on the ODH of propane including *operando* EPR/UV-vis/MS, *operando* EPR/Raman/UV–vis/MS, *operando* GC-Raman, and *operando* UV-vis/Raman/X-ray absorption fine structure (XAFS)/MS.[29] Recently, Waleska et al. [30] reported the first *operando* multiwavelength and time-resolved Raman spectroscopy approach for the ODH of ethanol. Three different excitation wavelengths in the visible and UV were applied, and the resonance Raman effect was exploited in a targeted manner. The spectroscopic results allowed the understanding of the reaction mechanism of the ODH with ethanol for a silica supported vanadium oxide catalyst. The mechanisms proposed by Kilos et al. [83], Beck et al. [38], and Nair et al.[84] could be confirmed demonstrating the great potential of *operando* spectroscopic techniques. Generally, a multiwavelength approach has been tested for several heterogeneous catalysts.[85–87] By the selective enhancement of Raman peaks, specific catalytic sites can be studied as previously reported for silica and ceria supported vanadium oxide catalysts.[86]

2 Theoretical

Operando and *in situ* techniques have gained importance for the characterisation of heterogeneous catalysts like e.g. vanadium oxide catalysts. Raman, IR, and UV-vis spectroscopic methods among others have been used in order to obtain an understanding of molecular and electronic properties of the respective catalyst.[17] In recent years, the application of Raman spectroscopy and especially resonance Raman spectroscopy has attracted interest in this research field.[85] As these spectroscopic methods are a fundamental part of this research work, an introduction into the underlying theory will be given here.

First, the phenomenon of Raman scattering will be described in terms of classical and quantum theory, followed by an introduction to resonance Raman effects.

2.1 Raman effect

2.1.1 Classical treatment of Raman scattering

There are various processes of the interaction between light and matter. Incident photons may either be absorbed or scattered, or may not interact with the material and pass through it.[88, 89] When scattering occurs, the oscillating electromagnetic field disturbs the electronic charge distribution in the molecule inducing a dipole moment even in the case of an unpolar molecule. The following mathematical description follows the derivation outlined by Dieing et al.[89]. The induced dipole moment μ can be expressed by the external electric field $\vec{E}$ and a proportionality factor, the molecular polarisability α, as follows:

$$\vec{\mu} = \alpha \cdot \vec{E} \tag{2.1}$$

The polarisability has tensor properties and specifies to which extent the electrons in the molecule can be displaced relative to the nuclei. The external field of the incident monochromatic radiation of frequency ω_0 can be written as

$$\vec{E} = \vec{E}_0 \cos\left(\omega_0 \cdot t\right) \tag{2.2}$$

When the molecule vibrates about its equilibrium position, the polarisability changes periodically and can be expressed in a Taylor series with the summation over all normal coordinates q of vibration.

$$\alpha = \alpha_0 + \sum_{q=1}^{N} \left[\left(\frac{\partial \alpha}{\partial q} \right)_{q_0} \cdot q + \frac{1}{2} \left(\frac{\partial^2 \alpha}{\partial q \partial q'} \right)_{q_0 q_0'} \cdot q \cdot q' + \ldots \right] \tag{2.3}$$

Oscillations with a characteristic frequency ω_q along each normal coordinate q are given by

$$q = q_0 \cdot \cos(\omega_q t) \tag{2.4}$$

The final expression of the induced dipole moment can be obtained via the electronic harmonic approximation, which neglects terms of higher order in the Taylor expansion. Moreover, the sum over all normal modes can be reduced to the representative mode q and the trigonometric formula for the product of two cosine functions may be applied.

$$\mu(t) = \alpha_0 \cdot E_0 \cos(\omega_0 t) + \frac{1}{2}\left(\frac{\partial \alpha}{\partial q}\right)_{q_0} \cdot q_0 \cdot E_0 \cdot \cos\left[\left(\omega_0 - \omega_q\right) t\right] + \frac{1}{2}\left(\frac{\partial \alpha}{\partial q}\right)_{q_0} \cdot q_0 \cdot E_0 \cdot \cos\left[\left(\omega_0 + \omega_q\right) t\right] \tag{2.5}$$

The formula reveals the fundamental principles of Raman scattering. The first term represents the elastic Rayleigh scattering where the scattered light has the same frequency as the incident radiation. Therefore it does not contain any information about the molecule. The oscillation frequencies in the second and third term vary from the laser radiation by the molecular normal mode frequency. The change in polarisability $\left(\frac{\partial \alpha}{\partial q}\right)_{q_0}$ is a fundamental requirement for the Raman effect to occur. The red shifted radiation is called Stokes scattering and is usually delineated in Raman spectra. Anti-Stokes scattering is characterised by the sum $\omega_0 + \omega_q$ and represents a source for radiation, which is blue shifted with respect to the laser frequency. Its intensity is strongly reduced due to the Boltzmann population of thermally excited vibrational states.

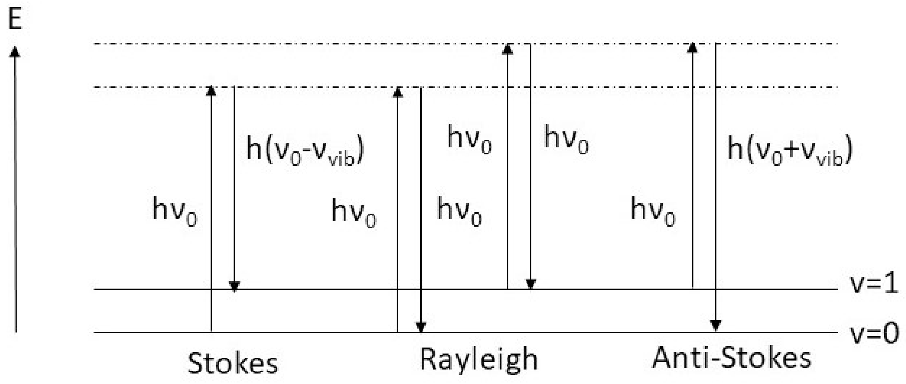

Figure 2.1: Raman scattering processes for two vibrational states v=0 and v=1. The upper lines represent virtual energy states. The incident light is described as $h\nu_0$; Stokes scattering is characterised by $h(\nu_0 - \nu_{vib})$ and Anti-Stokes by $h(\nu_0 + \nu_{vib})$, respectively.

2.1.2 Quantum-mechanical treatment of Raman scattering

The classical theory explains the existence of the Raman effect and the frequency of Raman lines. However, the polarisability does not include the dependency on characteristic electronic transition frequencies within the scattering molecule. Moreover, no description of molecular rotation is provided, and the vibrational Raman scattering tensor is only partly correct. In principal, the approach of the quantum mechanical treatment[89–91] is similar to the classic one. The transition electric dipole replaces an oscillating electric dipole and the polarisability is defined in terms of the wave function and energy levels of the system.[90] Hence, the description of α is based on quantum mechanics and in particular perturbation theory. For both treatments, the electric field has the same form.

The induced transition electric dipole moment $(\mu^{(1)})_{fi}$ is given as

$$(\mu^{(1)})_{fi} = \left\langle \Psi_f^{(1)} | \hat{\mu} | \Psi_i^{(0)} \right\rangle + \left\langle \Psi_f^{(0)} | \hat{\mu} | \Psi_i^{(1)} \right\rangle \tag{2.6}$$

$\Psi_i^{(0)}$ and $\Psi_f^{(0)}$ are the unperturbed time-dependent wave functions of the initial state i and the final state f, whereas $\Psi_i^{(1)}$ and $\Psi_f^{(1)}$ are the corresponding first-order perturbed time-dependent wave functions. $\hat{\mu}$ corresponds to the electric dipole moment operator. The perturbed time-dependent and unperturbed time-dependent wave functions are related to each other and can be substituted for $\Psi_i^{(1)}$ and $\Psi_f^{(1)}$, respectively. Afterwards, the final equation is rearranged according to their frequency dependency. The real induced transition electric dipole, which includes the Stokes and Anti-Stokes parts, may be written after several assumptions as follows (see eq. 2.7). $|\Psi_i\rangle$ has been simplified to $|i\rangle$ and so on.

$$(\mu_\rho^{(1)}) = \frac{1}{2\hbar} \sum_{r \neq i,f} \left\{ \frac{\langle f|\widehat{\mu_\rho}|r\rangle \langle r|\widehat{\mu_\sigma}|i\rangle}{\omega_{ri} - \omega_0 - i\Gamma_r} + \frac{\langle f|\widehat{\mu_\sigma}|r\rangle \langle r|\widehat{\mu_\rho}|i\rangle}{\omega_{rf} + \omega_0 + i\Gamma_r} \right\} \widetilde{E}_{\sigma_0} \exp(-i\omega_s t) + \text{complex conjugate} \tag{2.7}$$

$\widehat{\mu_\rho}$ and $\widehat{\mu_\sigma}$ are the ρ and σ components of the electric dipole moment operator in the cartesian basis. $|r\rangle$ refers to the intermediate state of Raman scattering. The laser frequency is given as ω_0, while ω_{ri} and ω_{rf} quantify the energetic differences between the respective states. Γ_r is a damping constant, and ω_s represents the absolute frequency of the scattered radiation ($\omega_s = \omega_0 - \omega_{fi}$). $\widetilde{E}_{\sigma_0}$ is the σ component of the complex amplitude of the plane harmonic electromagnetic wave. The general transition polarisability $(\alpha_{\rho\sigma})_{fi}$ is subsequently described as follows:

$$(\alpha_{\rho\sigma})_{fi} = \frac{1}{\hbar} \sum_r \left\{ \frac{\langle f|\widehat{\mu_\rho}|r\rangle \langle r|\widehat{\mu_\sigma}|i\rangle}{\omega_{ri} - \omega_0 - i\Gamma_r} + \frac{\langle f|\widehat{\mu_\sigma}|r\rangle \langle r|\widehat{\mu_\rho}|i\rangle}{\omega_{rf} + \omega_0 + i\Gamma_r} \right\} \tag{2.8}$$

2.2 Resonance Raman effect

Equation 2.8 describes the interaction of a phonon of frequency ω_0 with a molecule, which is in the initial stationary state $|i\rangle$. Several cases can be considered for ω_0 and ω_{ri}. Normal scattering occurs when $\omega_0 << \omega_{ri}$. The molecule is excited to a virtual state, from which it subsequently makes a transition to a final state $|f\rangle$. The state is called virtual as it is not a solution of the time-independent Schrödinger equation. Hence, it does not correspond to any well-defined value of the energy. The second case considers $\omega_0 \rightarrow \omega_{ri}$, which is pre-resonance Raman scattering. When $\omega_0 \approx \omega_{ri}$, the incident excitation wavelength is resonant with a molecular electronic transition. Hence, the first term dominantly contributes to the molecular polarisability. The mathematical expression is described as follows:

$$(\alpha_{\rho\sigma})_{fi} = \frac{1}{\hbar}\sum_{r}\left\{\frac{\langle f|\widehat{\mu_\rho}|r\rangle\langle r|\widehat{\mu_\sigma}|i\rangle}{\omega_{ri}-\omega_0-i\Gamma_r}\right\} \tag{2.9}$$

As a consequence, a significant increase in intensity is observed, which can be orders of magnitude. However, the intensity of the Raman scattered light can be strongly affected when self-absorption occurs.[92–94] The respective position of the excitation wavelength and the emitted wavelength in the absorption regime are crucial.[94] These effects need to be considered to explain the Raman spectra obtained within the multiwavelength approach in this work.

3 Experimental

This chapter contains the experimental details of this work. First, the preparation of the silica and ceria supported vanadium oxide catalysts is outlined followed by the description of the characterisation equipments. Finally, the procedure of the catalytic measurements and *operando* experiments for propane and ethanol ODH reactions is introduced. Details on the complete experimental setup can be found in the following chapter as the development and installation was a significant part of this research work.

3.1 Catalyst preparation

The synthesis procedure of SBA-15 was performed as described previously [31, 95]. 4.0 g of Pluronic P123 ($EO_{20}PO_{70}EO_{20}$, BASF) were mixed with 120 ml of 2 M HCl and 30 ml deionized water in a polypropylene bottle and stirred at 35°C in an oil bath until they were completely dissolved. Subsequently, 8.5 g of tetraethyl orthosilicate (TEOS, Sigma-Aldrich, $\leq$ 99%), which serves as the precursor for silica oxide, was added under stirring, which was maintained for further 20 h at 35°C. The bottle was placed in an oven at 85°C for 24 h. Afterwards, the suspension was filtered by a glass frit and the ground powder was calcined at 550°C for 12 h in ambient air by applying a heating ramp of 1.5°C/min. A further synthesis of SBA-15 was performed with a higher batch size.

CeO_2(111) particles were synthesised according to the procedure previously reported by Filtschew et al. [96]. Cerium(III) nitrate hexahydrate (99.5 % Sigma Aldrich) was calcined two times at 600°C for 12 h applying a heating rate of 6°C/min. After each calcination step the white powder was sieved with a mesh size of 200 μm.

Incipient wetness impregnation [97] was executed to load the respective supports. Vanadium(V) oxytriisopropoxide ($\geq$97%, Sigma Aldrich) was mixed with anhydrous 2-propanol (99.5%) in a glove box and added drop by drop to the samples while pulverising in an agate mortar. Subsequently, the yellow powders were calcined in an oven at 550°C for 12 h with a heating rate of 1.5°C/min.

An overview of the samples is presented in table 3.1. Each support was synthesised twice and their respective surface area was determined by the Brunauer-Emmet-Teller method (BET). The description of the BET-method can be find in the following section. As impregnation was performed various times, its effect on the final surface area was exemplarily quantified for two loaded SBA-15 samples marked with a number. The two results indicate that loaded SBA-15 samples, used in this work, contained a surface density of around 0.6 V/nm^2. For comparison, CeO_2 samples were impregnated with a surface density of 0.6, 1.2 and 2.3 V/nm^2 allowing the study of loading dependencies.

For the operation in fluidised bed mode [98], particle sizes between 200 and 300 μm were obtained by pressing 100 mg of SBA-15 at 75 MPa for 3s. Subsequently, the pellet was finely crushed in order to sieve with mesh sizes of 200 and 300 μm. The final samples were stored in an oven at 85°C. Herbert et al. [99] reported the mechanical stability of loaded VO_x/SBA-15 samples under these pressing conditions. Hence, it is assumed that the samples were not affected. Respective ceria charges were obtained in a similar manner.

Table 3.1: Overview of synthesised SBA-15 and CeO_2 samples

Sample	Surface Area (m^2/g)	Density (V/nm^2)	Loading (wt%)	Concentration (mol/l)
SBA-15 (#1)	730.7			
SBA-15 (#2)	697.5			
VO_x/SBA-15 (#1)	603.9	0.66	3.38	0.374
VO_x/SBA-15 (#2)	617.3	0.61	3.20	0.357
CeO_2 (#1)	62.3			
CeO_2 (#2)	56.3			
0.6 VO_x/CeO_2 (#1)		0.56	0.30	0.231
1.2 VO_x/CeO_2 (#1)		1.24	0.66	0.514
2.3 VO_x/CeO_2 (#1)		2.28	1.20	0.943

3.2 Physico-chemical characterisation

3.2.1 Nitrogen physisorption

Specific surface areas were determined based on nitrogen adsorption/desorption isotherms recorded on a NOVA 3000e (Quantachrome). The standard multipoint BET (Brunauer-Emmett-Teller) model was applied and the pore-size distribution was calculated from the desorption branch of the isotherm using the BJH (Barrett-Joyner-Halenda) method. Prior to measurements, the samples were pretreated in vacuum at 150°C for 24 h.

3.2.2 Raman spectroscopy

For Raman measurements three different laser systems were used, a tuneable Raman system for UV measurements (256.7 and 385 nm) [100], and two Vis-Raman setups (514.5 and 633 nm) [96, 101, 102]. The first Vis-Raman setup consisted of an argon ion laser (Melles Griot) with an excitation wavelength of 514.5 nm, which will be referred to as 515 nm in the following. The transmission spectrometer included a SuperNotch Plus filter (Kaiser Optical, HL5R) and an electronically cooled CCD detector (256 x 1024 pixels). For calibration an argon lamp and cyclohexane were taken. The spectrometer's resolution was 5 cm^{-1} with a wavelength stability better than 0.5 cm^{-1}. Cosmic ray removal and auto new dark correction were performed as online corrections. For silica supported vanadium oxide samples the laser power was adjusted to 4.7 mW and an acquisition time of 2x600s was chosen. In the case of ceria, measurements were executed with a laser power of 1.5 mW and an acquisition time of 20x20 s.

The UV-Raman setup included an all solid-state, tuneable laser system, which comprises an titanium-sapphire oscillator, an Evolution-15 pump laser, and an harmonics package with frequency doubling crystals.[103] The Evolution-15 pump laser (1053 nm) is a Nd:YLF laser, which itself is diode pumped. A closed loop dissipates the waste heat and maintains the wavelength of the twelve AlGaAs laser diode arrays to ensure the maximum absorption of the pump light in the gain medium. The Ti:sapphire oscillator is optically pumped by the second harmonic output of the Evolution-15 laser at 527 nm and is made to lase from 770 nm to 900 nm (linewidth $< 1\ cm^{-1}$). For the performed measurements, the laser wavelength is adjusted to 770.1+0.1 nm. Barium borate (BBO) and Lithium triborate (LBO) crystals are used for nonlinear frequency conversion. Second harmonic generation (SHG, 385.0 nm) and third harmonic generation (THG, 256.7 nm) requires the two input polarizations to be parallel to each other. This is crucial for the generation of the THG beam as the fundamental and SHG radiation have to be aligned to be collinear with the beam waist located in the plane of the THG crystal. The THG output beam, SHG input beam and fundamental input beam are then separated via a dichroic mirror reflecting the SHG and THG in different angles. The selected excitation wavelength is subsequently transmitted via a confocal setup onto the reaction cell. The mirror setup was previously installed by Dr. Waleska for the purpose to minimise radiation loss. Moreover, an increase of the spot size was implemented obtained by de-focusing the laser radiation. This is highly relevant as especially UV radiation may lead to photodecomposition and radiation damage of the samples. More details can be found in [100]. In addition to the constructional considerations, the samples were continuously moved during the measurements using an xy-stage or operated in a fluidised bed mode.

The Raman scattered light is dispersed and detected by a triple-stage spectrometer (Princeton Instruments, TriVista 555) with an attached nitrogen-cooled CCD camera (Princeton Instruments, Spec10:2kBUV, 2048 x 512 pixels). Subsequently, the data is transferred to the S&I TriVista Software. To remove the intense Rayleigh scattering the spectrometer is employed in subtractive mode. Thereby, the first and second stages operate as a bandpass filter (groove density: 300 g/mm), whereas the third stage (groove density: 2400 or 3600 g/mm) disperses the spectrum onto the CCD. The linear dispersion is calculated according to

$$D = \frac{d\lambda}{dx} = \frac{10^6 \cdot \cos\beta}{m \cdot N \cdot F} \tag{3.1}$$

As the diffraction angle β shows a dependency on the wavelength λ, the linear dispersion is a non-linear function varying across the CCD. Linear dispersion D increases while λ increases. Hence, at low wavelengths the spectral resolution is approximately 0.914 cm^{-1} per pixel and at high wavelengths approximately 0.798 cm^{-1} per pixel. Consequently, the spectral resolution is specified as 1 cm^{-1}. The respective combination of gratings for the 256.7 and 385 nm excitation wavelengths is shown in table 3.2. Best stray light rejection is obtained with narrow first stage entrance slit (Slit Entrance 1) and second intermediate slit (Slit Entrance 3). The first intermediate slit (Slit Entrance 2) is opened to around 3500 to 4000 μm in order to allow a wide bandpass to pass through.

Table 3.2: Overview of grating combinations. The unit g/mm refers to the groove density.

System Parameter	385 nm	256.7 nm
Grating Stage 1	300 g/mm	300 g/mm
Grating Stage 2	300 g/mm	300 g/mm
Grating Stage 3	2400 g/mm	3600 g/mm
Slit Entrance 1	200 μm	200 μm
Slit Entrance 2	3500 μm	4000 μm
Slit Entrance 3	200 μm	200 μm

The wavelength or, more precisely, the offset position of the gratings was calibrated with a mercury spectral lamp and the evaluation was performed with cyclohexane and benzonitrile. The results are summarised in table 3.3 for 256.7 nm and in table 3.4 for 385.0 nm reflecting the non-linearity of dispersion, which cannot be completely compensated via calibration. However, a slight tilting of the camera may also be the reason. Reference positions were taken from [104].

It might further be noted that wavelength determination for the Raman shift calculation is crucial as the final emitted wavelength fluctuates between 770.1 and 770.2 nm. For example, for THG generation the laser wavelength may either correspond to 256.700 nm in the first case or to 256.733 nm in the second case. The variation of 0.033 nm may result in a Raman shift deviation of 4.4 cm^{-1}. Best Raman shift accuracies, like <0.6 cm^{-1} between 800 and 1300 cm^{-1}, are obtained in the proximity of the central wavenumber.

Table 3.3: Evaluation of wavelength calibration via cyclohexane and benzonitrile for 256.7nm excitation

	Central wave-number (cm^{-1})	Nominal vibration (cm^{-1}) [104]	Actual vibration (cm^{-1})	Deviation (cm^{-1})
Cyclo-hexane	1100	384.1	386.46	2.36
		426.3	429.65	3.35
		801.3	801.84	0.54
		1028.3	1028.88	0.59
		1157.6	1157.98	0.38
		1266.4	1266.40	0.00
		1444.4	1442.32	-2.08
	3100	2852.9	2855.09	2.18
		2923.8	2926.66	2.86
		2938.3	2936.52	-1.78
Benzo-nitrile	1100	1598.9	1596.12	-2.78
	2100	1598.9	1605.22	6.32
	2100	2229.4	2230.61	1.21

Table 3.4: Evaluation of wavelength calibration via cyclohexane for 385.0 nm excitation

	Central wave-number (cm^{-1})	Nominal vibration (cm^{-1}) [104]	Actual vibration (cm^{-1})	Deviation (cm^{-1})
Cyclo-hexane	1100	801.3	803.54	2.24
		1028.3	1028.78	0.48
		1157.6	1158.01	0.41
		1266.4	1264.41	-1.99
		1444.4	1442.51	-1.89
	2800	2852.9	2853.01	0.11
		2923.8	2925.26	1.46
		2938.3	2939.65	1.35

Raman experiments with silica supported vanadium oxide were excited with a THG laser power of 6 to 9 mW at the sample. As the fundamental wavelength of 770 nm is at the limit of the tuning range, the maximum laser power of the THG could not always be guaranteed. Laser power was adjusted to 6 mW for excitation at 385 nm. Prior to the measurement, boron nitride was used in order to find the optimum focus position. For 256.7 nm excitation, spectra were acquired for 600 s with 1 to 2 accumulations at a central wavenumber of 1100 and 2100 cm^{-1}, and 5 accumulations at 3100 cm^{-1}. Furthermore, cosmic ray removal required an additional measurement of 600 s for each region. In the case of 385 nm, central wavenumber positions had to be set to 880, 1820 and 2820 cm^{-1} in order to cover the full range.

The data was processed via Matlab R2015a, which included background subtraction, smoothing with a moving-average filter, merging, and normalisation, if necessary. The change of the order of performed processing steps did not have any significant effect on the final spectra. Stagging points for background subtraction had to be adapted for each spectrum and handled with great care. The template of the Matlab script was gratefully provided by Dr. Waleska. Final plotting and fitting were performed via Origin v8.0951.

Raman spectra of ceria-based samples were recorded in a similar manner. The laser power at the sample was set to 5.0 mW for 256.7 nm, 3.8 mW for 385 nm, and 1.5 mW for 515 nm in order to consider an equal photon flux. The data was recorded as various consecutive frames without any internal software processing. The cosmic ray removal was performed for each frame via a Matlab program followed by a background subtraction of the averaged counts. In addition to 256.7 nm, 385 nm and 515 nm, ceria was characterised with a He-Ne laser emitting 633 nm with a set laser power of 1.2 mW. More details on the setup can be found in Hess [102].

3.2.3 UV-vis spectroscopy

UV-vis spectroscopic measurements were performed with a Jasco V-770 UV-vis/NIR spectrometer in the range between 200 and 1100 nm with 5 accumulations. The double-beam photometer consists of a halogen and deuterium lamp. Spectra were recorded via a photomultiplier tube and a Peltier-cooled PbS element and obtained in absorbance units. A Praying Mantis accessory (Harrick Scientific Products Inc.) was used for the application in diffuse reflection (DR). The dehydrated bare SBA-15 support at room temperature served as the white standard for silica supported vanadium oxide samples and dehydrated magnesium for ceria supported vanadium oxide samples. Spectra were plotted in Kubelka-Munk (KM) units, which are calculated according to the following equation

$$F(R_\infty) = \frac{(1-R_\infty)^2}{2R_\infty} \tag{3.2}$$

, whereas R_∞ as the diffuse reflectance of an infinitely thick powder is equal to the reflectance R. This, in turn, can be expressed by the relation of the incident and diffuse reflected intensity (I_0 and I) and therefore to the absorption A.

$$R = \frac{I}{I_0} = (10^A)^{-1} \tag{3.3}$$

Band edge energies are determined by plotting the quantity $(\mathrm{F(R_\infty)h}\nu)^{1/\mu}$ versus the photon energy $\mathrm{h}\nu$, also referred to as Tauc-plot. As an indirect transition is assumed, $\mu = 2$ was taken. The point of intersection of the tangent through the curve‘s turning point corresponds to the respective edge energy. Previously, Nitsche et al. [105] reported on the linear correlation between the number of V-O-V bonds and the band edge energy providing a reference for the obtained results in this work. Error estimation was performed by the maximal variation of the adjacent tangent.

3.2.4 DRIFT spectroscopy

Diffuse reflectance infrared Fourier transform (DRIFT) spectra were detected between 850 and 5000 cm^{-1} on a Bruker Vertex 70 spectrometer equipped with a liquid nitrogen (LN)-cooled mercury cadmium telluride (MCT) detector. The *in situ* cell was closed by a Praying Mantis diffuse reflection accessory (Harrick Scientific Products Inc.). Prior to measurements, potassium bromide (KBr) was dehydrated at 12.5% O_2 / 87.5% N_2 for 30 min and reference spectra were obtained at various temperatures. Additional background spectra were taken for a gas composition of 12.5% C_3H_8/ 12.5% O_2 / 75% N_2 in order to subtract gas phase contributions.

3.3 Catalytic measurements and *operando* experiments

This section describes the experimental procedures for the majority of experiments in this work. If any variation was applied, it will be explicitly stated. Given temperatures in these descriptions are actual measured temperatures. For the relation to the set temperature, the reader is referred to the next chapter. Also details on the used *in situ/operando* cells, named as Linkam cell and Harrick cell reactor, can be found there.

3.3.1 Propane ODH with O_2

The experimental runs were carried out at reaction temperatures from 320 to 593°C using the Linkam cell reactor. Prior to the study, the catalyst (SBA-15: 14-15 mg, CeO_2: 70 mg; particle size: 200-300 μm) was dehydrated at 502°C under oxidative conditions (12.5% O_2 / 87.5% He). Propane and oxygen were fed into the gas stream with a ratio of 1:1 (12.5% C_3H_8 / 12.5% O_2 / 75% He) at a total flow of 40 ml$_n$/min. The GHSV is the ratio of gas flow rate in standard condition to the volume of the bed. By using the bulk density of SBA-15 and CeO_2, the GHSV was determined to be approximately 10 000 1/h for SBA-15 and 200 000 1/h for CeO_2. The catalytic performance was continuously monitored via online gas chromatography. The temperature was stable for at least 25 min before each chromatogram. Two measurements were performed at each temperature. Comparable studies were conducted with SBA-15, blank CeO_2, and the empty cell. A homogeneous gas phase contribution is expected above 550°C.[44] Propane conversion X and propene selectivity S were calculated according to the following equations:

$$X = 1 - \frac{n_{C_3H_8}}{n_{C_3H_{8,0}}} \tag{3.4}$$

$$S = \frac{n_{C_3H_6}}{n_{C_3H_{8,0}} - n_{C_3H_8}} \tag{3.5}$$

The inlet propane amount $n_{C_3H_{8,0}}$ was determined by the outlet amount of products.

$$n_{C_3H_{8,0}} = n_{C_3H_8} + n_{C_3H_6} + \frac{1}{3}n_{CO} + \frac{1}{3}n_{CO_2} + \frac{2}{3}n_{C_2H_6} + \frac{2}{3}n_{C_2H_4} + \frac{1}{3}n_{CH_4} \tag{3.6}$$

The calculated amount $n_{C_3H_{8,0}}$ was compared with the expected amount $n_{C_3H_{8,0,MFC}}$, which was dosed via the mass flow controllers (MFCs). The carbon balance value (CB) was specified as

$$CB = 1 - \frac{n_{C_3H_{8,0,MFC}}}{n_{C_3H_{8,0}}} \tag{3.7}$$

In this respect it is noted that the measurement uncertainty of the carbon balance itself is 2% due to the measuring uncertainty of the amount of propane. Further details can be found in the following chapter. The selectivity towards propylene was determined to be 20% - 30% for the empty cell, independent of conversion. The support SBA-15 does not show any significant activity in comparison to values obtained for the empty cell. In a separate experiment, the temperature dependent selectivity was studied. The average of each product x, $\bar{n}_{x,SBA-15}$, was determined for SBA-15 (including the cell activity), and subtracted from the measured amount of product n_{x,VO_x} in the presence of the supported vanadium oxide catalyst.

$$n_{x,corr} = n_{x,VO_x} - \bar{n}_{x,SBA-15} \tag{3.8}$$

The total amount of products $n_{tot,corr}$ (corr is short for corrected) was calculated according to the following equation:

$$n_{tot,corr} = n_{C_3H_6,corr} + \frac{1}{3}n_{CO,corr} + \frac{1}{3}n_{CO_2,corr} + \frac{2}{3}n_{C_2H_6,corr} + \frac{2}{3}n_{C_2H_4,corr} + \frac{1}{3}n_{CH_4,corr} \tag{3.9}$$

The adjusted selectivity and conversion of the vanadium oxide catalyst is obtained via

$$S_{VO_x} = \frac{n_{C_3H_6,corr}}{n_{tot,corr}} \tag{3.10}$$

$$X_{VO_x} = \frac{n_{tot,corr}}{n_{C_3H_8,0}} \tag{3.11}$$

The turn-over frequency (TOF) was determined via the number of converted moles of propane divided by the moles of vanadium and time. The unit is 1/s.

Operando studies were conducted as exemplarily shown for a gas composition of 14% C_3H_8 / 12% O_2 / 74% He in figure 3.1, which represents the online GC measurement of an *operando* Raman experiment.

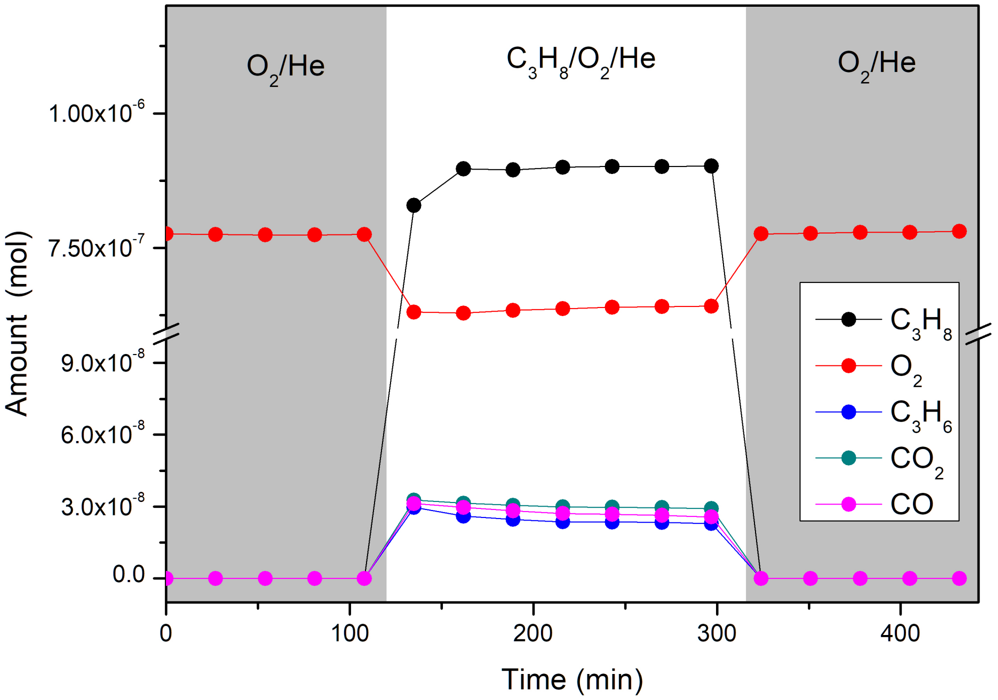

Figure 3.1: Example of a typical *operando* Raman experiment for propane ODH with O_2. The amount of respective gas phase contributions is plotted versus time.

Prior to reaction conditions, the 0.6 VO_x/SBA-15 catalyst (particle size: 200 - 300 μm, 14-15 mg) is dehydrated for one hour under oxidative conditions and a spectrum named as “Prior to Reaction” is taken. After waiting for 20 min in order to obtain steady state conditions, a spectrum under reaction conditions (“During Reaction”) is recorded. Likewise, a Raman spectroscopic measurement of the reoxidised catalyst is executed after 20 min in a mixture of O_2/He (“After Reaction”). Besides the overoxidation products CO_2 and CO, low amounts of ethane, ethylene, and methane were detected but not plotted here. While Raman measurements were performed in the Linkam cell, the Harrick cell was used for corresponding UV-vis and DRIFT spectra. The overall duration of the *operando* experiments depended on the respective time required for the detection of the necessary data. Furthermore, it should be noted here that the operation of the fluidised bed mode was only applied in conjunction with the Linkam cell.

Operando UV-vis experiments were recorded between 200 nm and 1100 nm using the Jasco V-770 spectrometer and the Harrick cell HVC-MRA. Around 15 mg of the vanadium oxide sample (0.6 VO_x/SBA-15, particle size <200 μm) was dehydrated for one hour at oxidative conditions (12.5% O_2/ 87.5% N_2, total flow: 40 ml_n/min). Dinse et al. [44] reported similar selectivity–conversion trajectories for different particle sizes. N_2 was used as an inert gas in order to obtain a set temperature of 630°C, corresponding to an actual surface temperature of 408°C. More details on the effect of the inert gas will be presented in the next chapter. After recording the UV-vis spectrum of the dehydrated catalyst, C_3H_8 was added to the gas mixture for *operando* conditions (12.5% C_3H_8 / 12.5% O_2/ 75% N_2, total flow: 40 ml_n/min). The UV-vis spectrum during reaction conditions was taken after 20 min, and the GC was started with two runs in total. Subsequently, the catalyst was reoxidised under oxidative conditions for 20 min. Spectra were recorded with five accumulations. SBA-15 served as a white standard.

Complementary *operando* IR spectra were taken using the Bruker Vertex70 spectrometer and the Harrick cell HVC-DRP-4. KBr was dehydrated for 30 min and recorded at a set temperature of 688°C for background subtraction. The catalyst 0.6 VO_x/SBA-15 (particle size <200 μm) was dehydrated under oxidative conditions (12.5% O_2/ 87.5% N_2, total flow: 40 ml_n/min) for one hour before taking the corresponding spectra at a set temperature of 688°C (surface temperature of 409°C). Propane was added to the gas mixture, in order to obtain a gas composition of 12.5% C_3H_8 / 12.5% O_2/ 75% N_2 at a total flow of 40 ml_n/min. The acquisition time was set to 20 min.

Additional experiments were performed while varying the temperature and the gas composition. The interference experiment is similar to a “typical” *operando* experiment. After *operando* conditions, oxygen is turned off in order to study the catalyst behaviour under propane reducing conditions. Moreover, the redox properties of the vanadium oxide catalyst were explicitly studied under hydrogen and propane reductive environments in dependency of the temperature.

3.3.2 Propane ODH with CO_2

Experimental runs were carried out for 0.6 VO_x/SBA-15 samples as previously described. The reaction was performed at temperatures between 320 and 593°C in the Linkam cell reactor. Prior to reactive conditions (12.5% C_3H_8 / 12.5% CO_2 / 75% He), the catalyst was dehydrated for one hour at a helium flow of 40 ml_n/min. As a reference, the reaction was also executed in the absence of CO_2.

In the case of CeO_2, samples (70 mg, particle size: 200-300 μm) were tested for 5 h at reaction conditions (14% C_3H_8/ 13% CO_2/ 73% He, total flow: 37 ml_n/min, temperature: 550°C) after dehydration in He to allow the observation of catalyst deactivation.

Propane conversion X and propene selectivity S were obtained by the detected outlet amount of products as specified in the following equations.

$$X = 1 - \frac{n_{C_3H_8}}{n_{C_3H_{8,0}}} \tag{3.12}$$

$$S = \frac{n_{C_3H_6}}{n_{C_3H_{8,0}} - n_{C_3H_8}} \tag{3.13}$$

$$n_{C_3H_{8,0}} = n_{C_3H_8} + n_{C_3H_6} + \frac{2}{3} n_{C_2H_6} + \frac{2}{3} n_{C_2H_4} + \frac{1}{3} n_{CH_4} \tag{3.14}$$

In a similar manner, the conversion of CO_2 was determined to

$$X_{CO_2} = 1 - \frac{n_{CO_2}}{n_{CO_{2,0}}} \tag{3.15}$$

, while the amount of inlet CO_2 ($n_{CO_{2,0}}$) is calculated via the following equation:

$$n_{CO_{2,0}} = n_{CO_2} + n_{CO} \tag{3.16}$$

The experimental design did not allow the quantification of the amount of deposited carbon. However, the CB value enabled a rough evaluation of potential coke formation during the reaction.

For silica supported vanadium oxide, the typical *operando* experiment was extended with a pretreatment procedure (see figure 3.2). The samples were dehydrated for one hour at 502°C under oxidative conditions (12.5% O_2/ 87.5% He). Raman spectra were taken after increasing the temperature to 547°C, which is correlated to a surface temperature of 446°C. After flushing the reactor and tubes with He, the catalyst was reduced with 7.5 % H_2 mixed in Ar and preoxidised with either 12.5% CO_2/ 87.5% He or 12.5% O_2/87.5% He. *Operando* conditions consisted of 12.5 % C_3H_8 / 12.5 % CO_2/ 75 % He for both experiments. Afterwards, the sample was regenerated under a flow of 12.5% CO_2/ 87.5% He. In this case, the Raman region around the central Raman shift of 3100 cm^{-1} was recorded first to give the catalyst more time to regenerate as the measurement in this region takes one hour.

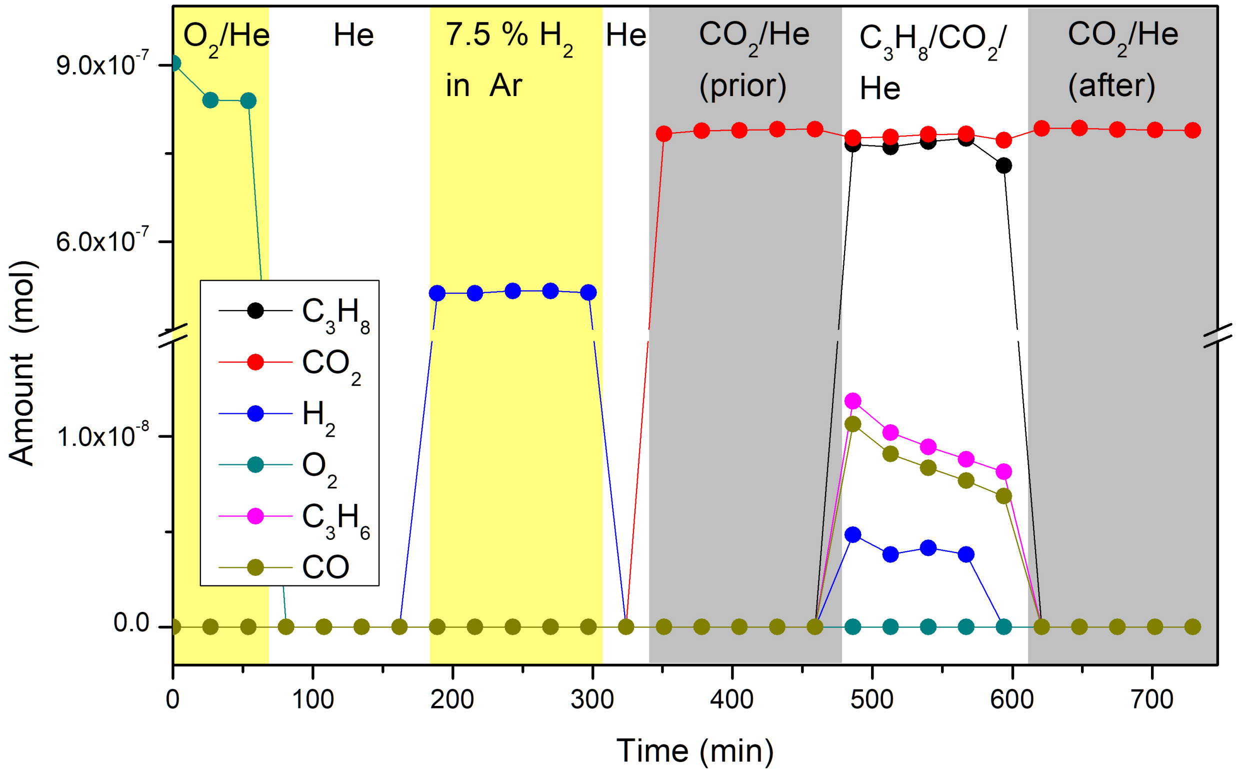

Figure 3.2: Example of the *operando* Raman experiment for propane ODH with CO_2. The amount of respective gas phase contributions is plotted versus time.

3.3.3 Ethanol ODH

The activity of ceria supported vanadium oxide was studied in the ODH of ethanol between 73 and 147°C in comparison to blank ceria. The samples (0.15 - 0.2 g) were dehydrated for one hour at approximately 500°C under oxidative conditions (8% O_2/ 92% N_2, 50 ml_n/min). After cooling down to 73°C, ethanol was added to the gas stream by bubbling N_2 through a saturator cooled to –6°C. Based on the Antoine equation, the final composition was determined to be 1% EtOH/ 8% O_2/ 91% N_2. The temperature was raised by approximately 9°C up to 147°C. The outlet gas phase was continuously measured via FTIR spectroscopy using the Vertex 70 spectrometer together with a RT-DLaTGS (room-temperature deuterated L-alanine-doped triglycine sulfate) detector. Conversion and selectivity were calculated on the basis of FTIR gas phase analysis by the amount of products. Corresponding calibration data was taken from Waleska [100].

Operando Raman and *operando* UV-vis spectra were recorded during reaction conditions at 100°C.

4 *Operando* Raman GC/FTIR setup

The present chapter describes the development of the *operando* GC/FTIR setup, which is combined with a tuneable laser system. *Operando* Raman spectra can be taken with a great variety of excitation wavelengths ranging from 193 to 900 nm (except for $450<\lambda<770$ nm). Such an *operando* setup is, to my knowledge, the first of its kind. In 2008, Martínez-Huerta et al. [106] reported an *operando* Raman-GC setup, which was tested in ethane ODH. Raman spectra were obtained with an excitation wavelength of 515 nm.

The installed *operando* Raman GC/FTIR setup, outlined here in detail, has great potential to be applied in a variety of experiments and reactions. Its possibilities were not completely exploited in this work. The following description starts with an overview of the setup. Afterwards, the employed commercial *in situ* cells are evaluated for their application in high-temperature reactions such as alkane ODH. Finally, the two acquisition devices for the gas phase composition, the FTIR spectrometer and the gas chromatograph, are introduced. Their implementation is addressed in the context of the ODH with ethanol and propane.

4.1 *Operando* setups

The previous setup, which combined multiwavelength Raman spectroscopy with FTIR gas phase analysis, had been installed by Dr. Waleska as described in detail in [100]. In principle, the extension and modification of the setup performed in this work allows the investigation of the following reactions. Figure 4.1 shows a scheme of the realised installation.

- Oxidative deyhdrogenation of propane with O_2 and/or CO_2 (Use of CO_2 as a promoter or soft oxidant)
- Oxidative dehydrogenation of ethanol with O_2 and/or CO_2 (Use of CO_2 as a promoter or soft oxidant)
- (Thermal) Dehydrogenation
- Reverse water gas shift reaction

The gases with the following specifications/purities were utilised:

- Nitrogen 5.0, Westfalen AG
- Helium 5.0, Westfalen AG
- Hydrogen (7.5%) in Argon, Air Liquide
- Oxygen 5.0, Westfalen AG
- Propane 3.5, Westfalen AG
- Carbon Dioxide, 5.0 Westfalen AG

The feed is controlled via mass flow controllers (MFC El Flow Select, F-201 CV and F-201-CRAA, Software: FlowDDE2) by Bronkhorst, calibrated to a maximum flow of 150 ml_n/min. Their performance is specified in table 4.2. They are vertically mounted on a plate together with their respective closing valves, particle filters, and check valves. Ethanol can be added to the gas mixture by bubbling an inert gas (N_2 or He) through a saturator preventing an undesired solution of O_2 or CO_2

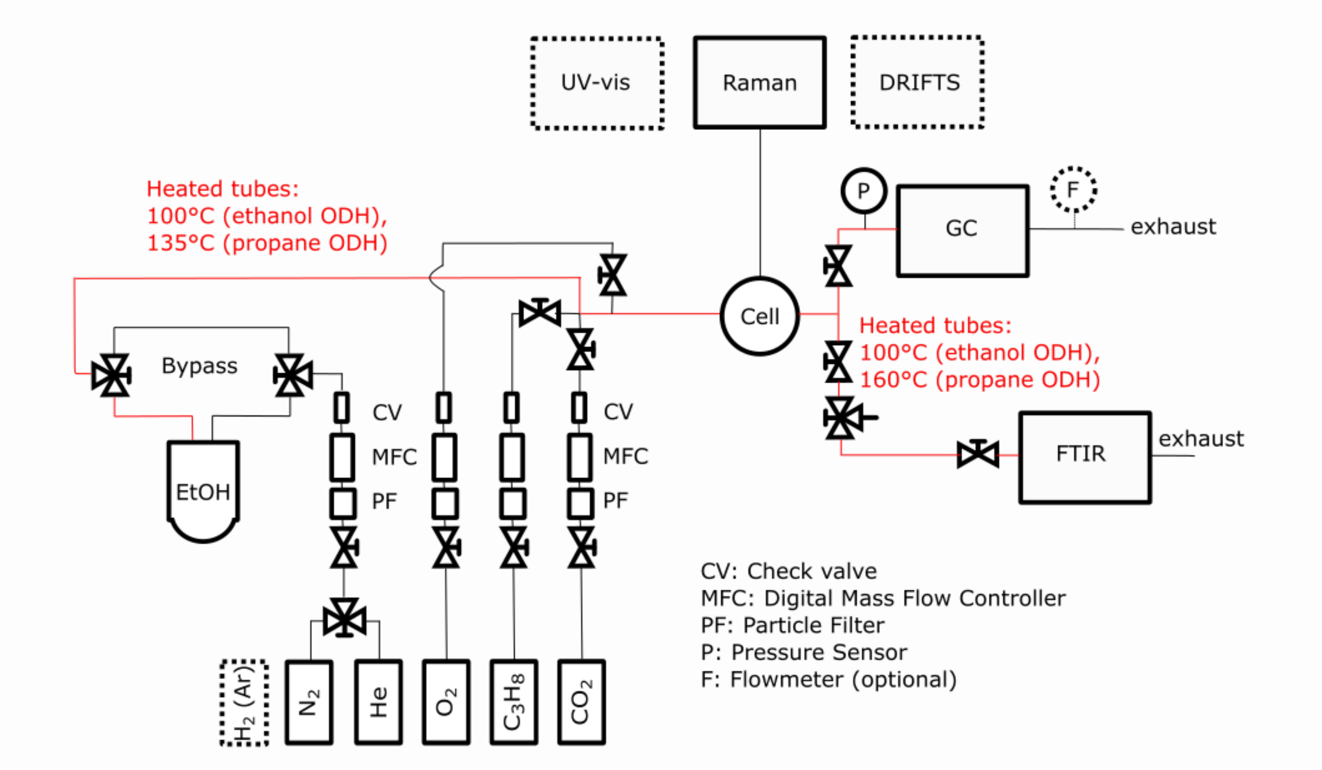

Figure 4.1: The novel *operando* Raman GC/FTIR setup for propane and ethanol ODH developed in this work

in the liquid ethanol. The ethanol concentration in the gas composition can be determined via the Antoine equation. At the mixing point, closing valves are installed to inhibit possible (re-)diffusion. For the ODH with ethanol, stainless steel tubes (1/8 “) are heated to 100°C to prevent ethanol and water condensation. A temperature of 160°C is set after the reaction cell for the ODH with propane in order to prevent the polymerisation of the possible by-product acrolein. Before entering the reaction cell, the gas mixture is preheated to approximately 135°C. Heated tubes are marked in red. Gas phase analysis can be performed via a mobile FTIR gas phase spectrometer, and/or a stationary gas chromatograph. A needle valve regulates the splitting of the gas flows, which can be measured via a mobile flow meter (Agilent, ADM Flow Meter, Model No. G6691A). A flow of 3-5 ml/min has to be guaranteed over the GC for accurate measurements to be taken. The installed pressure transducer (P-05, 0-2.5 bara, internal diaphragm) by Wagner Mess- und Regeltechnik allows the absolute pressure at the gas inlet of the GC to be determined. Its necessity will be explained in subsection 4.3.2. For Raman measurements, the reaction cell is mounted on a height-adjustable plate. The *operando* setup is easily adaptable for UV-vis and DRIFTS characterisation techniques.

Table 4.1: Specification of MFC model F-201 CV. Rd and FS are short for Reading and Full Scale.

Accuracy	±0.5 % Rd plus ±0.1 % FS
Repeatability	$< \pm 0.2$ % Rd
Attitude sensitivity	max. error at 90° off horizontal ±0.2 % FS at 1 bar, typical N_2
Ranges (air)	nominal 0.8...100 ml_n/min minimum 0.8...40 ml_n/min

4.2.1 Commercial *in situ*/*operando* cells

In total, three different commercial *in situ* cells were applied. Based on figure 4.2, the design of the Linkam and Harrick cell will be described in detail. The drawings are mainly based on the figures by Filtschew [98] and Waleska [100].

The *in situ* cell CCR1000 by Linkam Scientific Instruments Ltd. allows temperatures up to 1000°C. The water cooling, a Pike Technologies Recirculator, keeps the stage body at a safe temperature. A maximum flow of 50 ml/min is recommended. The gas mixture enters the reactor via a 1/16" tube and is heated while rising up inside the cell. The heating filament is positioned spirally inside a ceramic casing. An integrated thermocouple, a metal ring, is directly underneath the sample holder. The sample is deposited on to a filter sheet of alumina /silica (Al_2O_3 96% /SiO_2 4%) non-woven fabric in the ceramic sample holder. Some experiments were also performed with their new filter sheet made out of ZrO_2/Y_2O_3 (stabilised with 8% Yttria). The sample holder has a diameter and a height of approximately 7 mm, respectively. Thus, it protrudes past the ceramic casing by approximately 2 mm. As will be demonstrated in the next subsection, the Linkam cell has a better temperature profile in the reactor bed. Hence, it was used for activity and Raman measurements. In regard to the performance of the activity study, the variation of the gas hour space velocity is restricted, primary due to the limitation of the maximum flow and the available MFC devices. Spectroscopic characterisation requires the presence of a suitable window. While for Raman measurements in the visible range a quartz window (22 x 1 mm) is placed on top of the o'ring, a calcium fluoride window (CaF_2, Korth Kristalle GmbH, 22 - 0.2 mm x 1 ± 0.1 mm; optically polished) is the best choice for the UV range due to the respective Raman signals of the window. More details can be found in Waleska [100]. As the window protrudes, the stage lid has to to be slightly pressed onto the window to guarantee a leak free operation. The CaF_2 window turns out to be quite sensitive when high temperatures are applied. Although its melting point is specified to be 1418°C, the thermal expansion corresponds to $18.9 \cdot 10^{-6}$/K (298K) [107]. Hence, the heating rate has to be minimised to around 5-10°C/min, and the stage lid cannot be closed too tight. In contrast to, e.g., quartz, the joint surfaces of CaF_2 window experience shearing due to the thermomechanical tensions. In order to prevent hot spots and photodecomposition caused by UV excitation, the sample should be continuously moved. Throughout the course of this work, the application of the fluidised bed mode was employed for silica and ceria supported vanadium oxide samples. 200 to 300 μm particles are constantly mixed in the reactor bed by the back pulse of a membrane pump (Typ 123, SN: 53203625) by WISA, which is installed in series with the reaction cell. The fluidised bed can be controlled by a regulating transformer (0-230 VAC). It must be noted that, as the gas flows through the membrane pump, the medium comes in contact with EPDM (ethylene propylene diene monomer) and PVDF (polyvinylidene fluoride). These materials are not resistant to hydrocarbons and temperatures above 100°C. These specifications are considered quite critical for long-term operation in alkane ODH. Recently, Filtschew [98] successfully implemented the technique for CeO_2. In contrast, SBA-15 has a comparable low density and sensitivity to moisture. Depending on the temperature and gas composition, hills and valleys may be formed with particles sticking to the sample holder wall. Hence, the optimal focus position during the spectroscopic measurement can vary throughout a Raman experiment.

For UV-vis and DRIFTS measurements, two High Temperature Reaction Chambers (HVC) by Harrick Scientific Products Inc.

were employed. The HVC-MRA and HVC-DRP-4 model do not show any apparent constructional differences, however, the latter was acquired earlier. The Harrick cell allows temperatures of up to 910°C (under vacuum) and can be applied up to a maximum flow of 100-150 ml/min. The stage incorporates a cartridge heater and an integrated thermocouple located in its proximity. While for UV-vis measurements the sample is deposited in a sample cup made out of high temperature steel, a ceramic cup (corundum, Al_2O_3) is taken for DRIFT spectroscopy. A grid covering the hole of the sample cup allows the gas to flow through the sample. The cell is used in conjunction with the Praying Mantis Accessory. In UV-vis-NIR configuration, a dome with two SiO_2 windows and one glass observation window is used, while for DRIFT measurements, KBr windows are required.

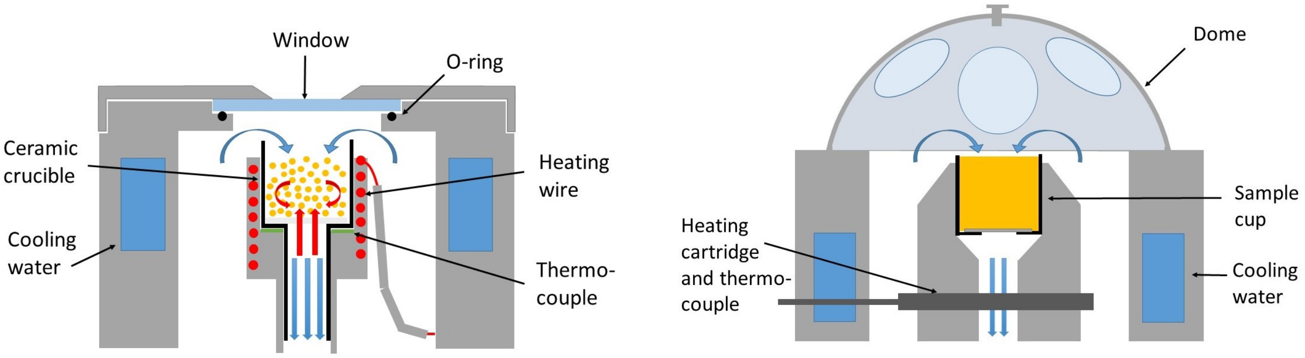

Figure 4.2: Scheme of the Linkam (left) and Harrick (right) cell [adapted from Waleska [100] and Filtschew [98]]. The operation in fluidised bed mode is indicated for the Linkam cell by the respective arrow directions.

4.2.2 Sample temperature

As already mentioned, the actual sample temperature may differ from the set controller temperature [79]. Previously, Dr. Waleska measured the sample surface temperature via the Raman red shift of the intense Boron nitride (BN) signal at 1360 cm^{-1}, as well as directly in SBA-15 with a thermocouple for the Linkam and Harrick cell.[100] A significant temperature deviation was recorded. In order to study the temperature gradient of the Linkam cell more precisely, and additionally in a closed configuration, a stainless-steel plate with a hole was used instead of the spectroscopic window. The thermocouple was inserted through the hole, allowing for an accurate insertion depth inside the sample holder. Its fixation in the centre of the cell is further guaranteed with a teflon-plate (melting point: 327°C) as shown in figure 4.3. Temperature measurements were taken at the bottom (h = 1 mm) and close to the surface (h = 3 mm) of the sample. Heights are specified herein as the distance to the non-woven. The sample holder was filled up to less than two thirds of its height with approximately 15 mg of SBA-15, and with 0.15 - 0.2 g CeO_2.

Figure 4.4 illustrates the results for SBA-15 for the open and closed cell, in comparison to the reference data taken from Waleska [100]. The temperature profile was studied below 400°C in order to prevent the melting of the teflon-plate. Ref1 and Ref2 correspond to the direct thermocouple measurement in SBA-15 (5 mm deep in SBA-15) and the Raman spectroscopic method with BN, respectively. It is noted that the exact thermocouple position is an important factor as

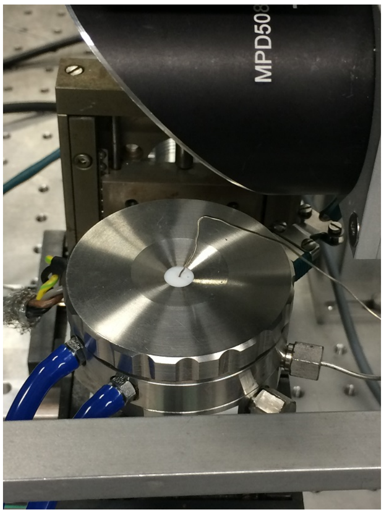

Figure 4.3: Temperature measurements for the Linkam cell with a self-made stainless-steel plate placed instead of the spectroscopic window. The thermocouple is inserted through a hole and additionally fixed through a teflon-plate.

the reference measurement with SBA-15 could not be reproduced. Most probably, the thermocouple was located deeper within the sample powder in this work. While closing the cell, a constant N_2 (40 ml_n/min) was applied. The bottom temperature showed a significant decrease, which can be explained by constant heat removal of the flowing gas. The measured surface temperature revealed a further temperature drop. As CeO_2 and SiO_2 are both poor heat conductors, a similar temperature behaviour was determined in the open cell. More data points were taken in the low temperature region for CeO_2 due to its application in the ODH with ethanol (<200°C). According to the cell design, the following assumptions may be reasonable. The integrated circular thermocouple takes the temperature from the outer edge of the ceramic sample holder, causing the heat energy to be emitted along the ceramic casing. Thus, the sample may have the highest temperature at the inner edge of the crucible. The temperature likely drops towards the centre and towards the surface with its coolest point in the centre of the powder surface. Hence, the catalytic activity of a sample may actually be referred to its highest temperature. In contrast, spectroscopic data is obtained from particles at the surface.

Additionally, the effect of the respective choice of inert gas was studied as can be seen on the left of figure 4.5. N_2 has a thermal conductivity of 0.02583 W/(mK) (25°C) in comparison to Helium with 0.150 W/(mK) (25°C). The actual temperature showed a significant increase when using Helium. In this case, the effect could be unambiguously identified because the measurements were taken at the same thermocouple position. The operation in fluidised bed mode with SBA-15, consisting of 200 to 300 μm particle size, slightly promoted a homogeneous temperature distribution (see right panel of figure 4.5). It is assumed that particles are heated while being at the bottom and cooled down while circulating to the surface. Hence, the actual particle temperature at the time of the spectroscopic measurement cannot clearly be determined here. Throughout the dissertation, the activity data refers to the temperature measured at the bottom, also called reaction temperature here, while the Raman spectroscopic data considers the actual surface temperature.

In the case of the Harrick cell, the thermocouple can be placed in a better position, which allows the temperature measurement at an insertion depth of 1 mm to be taken without any attachment. Both Harrick cell models were compared with each other as shown in figure 4.6 (open configuration). Reference data was likewise taken from [100]. It is noted

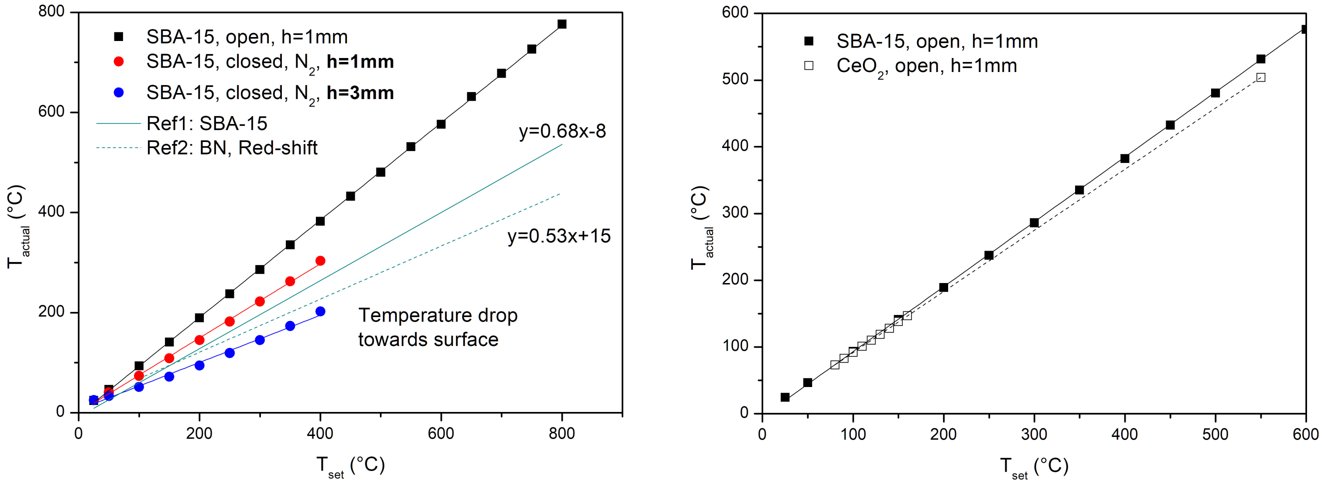

Figure 4.4: Correlation between the set temperature and the actual temperature in the Linkam cell. The temperature was measured with (left) an open and closed cell (N_2 flow: 40 ml$_n$/min), and (right) in comparison to CeO_2. Heights are specified as the distance to the bottom (non-woven). References Ref1 and Ref2 were taken from [100].

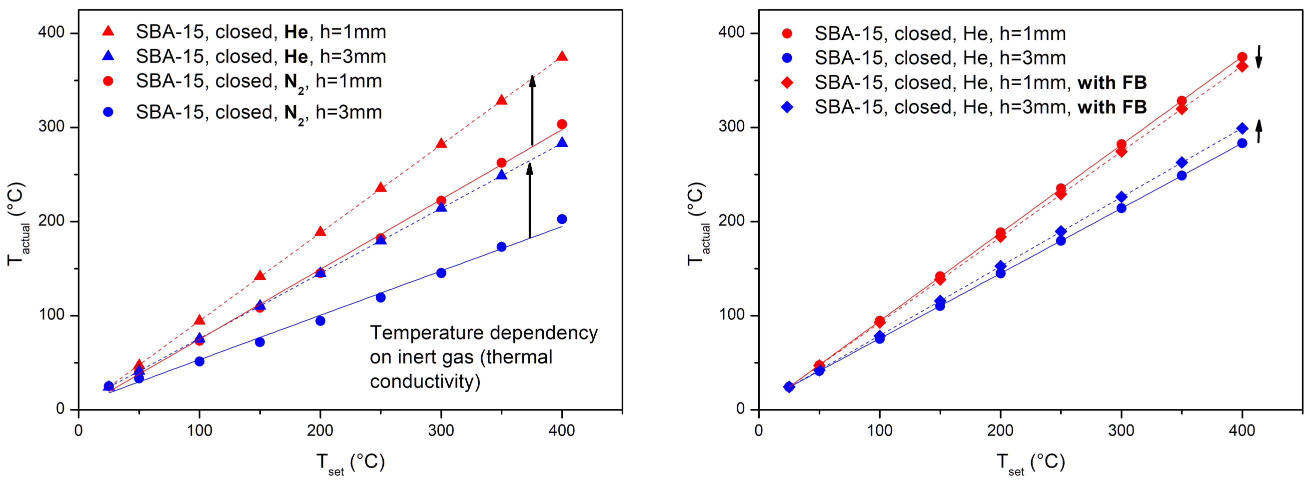

Figure 4.5: Correlation between the set temperature and the actual temperature in the Linkam cell. The effect of (left) inert gas and (right) fluidised bed mode was studied. Heights are specified as the distance to the bottom (non-woven).

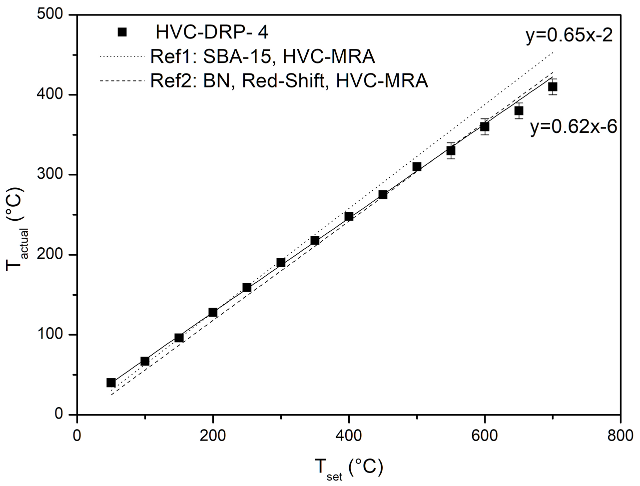

Figure 4.6: Correlation between the set temperature and the actual temperature in the Harrick cells. Temperatures were compared for the two different Harrick models. The measurements were performed in 1 mm depth from the surface. References Ref1 and Ref2 were taken from [100].

that, in principal, the temperature control shows high fluctuations. The HRV-DRP-4 model did not achieve the same performance as its “younger” model at high temperatures. The temperature deviation from the set temperature is even higher than for the Linkam cell. While for the latter, the surface temperature accounts for 373°C at a set temperature of 500°C, the Harrick cells show a surface temperature of 310°C (HVC-DRP-4) and 323°C (HVC-MRA). The effect of inert gas was not specifically studied. During the performed UV-vis measurements, the maximal temperature could not be reached while using Helium. Li et al. [80] mentioned that, in the presence of gases with high thermal conductivity, an increased convective heat transfer between the sample and the colder cell walls is assumed. In the case of the Harrick cell, more electrical current is needed to keep the bed (crucible + sample) at the desired temperature. The use of the Harrick cell for *in situ* and *operando* UV-vis and DRIFTs studies has been critically discussed in the literature.[108, 109] Especially, the prevailing temperature gradient has been mentioned. Ideally, an *operando* spectroscopic measurement should be performed in a conventional reactor. However, usually a compromise must be found in order to allow the radiation to probe the catalyst.[109] The term “*operando*” in the strict sense may refer to a spectroscopic information which is directly related to a catalytic activity. Common *in situ* cells are usually not appropriate for kinetic studies. In 2005, Bañares [27] emphasised that the catalytic data obtained with the spectroscopic cell should be in agreement with data achieved with a conventional catalytic reactor. Bañares and Khatib [110] presented a Raman cell which was a fixed-bed custom-built reactor made with optical quality quartz walls [106]. The *operando* Raman study is one of the few examples where the activity of the catalyst over the Raman cell was comparable to data measured with a conventional plug flow reactor.

In conclusion, due to the respective temperature profiles of the cells, the activity data obtained with the Linkam and the Harrick cell may not be directly comparable. In order to generate comparable spectroscopic data, the actual surface temperature is considered instead. The measured catalytic performance is referred to the hotter bottom temperature, and thus may not be the actual activity of the catalyst during the spectroscopic measurement. Table 4.2 provides an overview of the applied temperature corrections in this work. The use of the Linkam cell in combination with the fluidised bed mode, however, is promising for the *operando* approach. Particles, which are spectroscopically sampled, move constantly between the hotter bottom and the cooler surface. Moreover, the input of heat due to laser irradiation is inhibited for Raman spectroscopy. In the following, the Linkam cell will be tested in propane ODH for a silica supported vanadium oxide catalyst.

Table 4.2: Overview of the used temperature correlations in this work. FB is short for Fluidised Bed.

Cell	Name	Application	Equation	Reference
Linkam	Bottom or reaction temperature	Catalytic activity, FB	$T_{bottom} = 0.91 \cdot T_{set} + 1.75°C$	this work
Linkam	Surface temperature	Raman, FB	$T_{surface} = 0.73 \cdot T_{set} + 5.56°C$	this work
HVC-MRA	Surface temperature	UV-vis	$T_{surface} = 0.65 \cdot T_{set} - 2°C$	[100]
HVC-DRP-4	Surface temperature	DRIFT	$T_{surface} = 0.58 \cdot T_{set} + 13.70°C$	this work

4.3 Gas phase analysis

For the gas phase analysis, two acquisition devices are available, a Fourier-Transform Infrared spectrometer and a gas chromatograph. FTIR gas phase analysis is based on obtaining an infrared spectrum of the gas phase. The spectrum represents a fingerprint of each IR-active molecule, and thus requires the spectral separation of the corresponding bands. Peak heights or areas may be used for a quantitative analysis. Although the method shows high sensitivity, there are both minimum and maximum detection limits that depend on the IR-activity of the corresponding molecule. The data is recorded within minutes, which allows time-resolved monitoring of the gas phase. Despite these advantages, gas chromatography is the standard method in catalysis. The separation of the components of a gas mixture is based on the interaction of the mobile phase with the stationary phase of a column. The motion through the column is inhibited by the respective adsorption of the analyte molecule within the phase. As the mobile phase progresses along the column, the respective components reach the column end at different times, which is called retention time. The advantage of this technique is the reliable separation and quantification of the components of a mixture. However, the data generation usually takes about 30 min, which does not allow for continuous gas monitoring within a short time scale.

The following subsections evaluate the application of FTIR spectroscopy and gas chromatography in the ODH of ethanol and propane.

4.3.1 Fourier-Transform Infrared spectroscopy

For the ODH with ethanol, gas analytics had previously been implemented by Dr. Waleska.[100] In this thesis, spectra were similarly recorded on the Vertex70 spectrometer (Bruker) equipped with the RT-DLaTGS detector and a gas cell (Hellma Axiom Incopration). Corresponding calibration data was graciously provided. In order to improve the measurement speed, the spectral resolution was set from 1 to 4 cm^{-1}. Consequently, spectra were taken every 43 s without any significant reduction in quality. To apply this method to further ODH reactions, several requirements have to be met:

- ODH with CO_2: Quantification of the conversion of CO_2
- Propane ODH: Detection, identification, separation and quantification of products

Carbon dioxide shows several IR-active bands. At relevant concentrations, the band around 2300 cm^{-1} is saturated and cannot be integrated properly. The spectral analysis would require the dilution of the final gas mixture or the quantification of further bands, e.g. in the high wavenumber region. However, the by-product water shows overlapping spectral features at around 3500 to 4000 cm^{-1}, which also would not allow for a reliable detection (see figure 4.7).

For propane ODH, an appropriate product detection and separation has to be guaranteed. The test reaction was performed with a flow of 3ml$_n$/min C_3H_8, 3 ml$_n$/min O_2 and 29 ml$_n$/min N_2 for a silica supported vanadium oxide catalyst at a set temperature of 650°C in the Linkam cell. Several IR bands were identified, which are shown with their corresponding reference spectra in figure 4.8. A reliable product separation could not be obtained due to overlapping peaks.

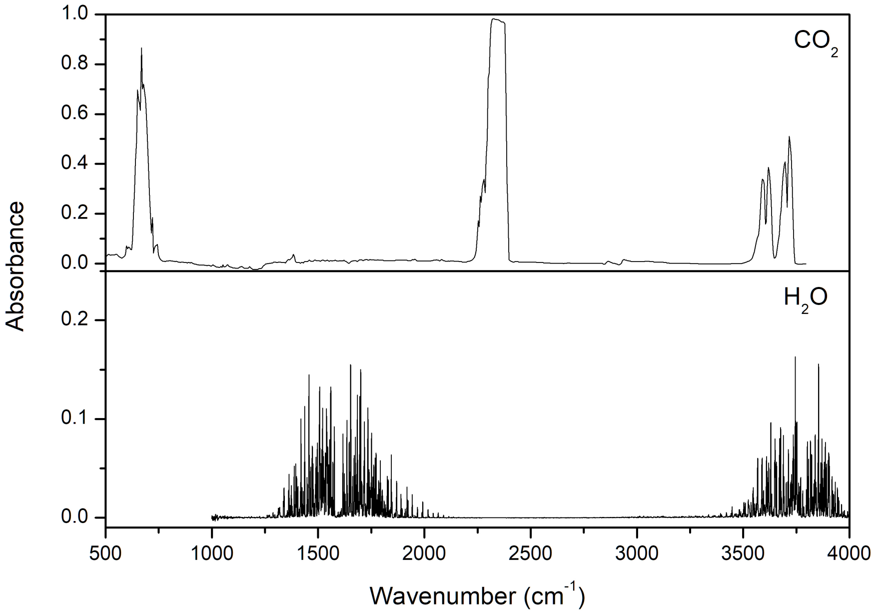

Figure 4.7: FTIR spectra of carbon dioxide and water. The water spectrum was graciously provided by Dr. Waleska.

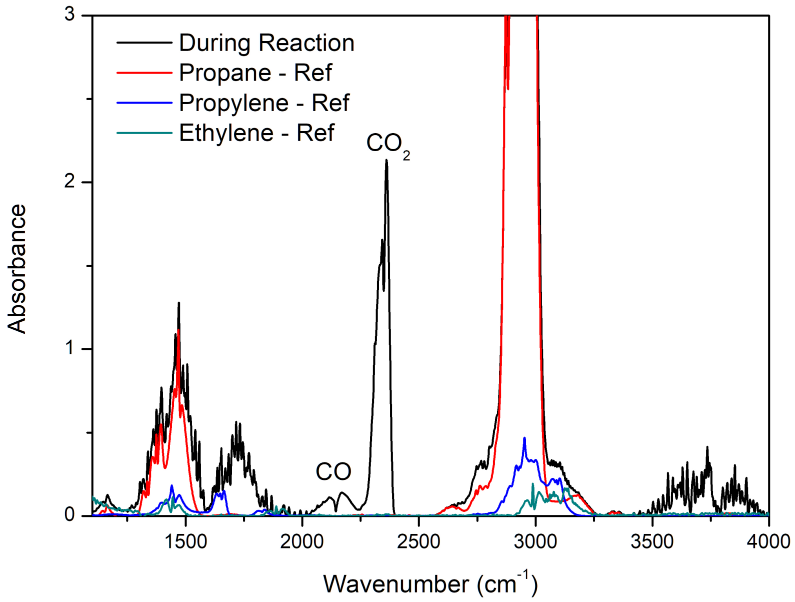

Figure 4.8: FTIR spectrum during reaction conditions with 0.6 VO_x/SBA-15 at a set temperature of 650°C (without fluidised bed operation) and corresponding reference spectra. The ethylene reference was graciously provided by Dr. Waleska.

4.3.2 Gas chromatography

Measuring device

In this thesis, an Agilent 7890B Series gas chromatograph was installed. An overview of the device and the data processing procedure is given in figure 4.9.

The outlet gas stream from the reactor continuously flows through a 6-port valve with a 0.25 ml loop, which is heated to 170°C. The measurement is initiated with the injection of the gas sample via the rotation of the valve. Inside the oven, two columns are connected in series, a HP-Plot Q (porous layer open tubular column, 30m x 0.535 mm x 40 μm) and a CP-Molsieve 5A (25 m x 0.53 mm x 50 μm). An intermediate 6-port valve enables column isolation. While the HP-Plot Q is suitable for the separation of hydrocarbons and alcohols, the molecular sieve is used for the separation of the permanent gases. Helium (Westfalen, 5.0) is chosen as the carrier gas. For subsequent detection, a thermal conductivity (TCD) and a flame ionization detector (FID) are connected in series. The TCD senses changes in the thermal conductivity, and compares it to a reference flow of the carrier gas. The FID is based on the detection of ions formed during the combustion of organic compounds in a hydrogen flame. For the operation of the FID, H_2 (Westfalen) with a purity of 5.0, and in-house air is used. Its purity was determined to be 0.25 ± 0.02 Vol.% of water and 0.0541 ± 0.0002 Vol.% of CO_2 via the FTIR gas phase spectrometer after purging for 5 h. No hydrocarbons were detected. The GC is controlled via a computer, which operates with the OpenLAB CDS ChemStation Edition Workstation Software. Measurements can be performed online with subsequent sample injections (Sequence mode). A pressure transducer records the absolute pressure. Especially, due to

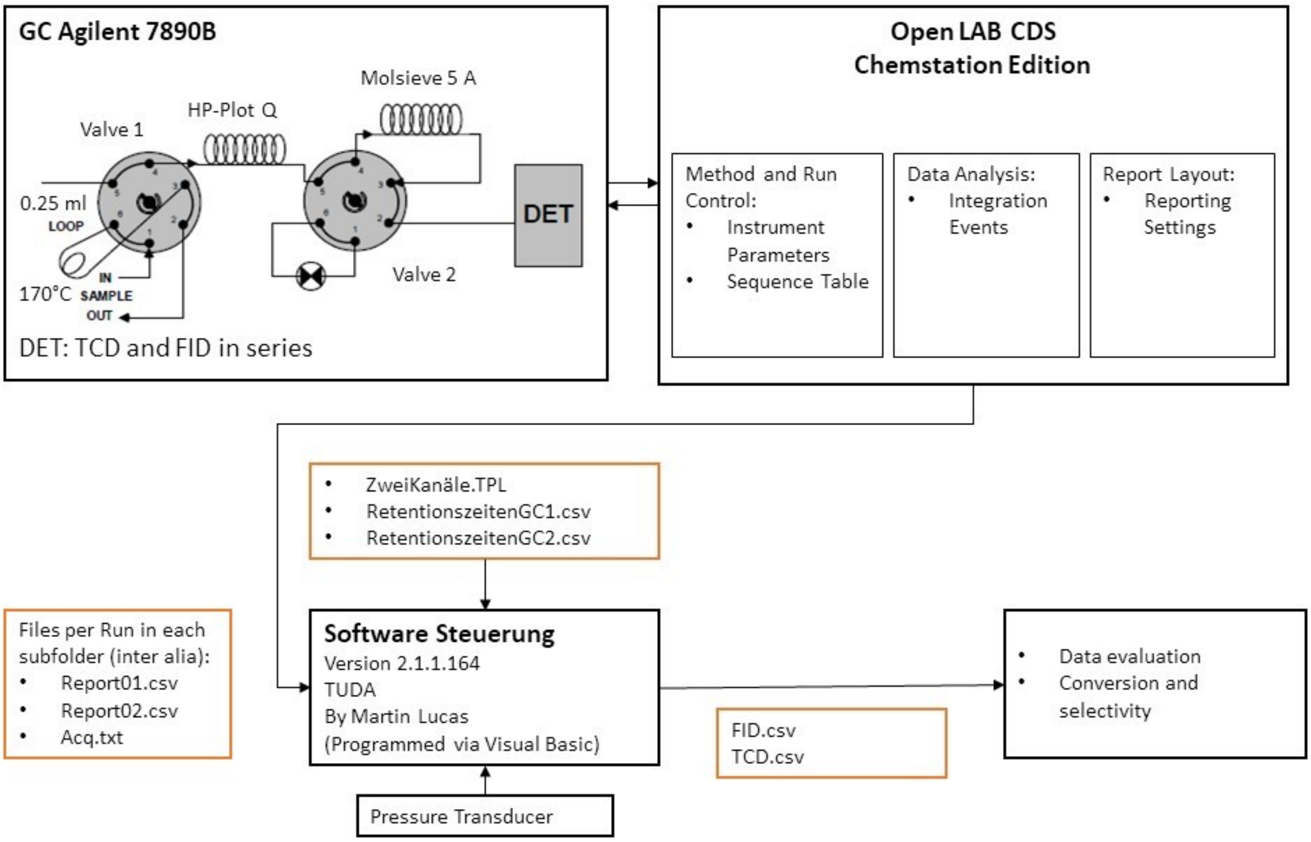

Figure 4.9: Scheme of the Agilent 7890B Series GC and the data processing procedure

the daily variation of the atmospheric pressure, the amount of substance present in the loop changes according to the ideal gas law. Data is automatically analysed by set integration events. Two reports are created for each run, which can be loaded and read out by the software "Steuerung", which was graciously provided and adapted by Martin Lucas (Rose Research group, TU Darmstadt). Two files are created, which include the peak area for all components.

Sample injection

The injection of the gas sample is performed by the gas sampling valve, which is moved by a pneumatic actuator. Hence, the event includes a short interruption to the ongoing flow. As a result, the powdery sample in the reactor may be pushed out of the sample holder. As a worst case scenario, the powder may stick to the reactor window, which would not allow any spectroscopic measurements. This effect can be explained by a change in flow velocity and static pressure, resulting in a short-time pressure shock wave in the tube. Without the splitting of the gas flow as shown in figure 4.1, the pressure wave is directly transmitted to the reactor. A needle valve allows to adjust the flow rates. A flow of 3 to 5 ml/min is recommended for the GC branch.

Data acquisition

For peak separation, a suitable temperature programme (figure 4.10) has been developed while performing a reaction at a set temperature of 650°C (0.6 VO_x/SBA-15, without FB). The ramp rate, final temperature, and the flow rate were adjusted, allowing an adequate peak separation combined with a shortening of the time for late-eluting analytes. The final temperature programme is shown together with the FID and TCD chromatogram for the acquired calibration mixture at the bottom of figure 4.10. Details on its gas phase composition can be found in table 4.4 and 4.5 (paragraph Calibration). Permanent gases and methane pass the HP-Plot Q in less than 2.5 min, which in the following will be separated in the Molsieve 5A. Valve 2 is turned on and the molecules eluted from the HP-Plot Q are detected via TCD and FID. The off position of the valves correspond to their position as illustrated in figure 4.9. The final temperature is set to 180°C with a ramp rate of 10°C per min. Propane and Propene elute after 7.5 min. At high reaction temperatures, several unidentified analytes were detected with higher retention times. Possible by-products could be acetone or acetic acid. Moreover, propylene may further react to acrolein, acrylic acid, acolein dimer and propionaldehyde. After cooling down to 120°C, valve 2 is turned off. Oxygen, methane and CO appear in the chromatogram. Propane and propene show a tailing peak due to column overload. The signals of valve switching is at 2.6 and 18 min.

During DH in CO_2 assistance, H_2 may be produced. In principle, the detection is possible via the TCD detector, however, its sensitivity is carrier gas dependent. The thermal conductivity of H_2 is in the order of He, which would require the use of N_2 or Ar as a reference gas, which, in turn, limits the sensitivity towards CO. Moreover, the TCD response may not be linear with H_2 concentration. To optimize the detection with He as the carrier gas [111], the TCD detector temperature can be varied. In this work, the TCD temperature had been set to 200°C. With 7.5% of H_2 in Ar, a negative peak at 18.9 min could be detected.

Data processing

The automatic data processing is provided by the "Data Analysis" section of the "Open LAB CDS Chemstation Edition" Software. The start and end time is recognised for each peak, and marked with a vertical line, which corresponds to the respective retention time. Afterwards, the apex of each peak is defined, the baseline is allocated, and the peak area measurement is performed. In the advanced baseline tracking mode, the integrator tries to optimize the start and end locations of the peaks. Hence, the baseline is re-established for a cluster of peaks, and baseline penetrations are removed.[112] The initial integration events are summarised in table 4.3. The most important parameters are the slope sensitivity and the peak width, which define the peak sensitivity and set an initial sampling interval for the integrator to distinguish peaks from baseline noise.[112] "Area Reject" allows the rejection of peaks. A low slope sensitivity and negative peak recognition was activated for H_2 detection at around 18.9 min.

Calibration

A multiple point external calibration of propane, propylene, CO_2, and ethylene was executed proving the linear response in the respective concentration range. However, in the case of propylene and CO_2, calibration could not be done at the relevant amounts. The calibration curves coverd a concentration range which was higher than the measured amount of propylene and CO_2 during reaction conditions. This is due to the fact that a minimum flow of 3 ml_n/min can be set for both gases, and further dilution with an inert gas was not possible. The knowledge of relative response factors from the literature was subsequently exploited to determine ethane, methane, and CO concentrations. The propane ODH reaction

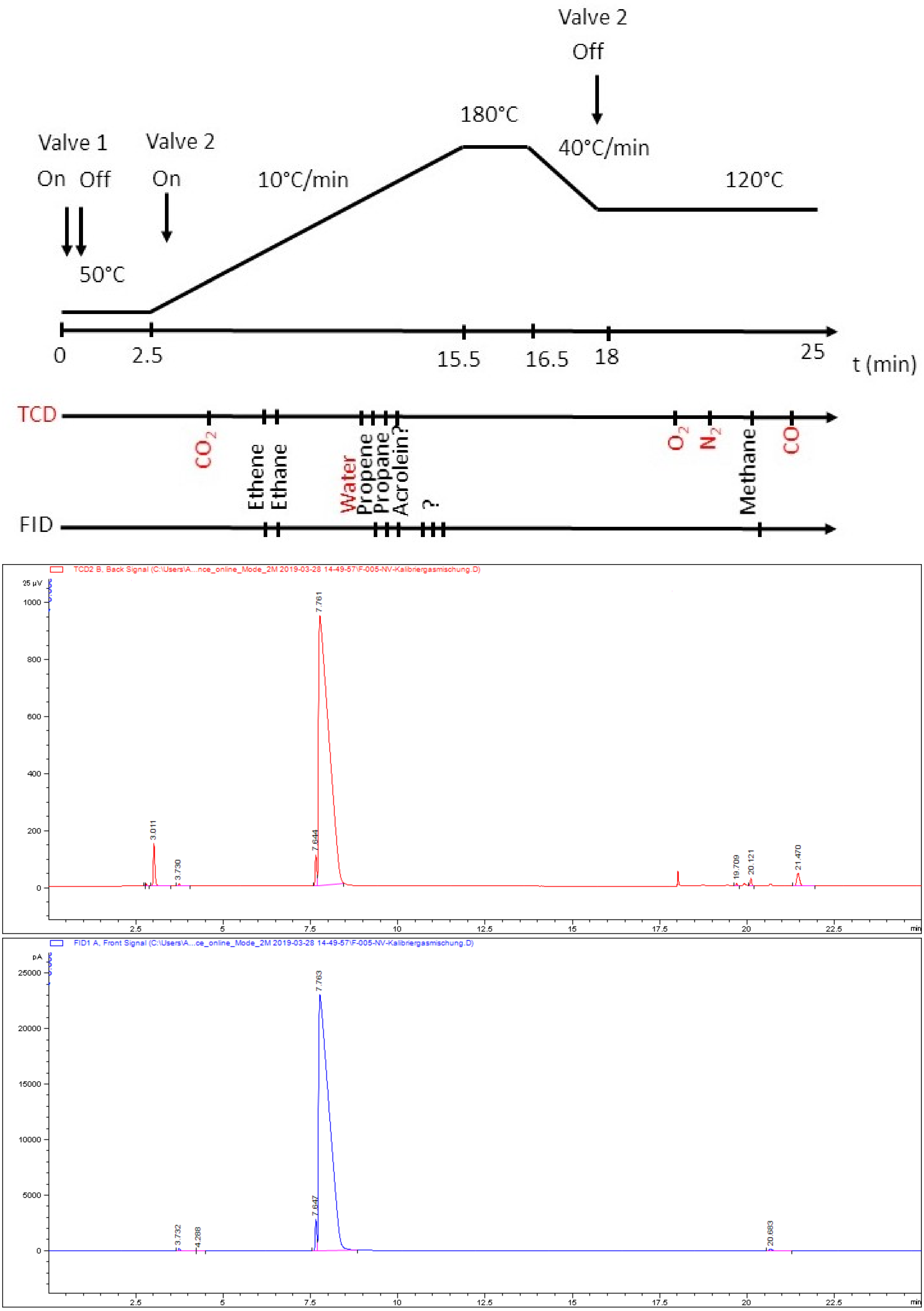

Figure 4.10: Developed temperature programme for propane ODH (top), and TCD and FID chromatograms of the acquired calibration mixture (bottom). Details on its gas phase composition can be found in table 4.4 and 4.5.

Table 4.3: Integration Events

Initial Events for all Signals	
Tangent Skim Mode	New Exponential
Tail Peak Sim Height Ratio	5.00
Front Peak Skim Height Ratio	5.00
Skim Valley Ratio	20.00
Baseline Correction	Advanced
Peak to Valley Ratio	500.00
Slope Sensitivity	150.000
Peak Width	0.040
Area Reject	1.000
Height Reject	1.000
Shoulders	Off
Area Percent Reject	0.000

was tested with a 0.6 VO_x/SBA-15 catalyst at a reaction temperature of 502°C in a fluidised bed mode. Furthermore, data from propane ODH experiments with CeO_2, and with CO_2 were obtained. On that basis, a calibration mixture (Air Liquide) was acquired, which represents a propane conversion of 3.75% with an initial propane concentration of 12.5 Vol.%, and a propylene selectivity of approximately 50%. The amount of produced CH_4 was taken from CO_2 ODH with CeO_2. Table 4.4 and 4.5 summarise the response factors of the calibration mixture for the FID and the TCD, respectively. The concentrations specify the actual gas composition, and thus slightly differ from their target values. The average peak area was determined from ten subsequent measurements. H_2 was calibrated with a mixture of 7.5% H_2 in Ar. The Response Factor RF was defined as the peak area A divided by sample amount n at 1 bar. Concentrations were calculated to molar amounts via the ideal gas law. Hence, the respective amount of substance n was obtained via the calibrated Response Factor and the measured peak area, while considering the recorded pressure p at the time of sample injection according to

$$n = \frac{1bar}{p}\frac{A}{RF} \tag{4.1}$$

Finally, the calculated amount of propane from the mixing via the MFCs was compared to the “actual” measured amount of propane via the GC. Various concentrations between 8% and 14% of propane mixed in He were set and each concentration was measured for two times via the GC. The Linkam cell was replaced for a tube in this experiment. The procedure is similar to an external multi-point calibration. It is noted that for a maximum total flow of 50 ml/min, as recommended for the Linkam cell, the propane MFC has to operate at its limit, i.e. C_3H_8 flows had to be set to 3.2 to 5.6 ml_n/min. Higher concentrations would result in inadequate peak separation of propane and propylene for activity measurements. On the one hand, the amount of propane was determined via the respective flows of propane and He. The errors were calculated by considering the specified accuracy of the MFCs and the error propagation. On the other hand, the amount of propane was determined via the measured value of the GC. The accuracy of the amount of propane in the calibration mixture itself accounts for a percentage deviation of 2.0%. Hence, its error is propagated to the Response Factor. Thus,

Table 4.4: Response Factors for substances measured via the FID for a calibration mixture (Air Liquide). The actual concentrations and their deviations were specified by the manufacturer.

	Ethene	Ethane	Propene	Propane	Methane
Concentration (Vol. %)	0.01861	0.00099	0.2489	11.61	0.04053
Deviation (Vol. %)	0.00037	0.00002	0.005	0.23	0.00081
Percentage Deviation (%)	2.0	2.0	2.0	2.0	2.0
Amount ($*10^{-9}$mol)	1.26	0.07	16.89	787.79	2.75
Average Peak Area	512.9	27.12	8865	465 807	585.0
Deviation	0.7	0.03	18	611	0.3
Percentage Deviation (%)	0.14	0.12	0.20	0.13	0.05
Response Factor ($*10^{10}$ 1/mol)	40.6	40.4	52	59	21.3
Deviation ($*10^{10}$ 1/mol)	0.8	0.8	1	1	0.4
Percentage Deviation (%)	2.0	2.0	2.0	2.0	2.0

Table 4.5: Response Factors for substances measured via the TCD for a calibration mixture (Air Liquide). The actual concentrations and their deviations were specified by the manufacturer.

	CO_2	H_2	CO
Concentration (Vol. %)	0.3777	7.5	0.2266
Deviation (Vol. %)	0.0076		0.0045
Percentage Deviation (%)	2.0		2.0
Amount ($*10^{-9}$mol)	25.63	509	15.38
Average Peak Area	473	143	254.7
Deviation	13	2	0.4
Percentage Deviation (%)	2.84	1.6	0.15
Response Factor ($*10^{10}$ 1/mol)	1.85	0.028	1.66
Deviation ($*10^{10}$ 1/mol)	0.06		0.03
Percentage Deviation (%)	3.5		2.0

measured amounts of propane have an accuracy of 2.0% itself. As shown in figure 4.11, the error intervals overlap at propane amounts higher than 6.5x10^{-7} mol. As the actual propane amounts remain unknown, the GC measured values were entered for the x-axis. The maximal deviation between the determined amount measured via the GC and the mixed amount via the MFC corresponds to 2.8%. These considerations are therefore relevant, as the catalytic and *operando* experiments do not include the inlet concentration measurement of C_3H_8 via e.g. a bypass. The carbon balance is therefore especially dependent on the knowledge of the assumed amount of propane obtained via the mixing. Carrero et al. [10] mentioned the importance of the carbon balance for kinetic studies. In this work, a CB within less than 2% may be sufficiently accurate. In contrast to values reported in the literature, the CB is calculated via the expected amount of propane, which is dosed via the MFCs (see equation 3.7). The determination is within the range of the possibilities provided by the current setup.

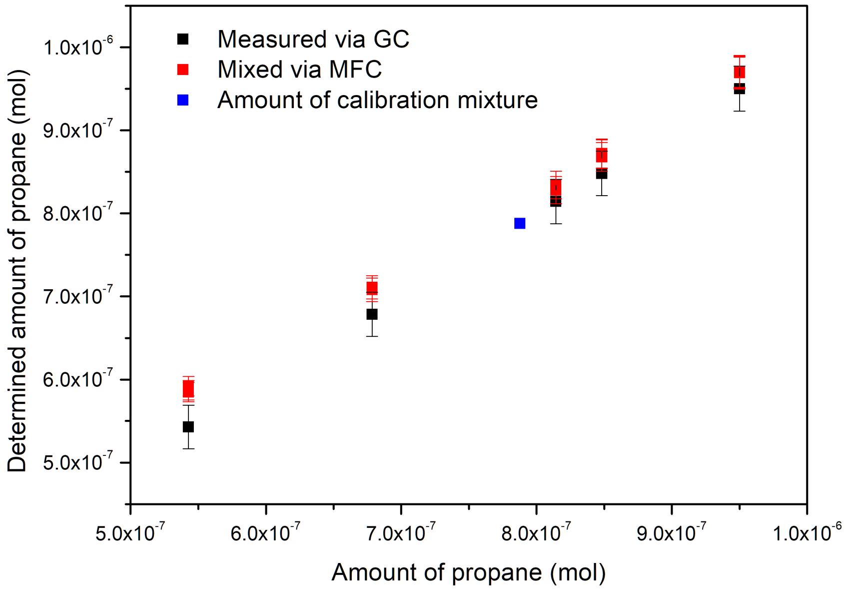

Figure 4.11: Comparison of measured propane amounts via the GC and determined propane amounts mixed via the MFCs. The values on the x-axis correspond to the GC measured values.

5 *Operando* catalysis with silica supported vanadium oxide for propane ODH

The oxidative dehydrogenation of propane was chosen as a test reaction in order to evaluate the installed *operando* Raman GC setup. Silica supported vanadium oxide catalysts have already been intensively studied for the ODH with propane. Besides its catalytic performance [10, 36], DFT calculations are available [39, 40]. As a result, several reaction mechanisms have been proposed.

The objective of this chapter is to establish a reaction mechanism for the oxidative dehydrogenation of propane with a silica supported vanadium oxide catalyst. Its outcome is based on the spectroscopic data obtained under *operando* conditions. Thereby, the interpretation of the spectroscopic information [113] is a crucial step towards the understanding of the vanadium oxide structure and its behaviour under reaction conditions.

First, the catalytic activity of the catalyst is studied at various temperatures. The results are compared to published data, obtained in a conventional reactor. Catalytically realistic conditions are chosen for the subsequent *operando* study. Secondly, *operando* Raman, UV-vis, and DRIFT spectra are presented and discussed. UV-vis spectroscopy provides the absorption behaviour of the catalyst on the basis of electronic transitions. Employing different laser wavelengths for Raman spectroscopy, the resonance effect is exploited in a targeted manner. DRIFT spectroscopy provides complementary information on possible surface species and adsorbates. The spectroscopic characterisation of the VO_x/SBA-15 catalyst has already been extensively discussed by Nitsche and Hess [105, 114], and Waleska et al. [30, 115], and is herein introduced in the context of the obtained *in situ* data. Complementary experiments were conducted in order to obtain a better understanding of the *operando* spectra. These include experiments, such as *operando* conditions at lower temperature, and an interference experiment. Moreover, the temperature effect on the vanadium oxide structure and on gas phase propane is presented. *In situ* DRIFT spectra are shown at various temperatures under reactive conditions. Recently, Shee and Deo [116] gave direct evidence of alkoxide formation during alkane adsorption on a vanadium oxide supported titania-doped catalyst by using *in situ* DRIFT spectroscopy. To study the redox properties of the silica supported vanadium oxide catalyst, hydrogen and propane reduction experiments were performed. The *in situ* experiments are comparably designed to a temperature-programmed reduction (TPR) Raman experiment, but without the detection of the outcoming gas phase. Previously, Wu et al. reported a similar approach, in order to study the redox behaviour of VO_x/silica.[117] Finally, the data is discussed in the context of the degree of reduction and the dependency on the substrate. Recently, Waleska et al. [30] have demonstrated the potential of *operando* multiwavelength Raman spectroscopy in the ODH with ethanol.

5.1 Activity study

Figure 5.1 shows the catalytic performance of the 0.6 VO_x/SBA-15 (14-15 mg, particle sizes: 200-300 μm, loading: 3.38 wt% VO_x) catalyst in comparison to SBA-15 and the empty cell (gas composition: 12.5% C_3H_8 / 12.5% O_2 / 75% He, total flow: 40 ml_n/min). The reaction was performed in a fluidised bed mode. In a second experiment, the gas composition consisted of 14% C_3H_8 /12% O_2 /74% He with a total flow of 36 ml_n/min. The CB was determined to be <1% and <3.5%, respectively.

Propane conversion is detected at temperatures >300°C and rises with increasing temperature. SBA-15 does not show any significant activity in comparison to values obtained for the empty cell. The increase of the residence time, achieved

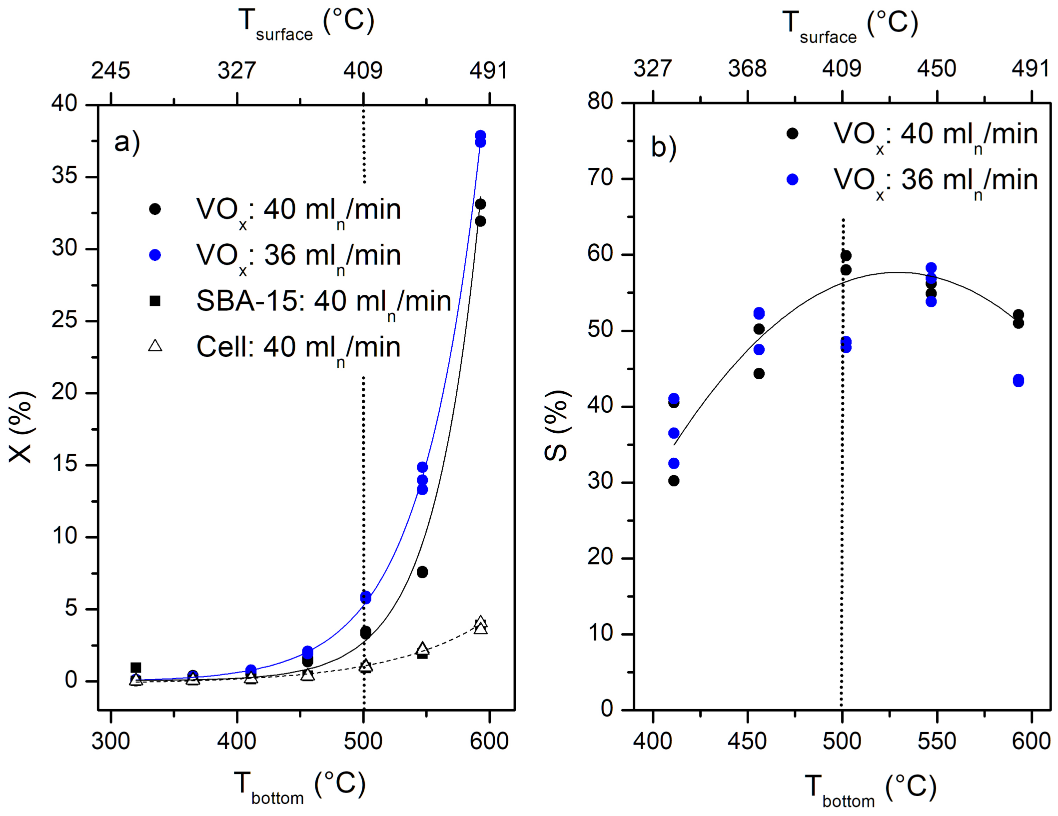

Figure 5.1: Catalytic performance of the 0.6 VO_x/SBA-15 catalyst in comparison to SBA-15 and the empty cell. a) Propane conversion as a function of temperature. Two different total flow rates are depicted. b) Selectivity towards propene as a function of temperature. The dashed lines indicate the temperature chosen for the *operando* experiments. The reaction was performed in a fluidised bed mode. Lines are to guide the eye.

via the lowering of the total flow (or rather GHSV), results in a higher conversion. The selectivity shows a maximum at around 500°C. It has been proposed that CO_2 and CO are mainly produced via the overoxidation of propylene [10, 36], which appears to be contrary to the obtained data. Reported selectivity-conversion dependencies [36, 44] show that with increasing conversion, propene selectivity drops. For these measurements, the GHSV was varied while the temperature was maintained. So far, such experiments have not be performed in the Linkam cell. Though, the propene selectivity of the cell was determined to be around 20 to 30%, independent of conversion. Hence, significant amounts of detected CO_2 molecules are attributed to the Linkam cell, and consequently not to the catalyst. Moreover, peak separation of propane and propylene is not completely guaranteed at low conversions. The temperature programme had been developed for a significantly higher amount of converted propane molecules (reaction temperature 609°C, without FB). The conversion-selectivity dependency was therefore studied in a subsequent experiment with a lower propane concentration. The reaction was executed with a gas composition consisting of 8.3% C_3H_8 / 8.3% O_2/ 83.3% He at a total flow of 36 ml_n/min. For comparison, bare SBA-15 was taken. The selectivity towards propylene, CO_2, and CO is illustrated in the left panel of figure 5.2. For each temperature, two GC runs were measured. In order to consider the amount of products produced by the cell (SBA-15), the average value was calculated for each product and each temperature. Finally, corrected selectivity values were obtained by the respective subtraction of these values. Although the method may contain errors, the expected propene selectivity trend becomes apparent (see right panel of figure 5.2). The conversion and selectivity of the previous results were therefore only corrected for a reaction temperature of 502°C via the respective SBA-15 values (2). Additionally, the corrected conversion was determined via the direct subtraction of the average SBA-15 conversion (1). The results are presented in table 5.1.

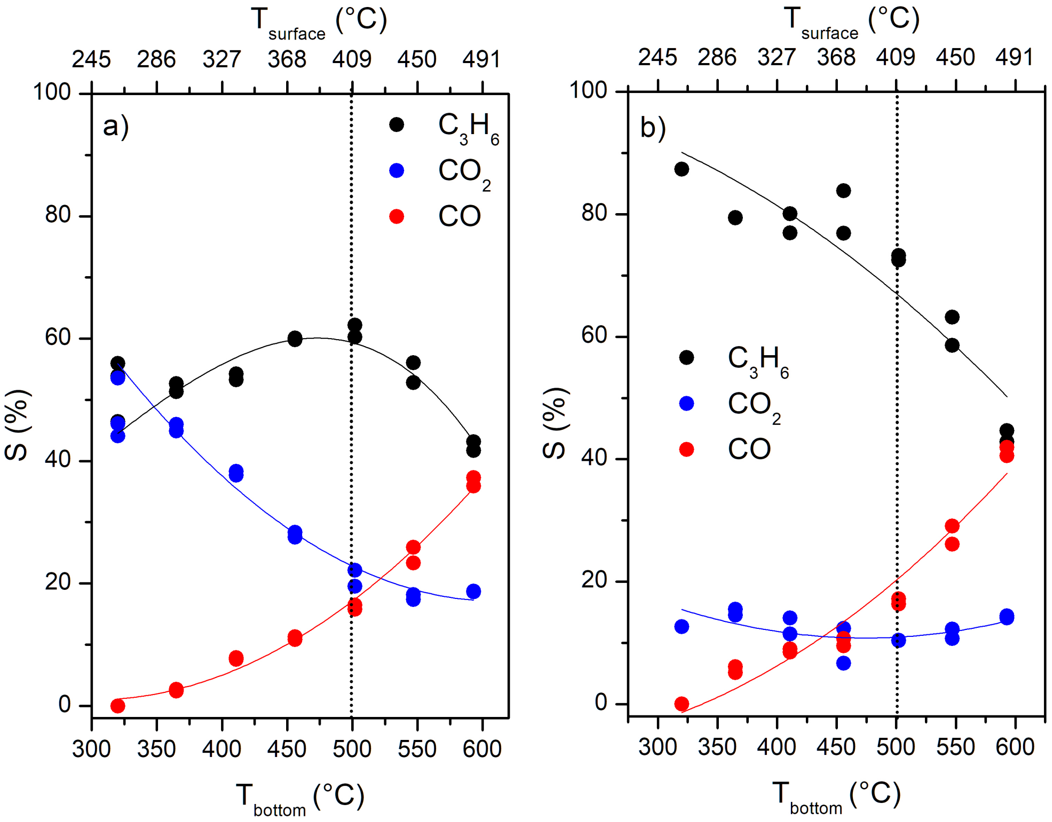

Figure 5.2: Selectivity towards propene of the 0.6 VO_x/SBA-15 catalyst as a function of temperature with a feed consisting of 8.3% C_3H_8 / 8.3% O_2/ 83.3% He at a total flow of 36 ml_n/min. a) Data as measured. b) Selectivity values obtained after subtracting corresponding activity data of bare SBA-15. Lines are to guide the eye.

Table 5.1: Comparison of catalytic data at a reaction temperature of 502°C. VO_x(1) is obtained by subtracting the average of the conversion of SBA-15. VO_x(2) values are calculated by subtracting the average amount of products obtained with SBA-15.

	0.6 VO_x/SBA-15, 40 ml_n/min		0.6 VO_x/SBA-15, 36 ml_n/min		Reference [36]	
	X(%)	S(%)	X(%)	S(%)	X(%)	S(%)
VO_x/SBA-15	3.37 ± 0.08	58.9 ± 0.9	8.04± 0.17	61 ± 1		
- SBA-15 (≈ Cell)	0.94 ± 0.02	21.5 ± 0.2	2.33 ± 0.18	27.3 ± 0.5		
= VO_x (1)	2.43 ± 0.10		5.71 ± 0.35			
= VO_x (2)	2.43 ± 0.08	73.2 ± 1.8	5.9 ± 0.2	72.9 ± 0.4	2.3 ± 0.1	78 ± 2
TOF (· 10^{-3} 1/s)	≈ 6.6		≈ 16			

A great number of publications is available, reporting propane ODH kinetics over silica supported vanadium oxide catalysts.[36, 44, 47, 118–122] In 2014, Carrero et al. [10] provided an overview of obtained TOF values, mentioning activation energy, temperature, BET, loading, vanadium density, and the synthesis method. Reported temperatures range from 400 to 600°C. Primarily, vanadium densities below monolayer coverage were considered, and the determined TOF values ranged from $0.01 \cdot 10^{-3}$ to $2 \cdot 10^{-3}$ 1/s for 400°C and from $0.1 \cdot 10^{-3}$ to $40 \cdot 10^{-3}$ 1/s for 500°C. The TOF values, reported here, fit well into the reported range.

Dinse et al. [36] used a VO_x/SBA-15 catalyst with a loading of 2.7 wt.% for a kinetic study. Experiments were run in a u-shaped fix-bed quartz reactor. The feed composition was specified as $C_3H_8/O_2/N_2$=16.9/16.9/67.5, and the GHSV varied between 600 and 6600 1/h by portioning 200 to 600 mg of the sample. At a temperature of 500°C, a conversion of 2.3 ± 0.1 % with a selectivity of 78 ± 2 % was obtained. The result is related to the shortest residence time. Inaccuracy values refer to the reading inaccuracy from the plot. A similar conversion and selectivity was determined in this work. In the literature, their experiments provide the best comparability, and also confirms the temperature correction (see chapter 4.2.2) to be valid. The temperature at the surface, where the spectroscopic measurement is supposed to take place, is determined to be 409°C for a reaction temperature of 502°C. The conversion at a bottom temperature of, e.g., 411°C corresponds to 0.59 ± 0.08% and 0.73 ± 0.07% at a total flow of 40 and 36 ml_n/min, respectively. Due to the implemented fluidised bed method, the powdery sample constantly moves in the sample bed. It is proposed that the particles mainly participate in the reaction during their flow through the hotter bottom, and are spectroscopically characterised while flowing to the top. In principal, this qualifies the Linkam reactor in combination with the fluidised bed method for the *operando* approach.

5.2 *Operando* results under reaction conditions

Operando UV-vis spectroscopy

UV-vis spectra were recorded at a sample temperature of 408°C under oxidative conditions (12.5% O_2/ 87.5% N_2, total flow: 40 ml_n/min) and *operando* conditions (12.5% C_3H_8 / 12.5% O_2/ 75% N_2, total flow: 40 ml_n/min) for the 0.6 VO_x/SBA-15 catalyst. The activity data is shown in table 5.2. The conversion was determined to be 14 ± 2% with a selectivity of 28 ± 5%. The comparability with the activity obtained in the Linkam cell is not given. On the one hand, a temperature of 630°C had to be set at the temperature controller in order to obtain a sample temperature of 408°C at the surface. Although the bottom temperature had not been explicitly measured, it is expected that the hottest sample temperature might be around 550 - 600°C. On the other hand, the Harrick cell is known for its high self-activity, probably towards CO_x in this case.[100] Corresponding spectra are depicted in figure 5.3.

Table 5.2: Summary of the catalytic performance of the 0.6 VO_x/SBA-15 during *operando* conditions in the UV-vis experiment (Harrick cell, model HVC-MRA).

	X (%)	S(%)	CB(%)
VO_x/SBA-15	14 ± 2	28 ± 5	<7

The UV-vis spectrum of the sample shows the typical absorption curve of a dehydrated VO_x species at low loading. Several contributions have already been identified. The range between 200 and 300 nm is attributed to tetrahedrally coordinated monomeric, dimeric, and trimeric VO_x units, and the range between 300 and 400 nm to tetrahedrally coordinated long-chain or large 2D VO_x oligomers (ligand to metal charge transfer transitions, LMCT).[30, 113] The absence of crystalline vanadium pentoxide is confirmed by its missing component in the vis region at around 481 nm.[123] The band edge energy is an indicator for the number of V-O-V bonds present.[105] Here, mainly a trimeric structure is assumed,

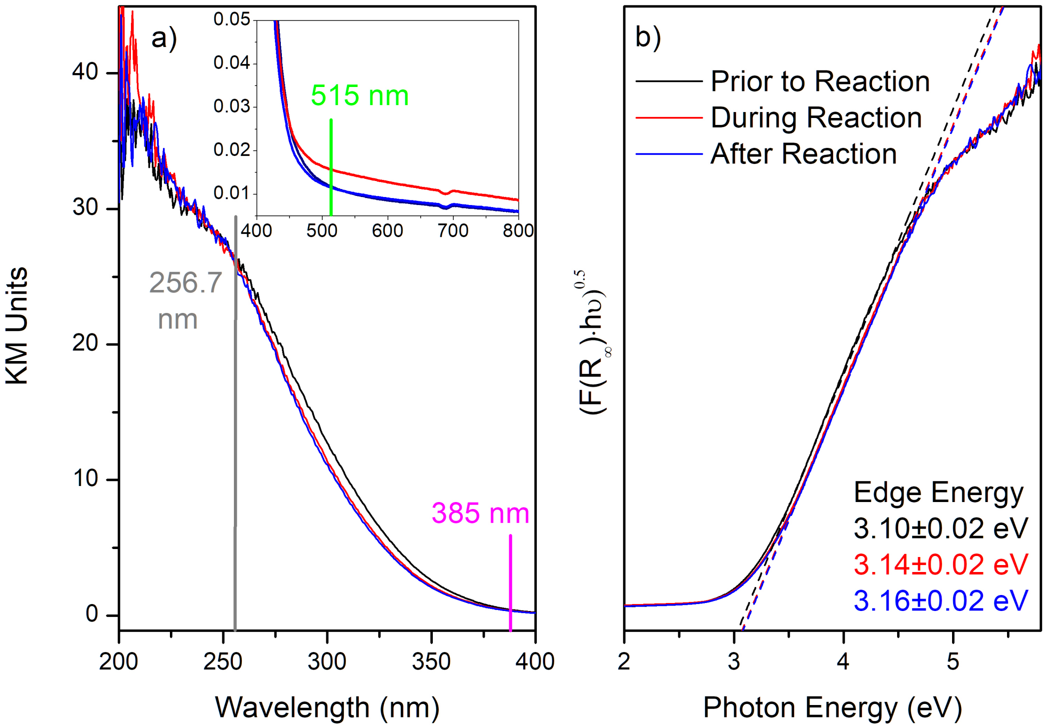

Figure 5.3: *Operando* UV-vis spectra of the 0.6 VO_x/SBA-15 catalyst prior to (black), during (red), and after (blue) propane ODH recorded at 408°C. The feed during *in situ* conditions consisted of 12.5% O_2 / 87.5% N_2; the feed during *operando* conditions consisted of 12.5% C_3H_8 / 12.5% O_2/ 75% N_2. The excitation wavelengths (256.7 nm, 385 nm, 515 nm) used for the Raman experiments are marked. The inset gives an enlarged view of the spectra at longer wavelengths.

as the band edge energy of 3.10 ± 0.02 eV corresponds to an average number of 2.1 V-O-V bridges. Under *operando* conditions, the band edge energy shifts to a higher value, resulting in a slight decrease of the average number of V-O-V bonds. At the same time, the absorption between 200 and 220 nm increases, where mainly monomeric VO_x structures are located.[113] In the vis region, d-d transitions are responsible for a rise in absorption, indicating the partial change of oxidation state from V(+5) to V(+4) or V(+3).[124, 125] After the reaction, the original state of the catalyst is not recovered under oxidative conditions, as the band edge energy exhibits an even increased shift to 3.16 eV, representing around 1.8 V-O-V bonds. This points to irreversible structural changes and a possible participation of V-O-V in the overall reaction mechanism. The decline in the vis region indicates the reoxidation of reduced vanadium oxide species from 3+/4+ to 5+.

Operando Multiwavelength Raman spectroscopy

The multiwavelength approach is based on the appropriate choice of excitation wavelengths. While 385 nm and 515 nm correspond to pre-resonance and non-resonance conditions, respectively, the excitation at 256.7 nm meets the requirement for full resonance enhancement.[30]

For the Raman experiments, the Linkam cell was used. 256.7, 385, and 515 nm spectra (figure 5.4) were obtained prior to and during reaction conditions (14% C_3H_8 / 12% O_2/ 74% He total flow: 36 ml_n/min) for the 0.6 VO_x/SBA-15 catalyst. The 515 nm spectra had to be taken from the interference experiment (reaction conditions: 12.5% C_3H_8 / 12.5% O_2/ 75% He total flow: 40 ml_n/min). Most probably, the focus position had changed during the *operando* experiment, and an appropriate background subtraction could not be performed. Likewise, the interference experiment includes spectra prior to and during reaction conditions. In contrast, subsequent to *operando* conditions, the oxygen was turned off (see section 5.3). Corresponding raw data of the 256.7, 385 and 515 nm spectra can be found in the annex (see figures S1.1, S1.2, S1.3, respectively). The catalytic activity is summarised in table 5.3. The data proves that *operando* spectra correspond to an active ("working") catalyst.

Table 5.3: Summary of the catalytic performance of the 0.6 VO_x/SBA-15 during *operando* conditions in the 256.7, 385, and 515 nm Raman experiment

Experiment	X (%)	S (%)	CB (%)
VO_x/SBA-15, 256.7 nm	4.6 ± 0.2	54.8 ± 0.2	<2
VO_x/SBA-15, 385 nm	4.9 ± 0.1	56 ± 1	<3
VO_x/SBA-15, 515 nm	6.3 ± 0.2	63.2 ± 0.7	<2
SBA-15, 256.7 nm	2.4 ± 0.1	11.4 ± 0.8	<4

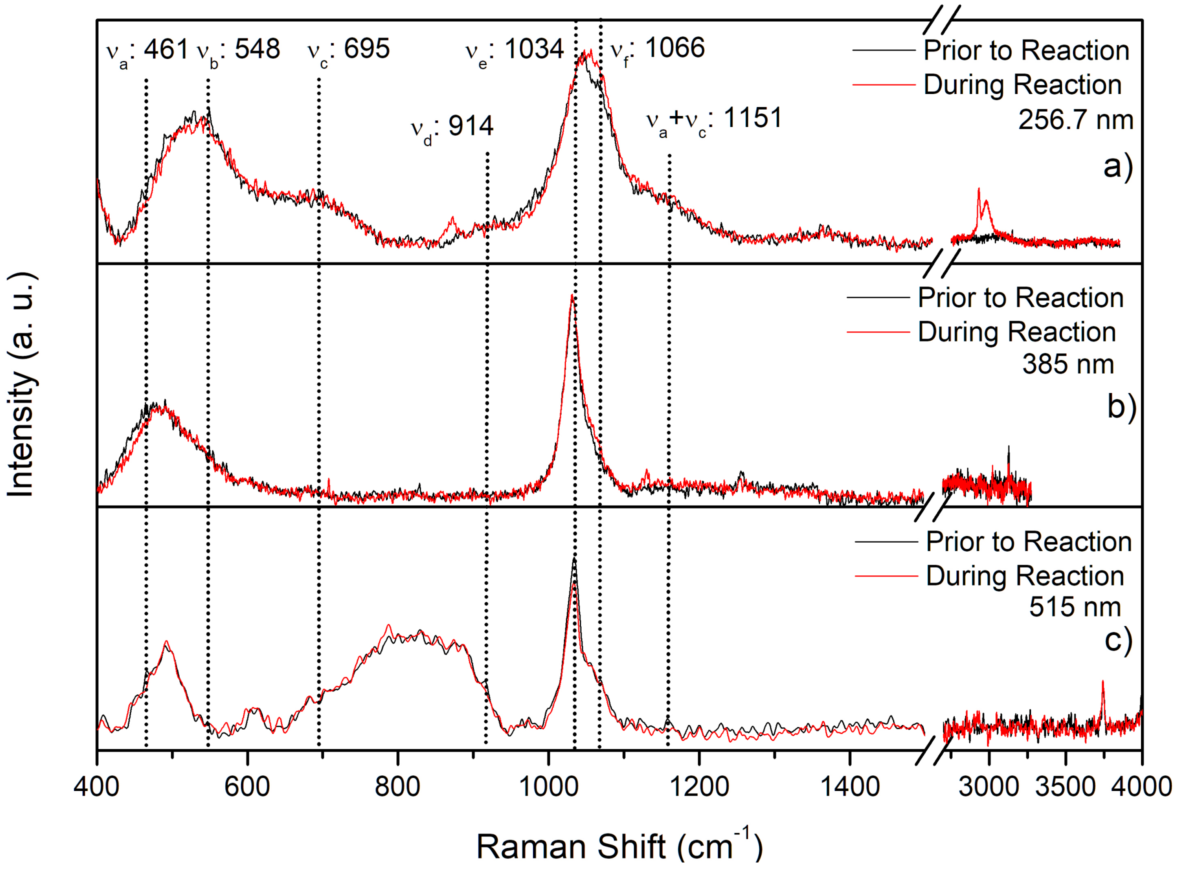

Figure 5.4: *Operando* multiwavelength Raman spectra of the 0.6 VO_x/SBA-15 catalyst prior to (black) and during (red) propane ODH recorded at 409°C. Spectra at 385 nm were normalised to V=O.

The spectrum of the catalyst prior to reaction conditions at 515 nm shows strong signals of the support. Raman bands at 492, 608, 818, 980, and 3743 cm^{-1} are assigned to D_1 and D_2 defect bands of silica, as well as to Si-O-Si, Si-OH and

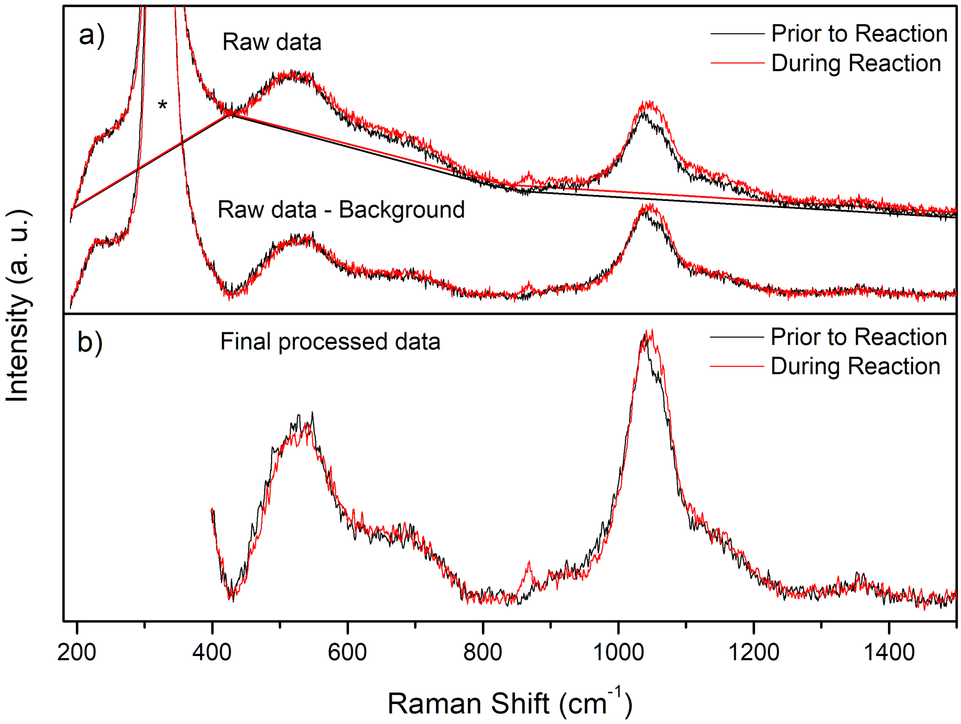

Figure 5.5: Data processing of the 256.7 nm Raman spectra prior to and during reaction.

SiO-H vibrations, respectively. At 256.7 nm, Raman signals, which correspond to supported vanadium oxide species, experience full resonance enhancement. The excitation wavelength is located in the absorption regime of low oligomeric, trimeric, and dimeric species. Bands of the silica support show negligible components. The peak at 818 cm^{-1}, e.g., almost completely vanishes. The detection of V-O-V vibrations at 548 and 695 cm^{-1} confirms the presence of oligomeric species, consistent with UV-vis spectroscopy. A summary of observed Raman bands is shown in table 5.4. The nomenclature ν_{a-f} for the six fundamental vibrations is taken from Waleska et al. [30]: V-O-Si deformation (ν_a: 461 cm^{-1}), V-O-V (ν_b: 548 cm^{-1}), V-O-V (ν_c: 695 cm^{-1}), V-O-Si (in phase) (ν_d: 914 cm^{-1}), V=O (ν_e: 1034 cm^{-1}), V-O-Si (out of phase) (ν_f: 1064 cm^{-1}), and combination bands. Exact positions can vary slightly.

Upon switching to reaction conditions, minor structural changes are observable. At 515 nm excitation, the vanadyl peak looses intensity. This indicates the reduction of vanadium to +3 or +4 as V(+3)/V(+4) species possess a lower Raman cross section.[127] In the 256.7 nm Raman spectrum, the signal around 1066 cm^{-1} increases, which may indicate either a rise of V-O-Si (out of phase) vibrations, or an additional V-O-C contribution, as recently published for an adsorbed ethoxy species.[30] Due to the poor structural dynamic observable in the low wavenumber regime, changes, like e.g. of the vanadyl overtone, are even more difficult to determine. It is reasonable that a rise of V-O-Si (out of phase) vibrations would go along with an increasing V-O-Si (in phase) band. However, the in phase Raman signal at 914 cm^{-1} is quite small, and a percentage change, of e.g. 10%, may not even be noticeable. Moreover, Nitsche [128] reported the effect of translational cell movement on the vanadyl peak. At static conditions, the vanadyl peak broadened. In the 385 and 256.7

Table 5.4: Summary of the assigned Raman features of the VO_x/SBA-15 sample

Position (cm^{-1})	Assignment		Reference
461	ν_a, V-O deformation	VO_x	[30, 117]
492	D_1 defect	SBA-15	[30, 117]
548	ν_b, V-O-V, additional V-O-Si component	VO_x	[30, 105, 126]
608	D_2 defect	SBA-15	[30, 117]
695	ν_c, V-O-V, additional V-O-Si component	VO_x	[30]
818	Si-O-Si	SBA-15	[30, 117]
914	ν_d, V-O-Si (in phase)	VO_x	[30, 105, 126]
980	Si-OH	SBA-15	[30, 117]
1034	ν_e, V=O	VO_x	[30, 105]
1064	ν_f, V-O-Si (out of phase)	VO_x	[30, 105, 126]
1151	$\nu_a + \nu_c$	VO_x	[30]
1381	$\nu_a + \nu_d$	VO_x	[30]
3743	SiO-H	SBA-15	[30, 117]

nm Raman spectra, V-O-V or V-O-Si signals decline. Additional features at 868, 2888, and 2940 cm^{-1} observed for 256.7 nm excitation can be attributed to propane, either as an adsorbed species (isopropoxide, isopropanol), or as a gas phase contribution. In order to clarify the effect of background subtraction, figure 5.5 shows the individual steps of the data processing. The intense feature at 320 cm^{-1} originates from the CaF_2 window, and appears to be asymmetric. Its presence is mainly responsible for the titled background below 800 cm^{-1}. The exact position of the stagging points is crucial. Due to the propane peak at 862 cm^{-1}, the stagging point, which is set at that position, has to be shifted to a smaller value. At 818 cm^{-1}, however, a low Raman signal of the support is expected. In the following, the actual intensity of the V-O-Si (in phase) band may have changed during the data processing. It may also be mentioned that a normalisation to the vanadyl peak was not necessary for the 256.7 nm Raman spectra obtained prior to and during the reaction. The significance of the spectral change in the region between 400 and 800 cm^{-1} is also questionable. The rise at 1066 cm^{-1}, however, is prominent in the raw data, and could be reproduced within the interference experiment (see spectra in figure S1.4).

Spectra after the reaction are compared with spectra prior to reaction in figure 5.6, indicating irreversible structural changes. The original structure did not completely restore under oxidative conditions. The decrease around 460 cm^{-1} is clearly visible, and a sharp peak arises around 1053 cm^{-1}. *Operando* Raman spectra with a central wavenumber of 1100 cm^{-1} (or 880 cm^{-1} for 385 nm excitation) are the first to be taken after 20 min of the reaction. The reaction was performed for 2h 10 min in total. Hence, spectral changes may have intensified over time. UV-vis spectroscopy points to a reduction of the oligomerisation degree after the reaction.

The region between 850 and 1300 cm^{-1} was fitted by applying a multiple peak fit analysis. Five voigt functions at around 914, 980, 1034, 1065, and 1151 cm^{-1} were used, while fixing the support contribution at 980 cm^{-1}, and Lorentzian and Gaussian width (figure 5.7). In various attempts, several peak positions and areas were also defined. The results were not satisfactory. The profile after the reaction could not be properly matched, as the feature at around 1066 cm^{-1} seemed to have shifted. The best fitting obtained is illustrated here. The data of the peak fit analysis, presented in table 5.5, should

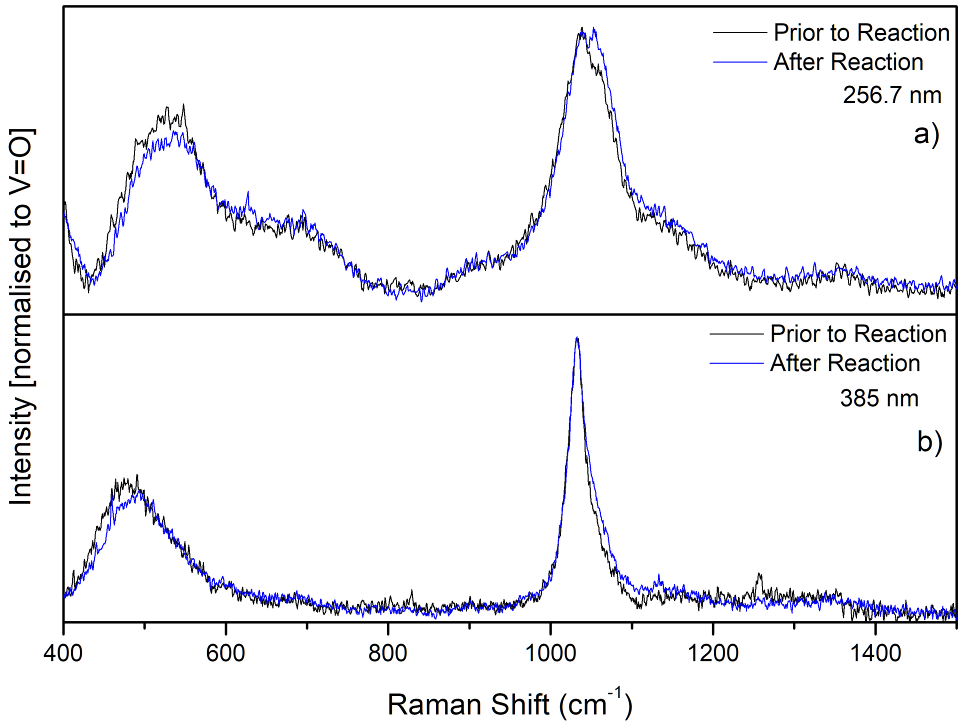

Figure 5.6: *Operando* multiwavelength Raman spectra of the 0.6 VO_x/SBA-15 catalyst prior to (black) and after (blue) propane ODH recorded at 409°C. Spectra were normalised to V=O.

be understood solely as a general trend. The band ratio between the ν_e and ν_f peak changes notably. Furthermore, the combination band around 1151 cm^{-1} is affected. Due to the low signal intensity around 914 cm^{-1}, no clear statement can be made upon the development of the V-O-Si (out of phase) vibration, as previously discussed.

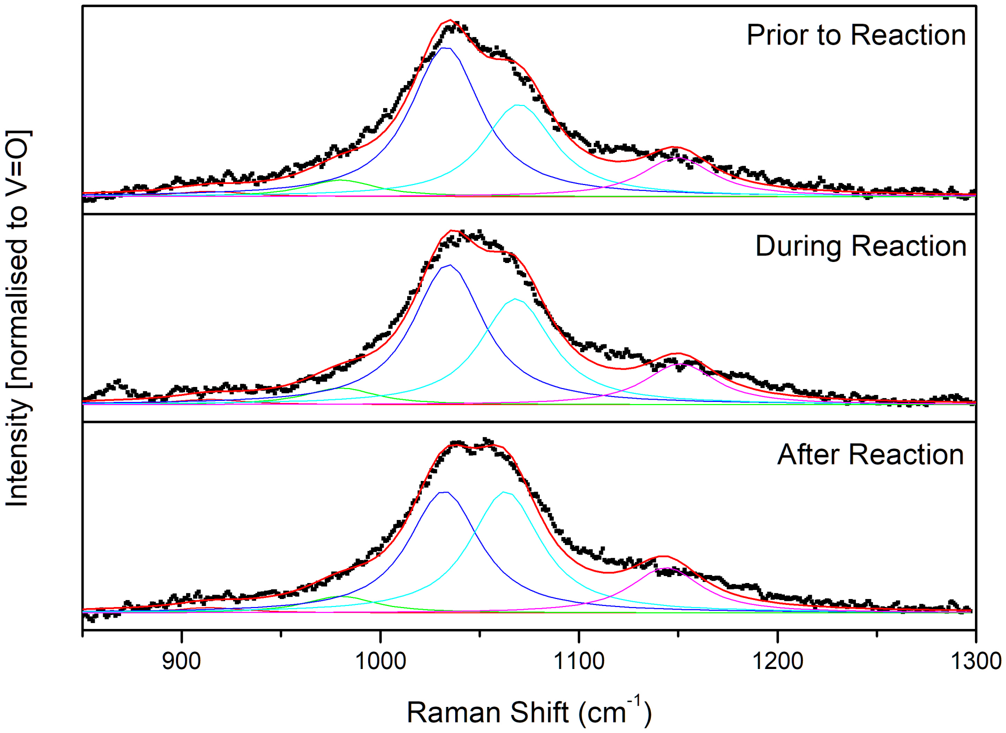

Figure 5.7: Peak fit analysis between 850 and 1300 cm^{-1}. Raman spectra of the 0.6 VO_x/SBA-15 catalyst prior to, during and after propane ODH recorded at 409°C. Spectra were normalised to V=O.

Table 5.5: Summary of the performed peak fit analysis

		Prior	During	After
ν_e	Position (cm^{-1})	1032.8	1034.2	1032.1
	Area	57.0	53.3	46.2
ν_f	Position (cm^{-1})	1069.8	1068.2	1063.0
	Area	35.1	40.4	46.0
$\nu_a + \nu_c$	Position (cm^{-1})	1149.5	1151	1143.80
	Area	14.8	15.6	17.2

In order to obtain more information about the observed propane vibrations, *operando* spectra at 256.7 nm were taken with SBA-15 as a reference. Furthermore, the detection of gas phase propane could be demonstrated by flowing a gas mixture of 12.5% of C_3H_8 through the reactor at a set temperature of 400°C. The spectra are shown in figure 5.8. For SBA-15, no Raman peak at 862 cm^{-1} due to propane is apparent, which may be explained by the lower overall intensities of propane features. A further reason may also be a resonance enhancement effect, triggered by vanadium oxide species [30], or a different focus position. Recently, Waleska et al. [30] have provided a literature overview of alkoxide-related adsorbate bands. Alcohol ODH starts with the chemisorption of an alkoxy-species, as reported multiple times. The most relevant reference for this thesis was published by Resini et al. [129]. The adsorption of isopropanol at room temperature resulted in the formation of surface isopropoxide species, as observed in FTIR spectroscopy. The conclusion was based on the missing OH deformation mode of molecularly adsorbed isopropanol in the range between 1200 and 1400 cm^{-1}. With

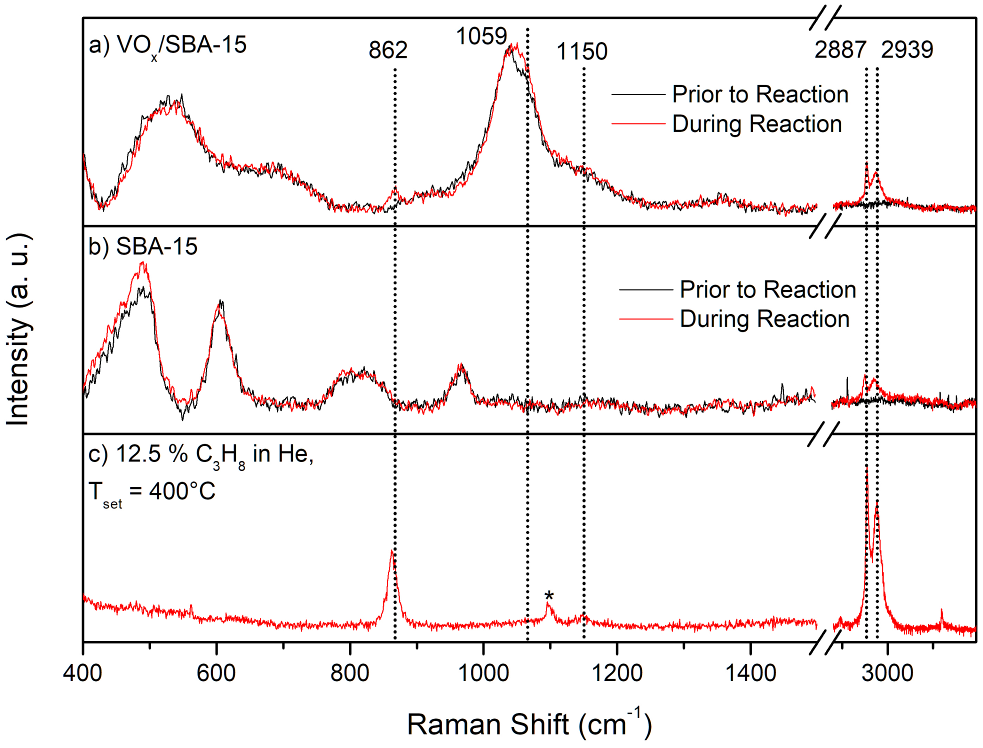

Figure 5.8: *Operando* 256.7 nm Raman spectra of the 0.6 VO_x/SBA-15 catalyst compared to bare SBA-15 prior to (black) and during (red) propane ODH recorded at 409°C. Additionally, a 256.7 nm Raman spectrum of propane gas phase is depicted. The artefact is marked with an asterisk.

increasing temperature (200°C), features attributed to isopropoxide species disappeared, without the appearance of new bands. It is suggested that propane features, observed in the 256.7 nm Raman spectra, are attributed to propane in the gas phase. Respective peak ratios match with the measured gas phase spectrum at 400°C. A possible resonance enhancement of the C-C stretching mode (862 cm^{-1}) in the presence of VO_x species cannot be finally identified due to its “apparent” absence in the SBA-15 spectrum. Unfortunately, the support contains a broad feature at around 818 cm^{-1}, which may be overlapping. Table 5.6 summarises possible assignments for observed propane bands located at 862, 2887 and 2939 cm^{-1}.

Table 5.6: Assignment of the Raman bands located at 862, 2887, and 2939 cm^{-1}

	ν(C-C)/ν(C-O) (cm^{-1})			$\nu(CH_3)$ (cm^{-1})	$\nu(CH_2)/\nu(CH_3)$ (cm^{-1})	Reference
Propane (gas phase), 400°C	862	1070 (broad)	1150	1460	2887, 2939	this work
Propane (gas phase), RT	870	1060	1170	1450	2900	[130]
VO_x/SiO_2, Isopropoxide	965, 1110, 1162				2926, 2968	[129]

***Operando* DRIFTS**

FTIR spectroscopy has been previously employed to prove the presence of surface hydroxyl groups for a silica supported vanadium oxide catalyst.[105] According to the proposed reaction mechanisms, VO-H bonds are created during the reaction. DRIFT spectra were recorded at oxidative (12.5% O_2/ 87.5% N_2) and reaction conditions (12.5% C_3H_8 / 12.5%

O_2/ 75% N_2) at a surface temperature of 409°C. Table 5.7 shows the catalytic results. Due to the high temperature necessary to obtain the desired surface temperature, the conversion was high, which is accompanied by a low selectivity towards propylene in comparison to values obtained in the Linkam cell. It is expected that the Harrick cell contributes to a significant amount of CO_x. The amount of detected gas phase components, especially that of propane, decreased significantly during the experiment, resulting in a final carbon balance of <27%. At the beginning of the experiment, the carbon balance was determined to be <1%. As the amount of products decreases proportionally with propane, similar conversion and selectivity values are obtained for the GC runs. Moreover, no leak test with Helium has been performed with the Praying Mantis accessory for this cell, so far.

Table 5.7: Summary of the catalytic performance of the 0.6 VO_x/SBA-15 during *operando* conditions in the DRIFTS experiment (Harrick cell, model HVC-DRP-4).

Experiment	X (%)	S(%)	CB(%)
0.6 VO_x/SBA-15	17.1 ± 0.4	31 ± 2	<27 (<1)

Figure 5.9 illustrates the results in the region between 1000 and 5000 cm^{-1} together with a zoomed view of the region between 3500 and 3800 cm^{-1}.

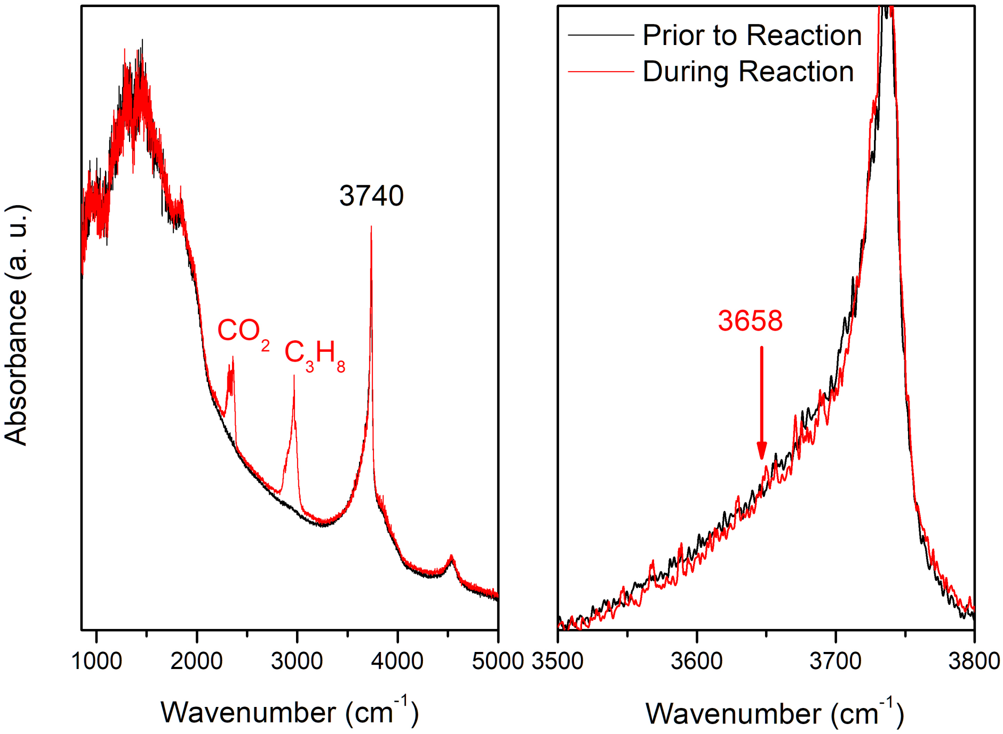

Figure 5.9: *Operando* DRIFTS spectra of the 0.6 VO_x/SBA-15 catalyst prior to (black) and during (red) propane ODH reaction at 409°C. The feed during *in situ* conditions consisted of 12.5% O_2 / 87.5% N_2; the feed during *operando* conditions consisted of 12.5% C_3H_8 / 12.5% O_2/ 75% N_2.

Vibrations in the low wavenumber regime are mainly attributed to the support together with the dominant peak at 3740 cm^{-1}, which is assigned to SiO-H vibrations.[105] During reaction conditions, two peaks between 2000 and 3500

cm^{-1} appear, which are attributed to gas phase CO_2 and C_3H_8, respectively. Due to the high applied temperature, the spectra show a low signal-to-noise ratio and a high background. VO-H vibrations are expected at around 3658 cm^{-1}, as demonstrated for (partly) hydrated vanadium oxide species at room temperature [105]. Under the applied conditions no contribution is detectable. Possible adsorbates would have been expected in the region between 1200 and 1900 cm^{-1} [116], but cannot clearly identified.

5.3 Interference experiment

Interference experiments were conducted at 409°C, applying UV-vis, Raman, and DRIFT spectroscopy in order to trigger structural dynamics. Spectra were taken prior to and during reaction conditions, which is followed by a reductive environment in the absence of oxygen. For *operando* conditions a mixture of 12.5% C_3H_8 / 12.5% O_2 in either He (Raman) or N_2 (UV-vis and DRIFT) was applied. The feed after the reaction consisted of 12.5% C_3H_8 in the inert gas.

Figure 5.10 shows the UV-vis spectra during *operando* and reductive conditions. The rise in the vis region clearly indicates the change in oxidation state from V(+5) to V(+4)/V(+3). At the same time, the band edge energy shift from 3.02 ± 0.02 eV to 3.14 ± 0.07 eV, pointing to a decreased oligomerisation degree. As the shape of the spectrum under reductive conditions shows a significant change, the exact determination of the band edge energy is impeded, resulting in a higher uncertainty. The absorption decreases between 220 and 350 nm, which indicates that long-chain, short-oligomeric, and trimeric/dimeric species are reduced in the presence of propane. Contributions between 200 and 220 nm, mainly attributed to monomeric vanadium oxide species, remain relatively unaffected.

The Raman experiment at an excitation wavelength of 515 nm demonstrates the ongoing reduction of supported vanadium oxide species. Vibrations are detected at 492 and 818 cm^{-1}, which are assigned to D_1 (SBA-15) and Si-O-Si, respectively. As the vanadyl peak completely vanishes, the peak at 1066 cm^{-1}, attributed to the TO vibration of the silica support, becomes more apparent. Signals at 608 and 3743 cm^{-1}, which are related to the silica support, are not visible anymore. In contrast, the Raman spectrum at an excitation wavelength of 256.7 nm hardly shows any structural changes. The signal at 460 cm^{-1} notably decreased. Due to the overlapping noise for these spectra, no statement can be made on the overall shape of the vanadyl peak. The low intensity of peaks, corresponding to gas phase propane, can be explainable by a different focus position.

A complementary DRIFT experiments did not detect any VO-H vibrations under reductive conditions. The combined results indicate that highly-oligomerised vanadium oxide species are affected under propane reduction, which leads to the breakage of V-O-V bonds and the formation of smaller aggregates. The 256.7 nm Raman spectrum exhibits VO_x units, still containing short-chain oligomeric species as identified by the V-O-V contributions at 548 and 695 cm^{-1}.

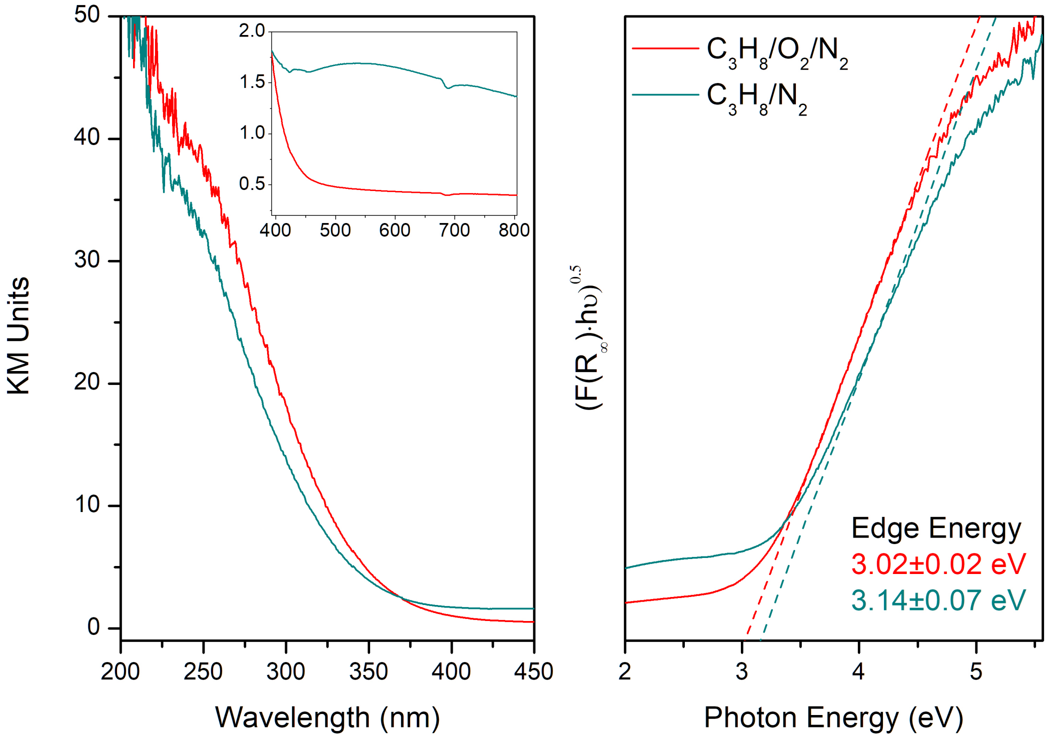

Figure 5.10: *Operando* UV-vis spectra of the 0.6 VO_x/SBA-15 catalyst during propane oxidative (red) and reductive (green) conditions recorded at 408°C.

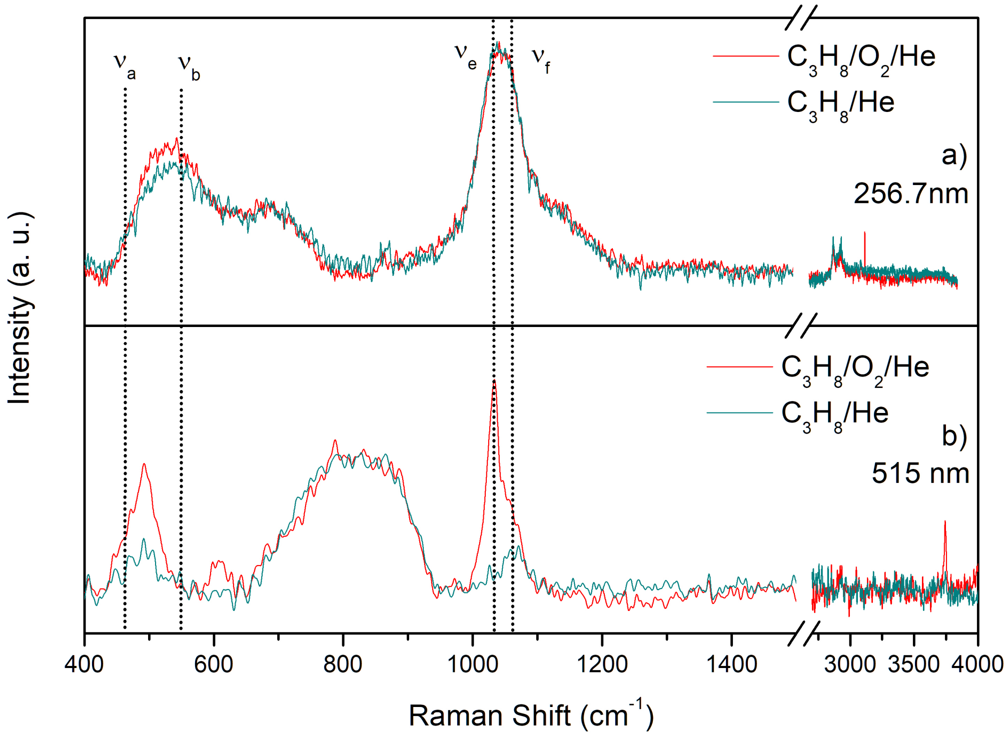

Figure 5.11: *Operando* multiwavelength Raman spectra of the 0.6 VO_x/SBA-15 catalyst during propane oxidative (red) and reductive (green) conditions recorded at 409°C. The 256.7 nm spectra were normalised to V=O.

Operando experiments at lower reaction temperatures might be a promising and complementary approach due to lower reaction rates and a higher selectivity. Moreover, the observation of adsorbates is more probable.

The experimental procedure for UV-vis, Raman, and DRIFTS measurements is as described in 3.3.1. The feed during *operando* conditions consisted of 12.5% C_3H_8 / 12.5% O_2 in either He (UV-vis, Raman) or N_2 (DRIFTS) with a total flow of 40 ml_n/min. A surface temperature of 299°C with a propane conversion of less than 1% was chosen.

The UV-vis results are shown in figure 5.12. The spectra prior to, during, and after the reaction do not show any noticeable differences.

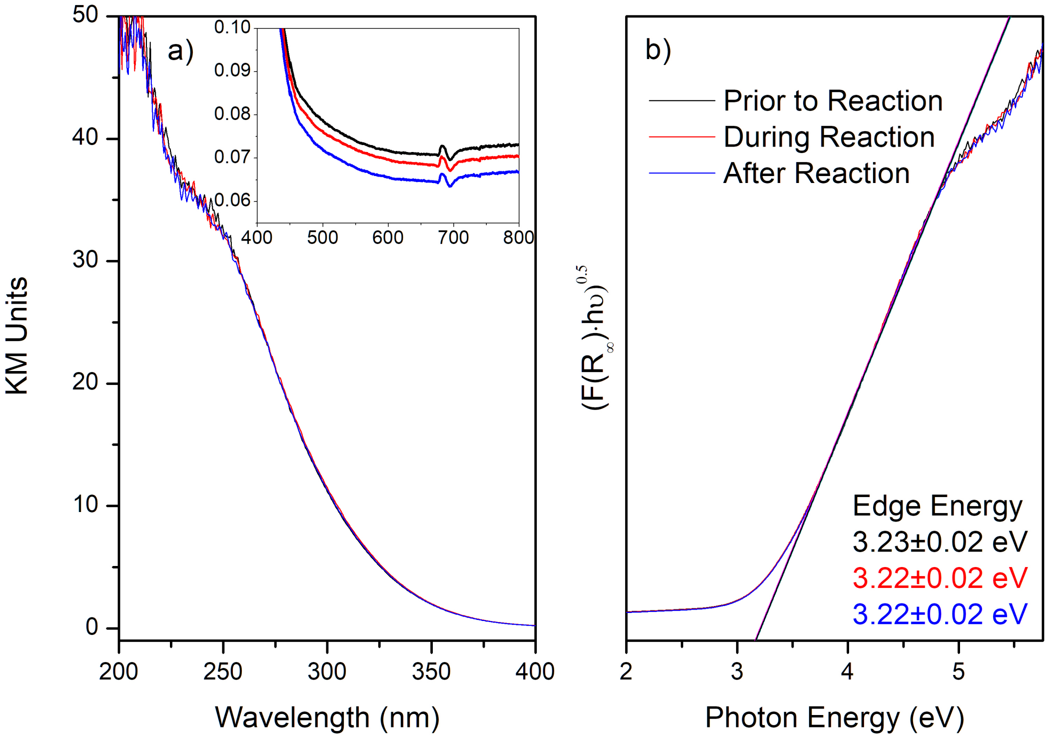

Figure 5.12: *Operando* UV-vis spectra of the 0.6 VO_x/SBA-15 catalyst prior to (black), during (red), and after (blue) propane ODH recorded at 297°C. The feed during *in situ* conditions consisted of 12.5% O_2 / 87.5% He; the feed during *operando* conditions consisted of 12.5% C_3H_8 / 12.5% O_2/ 75% He.

No rise in the pre-edge adsorption is observable. The decline in the vis-region even causes a doubt about the significance of these observed changes at these low levels. Either the reaction did not take place at the surface or the amount of reduced species was too low to be detectable. The catalyst shows a band gap of 3.23 ± 0.02 eV, which corresponds to approximately 1.8 V-O-V.

As suggested by the UV-vis results, the *operando* 256.7 nm Raman data do not exhibit any structural dynamics (see figure 5.13). Propane gas phase peaks have higher overall intensities. Due to cosmic rays and noise around the vanadyl peak, changes are not clearly evident in this region.

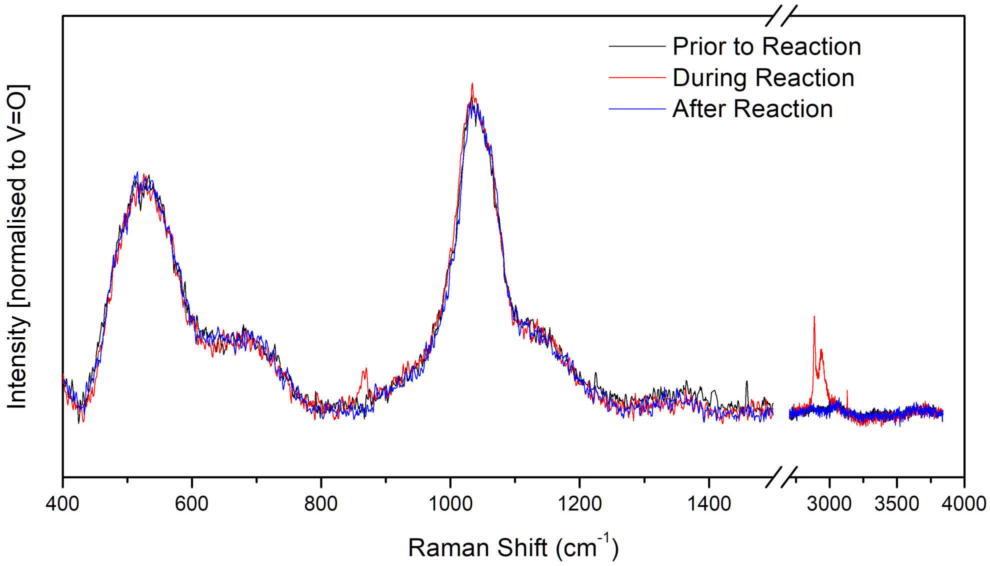

Figure 5.13: *Operando* Raman spectra of the 0.6 VO_x/SBA-15 catalyst prior to (black), during (red), and after (blue) propane ODH recorded at 299°C. Spectra were normalised to V=O. The feed during *in situ* conditions consisted of 12.5% O_2 / 87.5% He; the feed during *operando* conditions consisted of 12.5% C_3H_8 / 12.5% O_2/ 75% He.

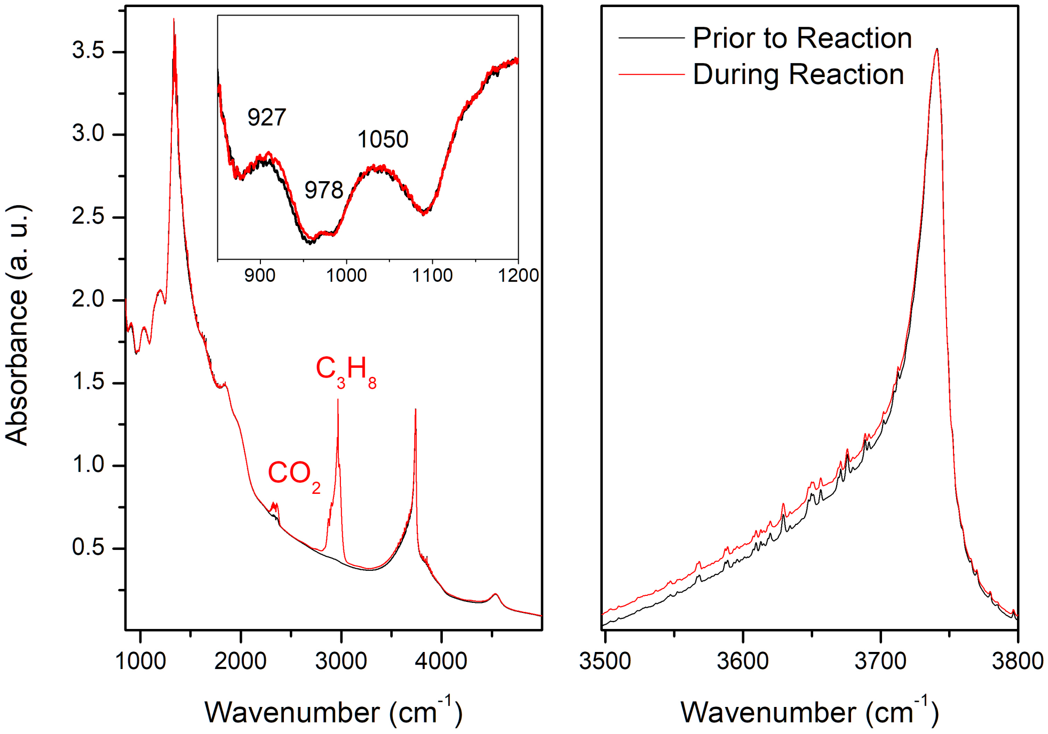

Figure 5.14: *Operando* DRIFT spectra of the 0.6 VO_x/SBA-15 catalyst prior to (black) and during (red) propane ODH recorded at 299°C. The feed during *in situ* conditions consisted of 12.5% O_2 / 87.5% N_2; the feed during *operando* conditions consisted of 12.5% C_3H_8 / 12.5% O_2/ 75% N_2.

The detection of CO_2 vibrations around 2000 cm^{-1} in the *operando* DRIFT spectrum (see figure 5.14) suggests that the reaction was taking place during the *operando* measurement (set temperature: 496°C). The signal-to-noise ratio is notably improved in comparison to a spectrum obtained at higher temperatures. The changes are evident in the low wavenumber regime, where mainly lattice vibrations can be found. Nevertheless, no adsorbates, such as isopropoxide, or VO-H vibrations are detectable. Support features at 978 and 1050 cm^{-1} are attributed to Si-OH and Si-O-Si vibrations, respectively. The band at 927 cm^{-1} corresponds to V-O-Si vibrations, and increases slightly during the reaction.

5.5 Temperature variation

5.5.1 Temperature effect on vanadium oxide

The direct comparison of the *in situ* 256.7 nm Raman spectra obtained at 409 and 299°C raises the question if the catalyst was in the same initial state before starting the reaction. It may be possible that the catalysts differed in their oligomerisation degree, which may be a result of the respective employed temperature, as also indicated via UV-vis spectroscopy. Hence, the effect of temperature was studied in a separate experiment. The catalyst was dehydrated at a bottom temperature of 502°C. Raman spectra were taken at a surface temperature of 409, 152, 299, and 446°C in oxidative conditions (12.5% O_2 /87.5% He) in a fluidised bed mode. *In situ* UV-vis spectra were taken from the *in situ* hydrogen reduction experiment during oxidative conditions (12.5% O_2 /87.5% He) at 372 and 77°C. Figure 5.15 shows the UV-vis results. The band energy shifts from 3.04 ± 0.02 eV to 3.23 ± 0.02 eV, while cooling down. Furthermore, absorption decreased.

The temperature-dependent Raman spectra between 152 and 446°C are depicted in figure 5.16. With increasing temperature, the overall Raman intensities decrease, which might be either attributed to an increasing absorption, as demonstrated via UV-vis spectroscopy, or to a a different focus position due to a different particle movement (fluidised bed). Hence, spectra were normalised to V=O for comparison. Several changes are apparent. The ratio between components at 548 cm^{-1} and 695 cm^{-1} changes, which are mainly attributed to V-O-V vibrations. Special attention was put on background subtraction during data processing. Although an erroneous impact cannot be excluded, the effect is already apparent by comparing the raw data. The vanadyl experiences a red shift with increasing temperature, which goes along with a peak ratio change between V=O and V-O-Si (out of phase). Peak fitting analysis (figure 5.17) was performed while fixing the support contribution at 980 cm^{-1}, and Lorentzian and Gaussian width. The final results are summarised in figure 5.18. With increasing temperature, peak areas of the V=O features increase while the V-O-Si (out of phase) successively decreases. The combination band at 1151 cm^{-1} may serve as an indicator for changes in V-O-Si (461 cm^{-1}) and V-O-V (695 cm^{-1}), however, the shoulder could not be described adequately at high temperatures.

The *operando* study by Waleska et al. [30] included a temperature-dependent UV-vis study with temperatures up to 291°C for a silica supported vanadium oxide under oxidative conditions. Recently, Nitsche and Hess [105] demonstrated that a decreasing band edge energy is an indicator for an increasing degree of oligomerisation. Gao et al. [131] summarised possible effects on edge energy shifts based on the analysis of several vanadium oxide reference substances. In general, the band edge energy shift may arise either due to a oligomerisation of the V cation, changes in coordination geometry, or changes in the second coordination sphere around V(V) cations. Xie et al. [132] explicitly studied the temperature effect

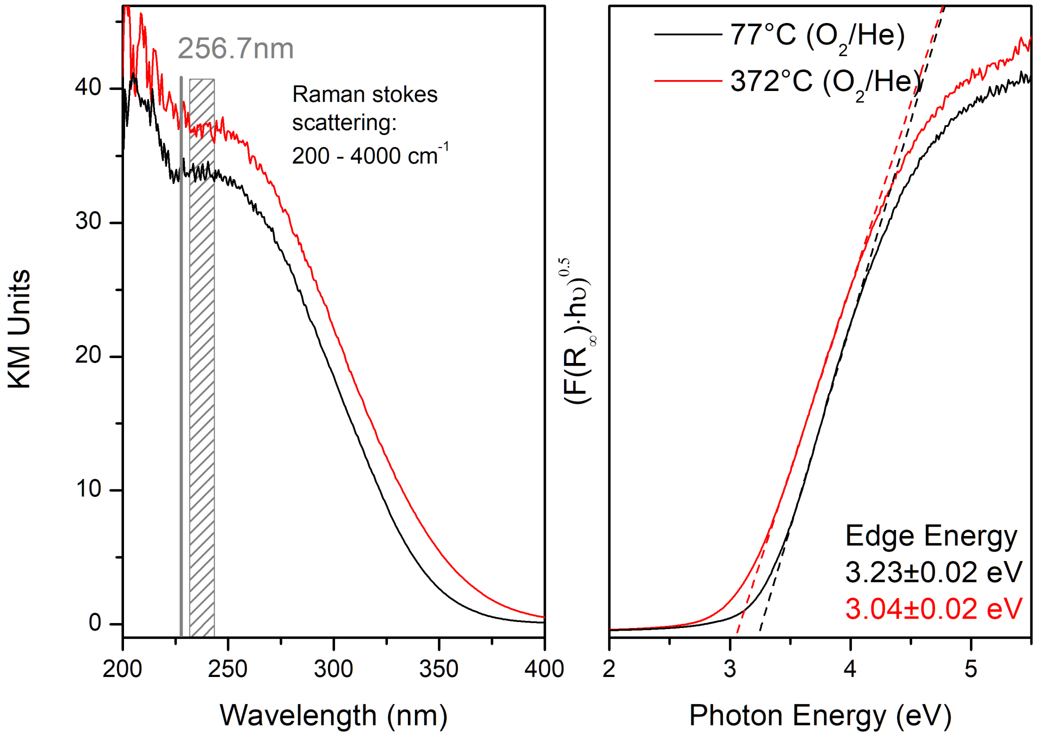

Figure 5.15: *In situ* UV-vis spectra of the 0.6 VO_x/SBA-15 catalyst at different temperatures. The *in situ* condition consisted of 12.5% O_2 / 87.5% He.

of bulk and dispersed oxides. Bulk oxides like V_2O_5 exhibit an increase in optical absorption with increasing temperature which was attributed to to a loss of oxygen and the consequent formation of nonstoichiometric oxides and stoichiometric suboxides.

In the case of the Raman study, Wu et al. [117] previously reported a temperature effect on highly-dispersed vanadium oxide. The feature at 1060 cm^{-1} decreased relatively more than at 1032 cm^{-1}. It was attributed to the weaker metal-oxygen bond according to Xie et al. [132]. When the increase in optical absorption is significant at or near the frequency of the laser used for Raman spectroscopy, a loss in Raman signal intensity is expected due to a decrease in sampling depth, and is even more drastic for weak metal-oxygen bonds. Hence, the features at 1032 and 1060 cm^{-1} may experience a different resonance effect depending on the temperature (resonance effect versus self absorption). The downward shift is observed for both, V_2O_5 and supported vanadium species, attributed to thermal expansion and changes in the population of the vibrational energy levels with increasing temperature.[132] In recent years, the structure of supported vanadium oxide species has been studied extensively [105, 115, 117]. Proposed structures include the long-time accepted pyramidal model (trigrafted), bigrafted model, and umbrella model (monografted). Also the effect of hydration has been intensively discussed [102, 105, 131, 133]. Dispersed vanadium species are quite sensitive to moisture, like water, at low temperatures. Hence, Nitsche and Hess [105] proposed several structures for highly dispersed vanadium oxide under dehydrated conditions containing hydroxyl groups, based on their spectroscopic data. With increasing V-O-V bonds ribbon-like aggregates are also mentioned as a result of condensation.

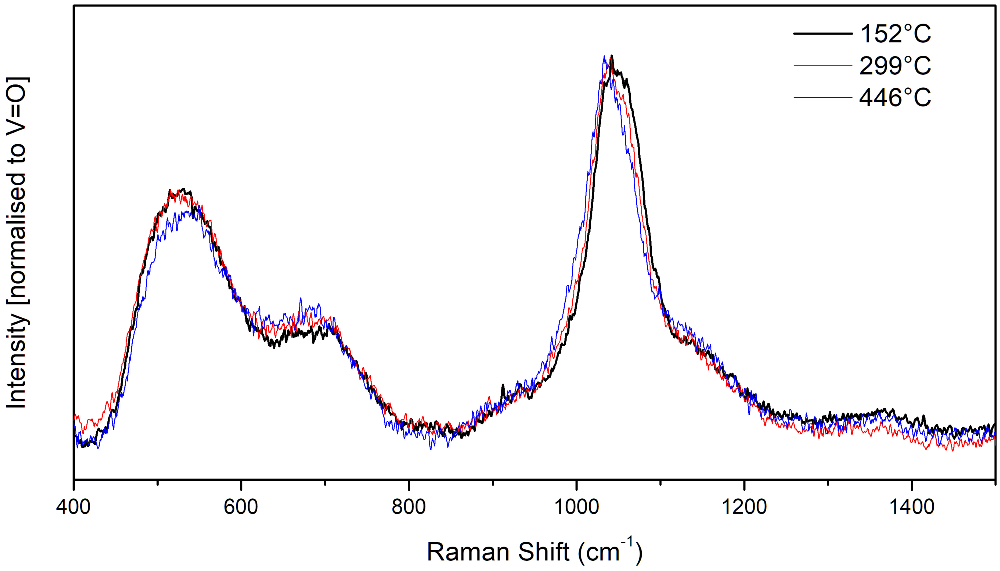

Figure 5.16: *In situ* 256.7 nm Raman spectra of the 0.6 VO$_x$/SBA-15 catalyst at different temperatures. The *in situ* condition consisted of 12.5% O$_2$ / 87.5% He.

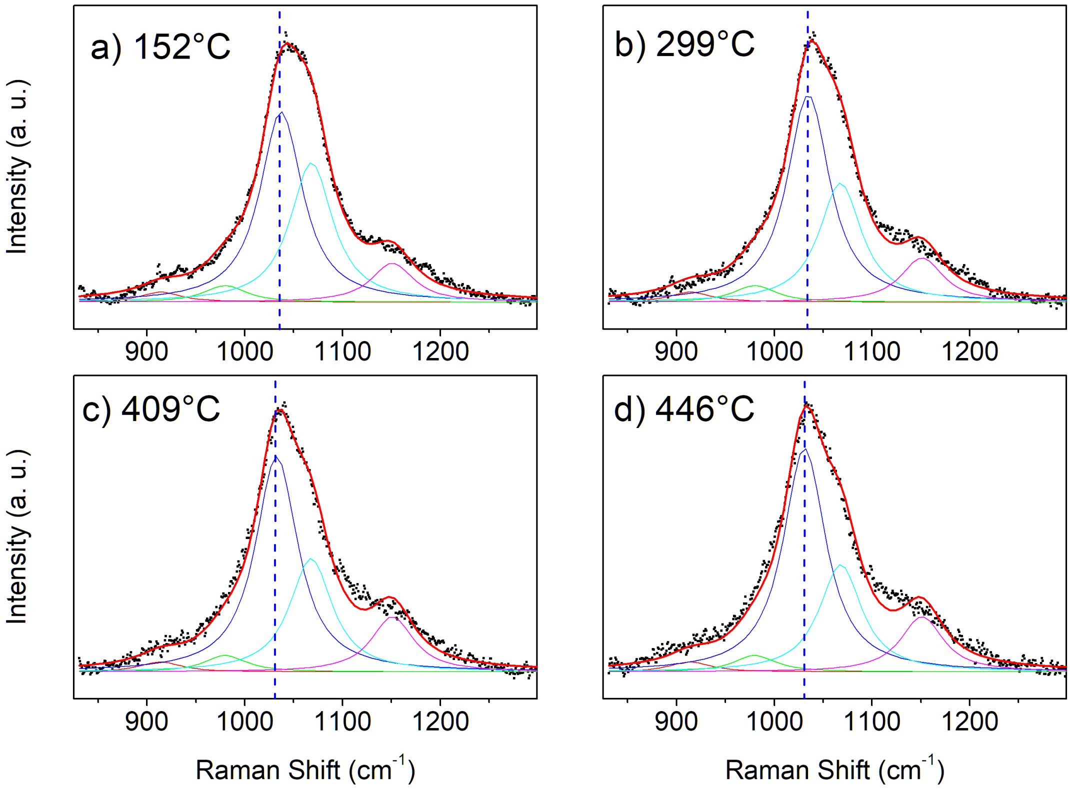

Figure 5.17: Peak fit analysis between 850 and 1300 cm^{-1}. Raman spectra of the 0.6 VO$_x$/SBA-15 catalyst at different temperatures. Spectra were normalised to V=O.

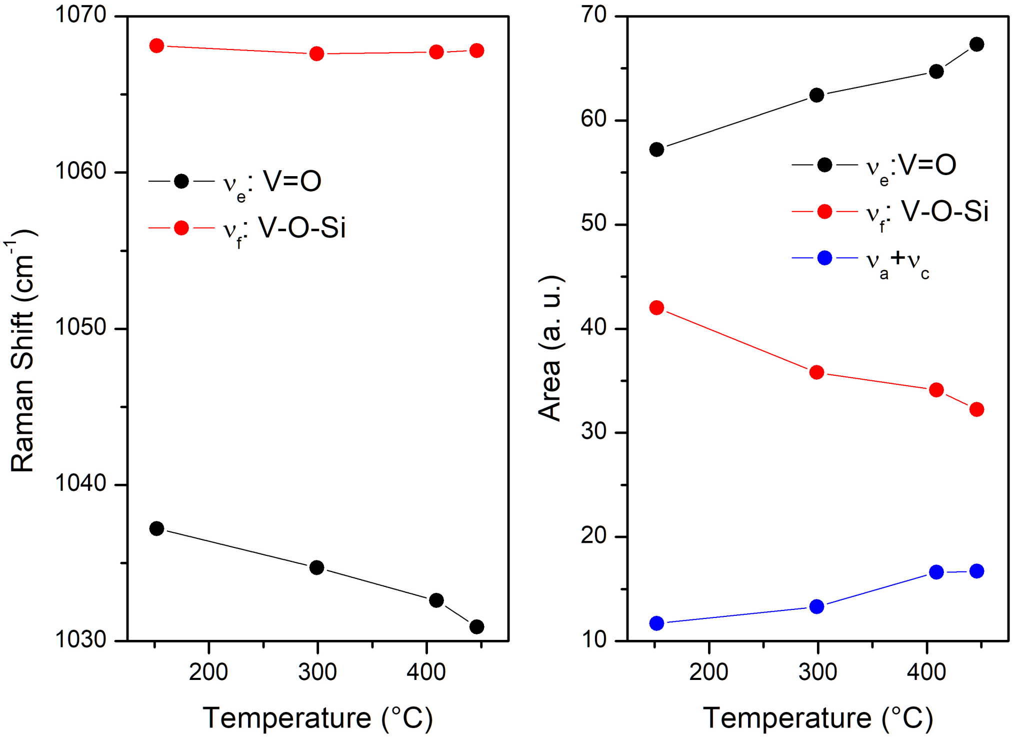

Figure 5.18: Correlation of the Raman shifts and peak areas of the V=O, V-O-Si, and the combination band at 1150 cm^{-1} with temperature.

5.5.2 Temperature effect on gas phase propane

The previous sections have demonstrated the potential to detect gas phase contributions while applying excitation wavelengths of high energy. The molecule propane has a C_{2v} symmetry. Several theoretical and experimental studies have identified 27 distinct vibrational modes.[134] As a result, vibrational spectra appear quite complex. Here, Raman spectra were taken at a concentration of 12.5% C_3H_8 in He at a total flow of 40 ml_n/min. The temperature dependency was studied while heating up to a set temperature of 600°C. As the measurements were performed in the empty cell, the temperature is specified as the set temperature. The results are shown in figure 5.19 and respective peak assignments are summarised in table 5.8.

At room temperature several Raman peaks are visible. In the high Raman shift region, the observed features at 2884, 2911, 2930, 2960, and 2972 cm^{-1} are comparable to the peaks in the spontaneous Stokes–Raman scatterings spectrum obtained by Magnotti et al. [136]. The region between 2900 and 3000 cm^{-1} is described to contain several contributions of asymmetric stretching modes of CH_3 and CH_2 stretching modes, combined with several combinations and overtones. The spectra show a clear temperature dependency upon heating to 600°C. At high Raman shift values, peak amplitudes decrease continuously with temperature. However, the dominant peak at 2884 cm^{-1} shows comparatively larger drop. At high temperatures the sharp feature has a similar height like its neighbouring broad region. At the same time, the peak width at initially 2950 cm^{-1} becomes smaller. The C-C stretching mode at 866 cm^{-1} shows a red shift and is broadened and

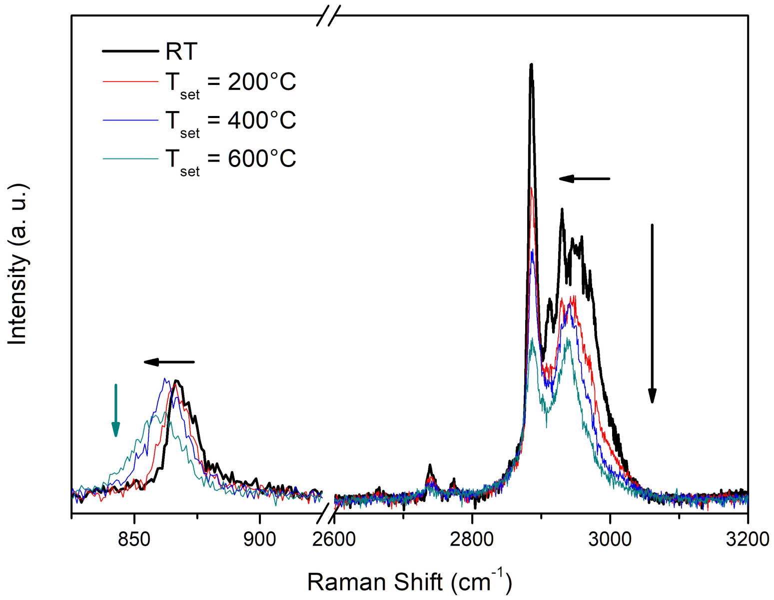

Figure 5.19: 256.7 nm Raman spectra of gas phase propane at different temperatures. RT is short for room temperature

Table 5.8: Summary of detected gas phase vibrations, obtained in this work, and reference data. RT is short for room temperature.

this work, RT	liquid [135]	gas, theory [130]	theory [130, 134]	assignment
	375 (W)	370	369	C-C-C bending
866 (S)	867 (S)	870	869	C-C stretch
	940 (VW)		922	CH_3 rocking
1070	1054 (M)	1060	1053	C-C stretch, CH_3 rocking
1154	1152 (W)	1170	1158, 1192	CH_3 rocking
	1278 (W)		1292	CH_2 twist, CH_3 rocking
	1338 (M)	1305	1338	CH_2 wag, CH_2 rocking
			1392,1378	CH_3 symm. deform
1464 (M)	1451 (S)	1450	1462, 1476	CH_3 non-symm. deform, CH_2 deform
2739, 2772				
2884 (S)			2887	CH_3 symm. stretch
2960 (S)	2967 (M)	2900	2962, 2968	CH_3 non-symm. stretch
2972 (S)			2973, 2977	CH_2 stretch

decreased at 600°C. In conclusion, peak ratios may change upon temperature. This has to be considered when interpreting Raman spectra at different temperatures.

5.5.3 *In situ* DRIFT study of propane adsorption at various temperatures

In situ DRIFT studies were performed in order to obtain information on possible propane adsorption and propoxide formation at low temperatures. KBr was measured at various temperatures for background subtraction before starting the experiment. The 0.6 VO_x/SBA-15 sample was dehydrated (12.5% O_2 / 87.5 % N_2 and cooled down to room temperature, before mixing propane and oxygen into the gas phase (12.5% C_3H_8 / 12.5% O_2/ 75% N_2). The temperature was gradually increased until a maximum surface temperature of 409°C. Shee and Deo [116] provided an overview of IR band assignments of possible surface species formed during the adsorption of ethane or propane. Species like ethoxide, propoxide, acetone, acetaldehyde, formate, acetate, cyclic anhydride, and olefins have been considered. Corresponding IR bands are located between 1200 and 1900 cm^{-1}. In this experiment, no adsorbate species were observable for the silica supported vanadium oxide sample. Hence, figure 5.20 illustrates only the O-H region between 3500 and 3800 cm^{-1}. As the background rises with temperature, spectra were offset for better visibility. VO-H vibrations are detected for the dehydrated sample at room temperature. The vibration decreases with temperature until it finally vanishes at a temperature of 299°C.[133] At room temperature, an additional broad feature is observed between 3670 and 3730 cm^{-1} in the presence of propane. Previously, a broad area between 3740 - 3450 cm^{-1} has been assigned to hydrogen-bonded hydroxy silanol groups.[129] Vibrations at 3740 - 3720 cm^{-1} have been attributed to hydrogen perturbed OH species.[137] In order to exclude gas phase contributions, the room temperature experiment was repeated with a background previously taken, which consisted of KBr + 12.5% C_3H_8 / 12.5% O_2/ 75% N_2. Figure 5.21 demonstrates that propane features are not completely eliminated, which may indicate the adsorption of propane at room temperature. However, a slightly different propane concentration cannot be excluded. The broad feature between 3675 and 3725 cm^{-1} remains unaffected by the background subtraction. It is assumed that propane is physisorbed. Kämper et al.[138] studied the physisorption of propane molecules on the (001) surface of vanadium pentoxide. They concluded that the energetically most favoured sites for adsorption are located between two double rows of vanadyl oxygens.

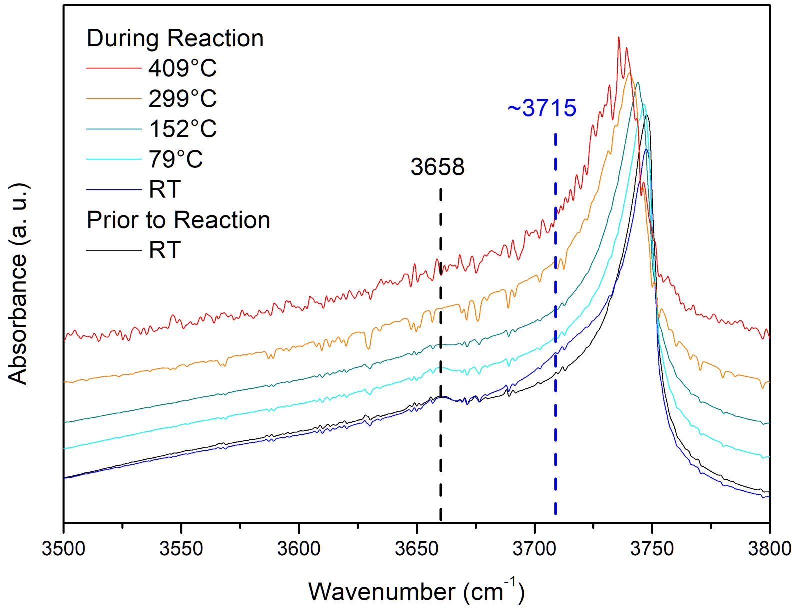

Figure 5.20: *In situ* DRIFT spectra of the 0.6 VO_x/SBA-15 catalyst at propane oxidative conditions (12.5% C_3H_8 / 12.5% O_2/ 75% N_2) in dependency of the temperature. RT is short for room temperature. Spectra are depicted with an offset.

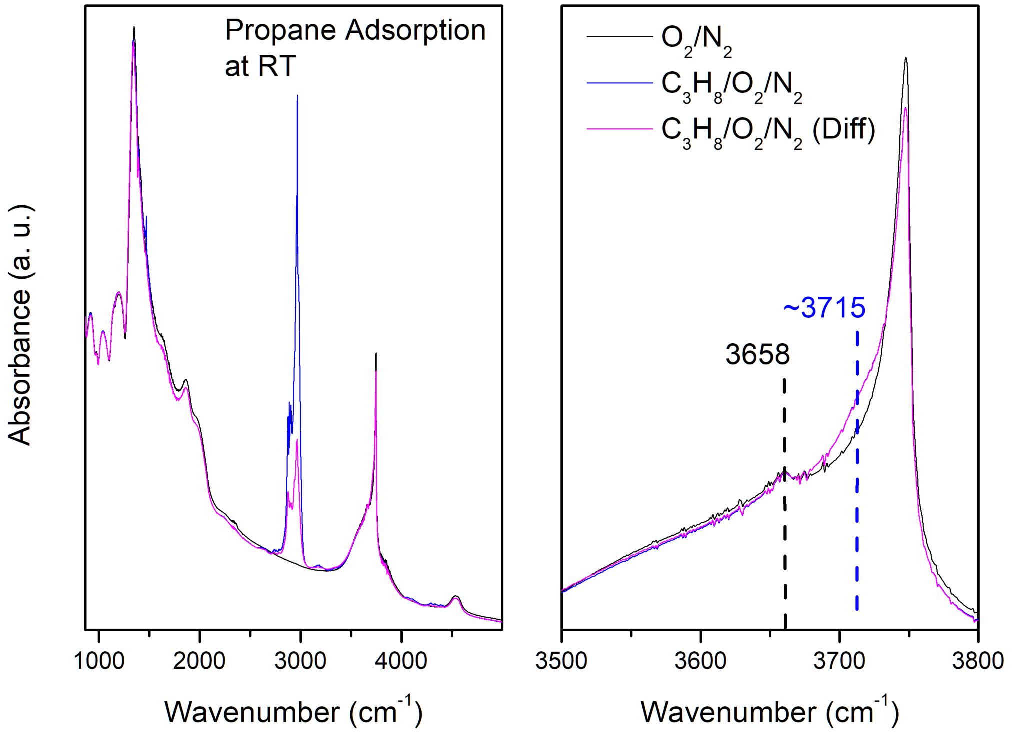

Figure 5.21: *In situ* DRIFT spectra of the 0.6 VO_x/SBA-15 catalyst at propane oxidative conditions (12.5% C_3H_8 / 12.5% O_2/ 75% N_2) at room temperature. The background spectrum for the difference spectrum (Diff) consisted of KBr + C_3H_8 + O_2 + N_2 at room temperature (RT).

Propane Reduction

DR UV-vis spectra of the propane reduction experiment are shown in figure 5.22. The 0.6 VO_x/SBA-15 sample was dehydrated for one hour at oxidative conditions (12.5% O_2/ 87.5 % He) before starting the experiment. The temperature was cooled down to a sample temperature of 77°C and successively increased in a gas composition consisting of 12.5% C_3H_8/ 87.5 % He at a total flow of 40 ml_n/min. UV-vis spectra were taken after 5 min, respectively. Likewise, a complementary UV Raman experiment (256.7 nm) was designed as illustrated in figure 5.23. However, experiments are not entirely comparable as the duration of the Raman and UV-vis measurements differ from each other.

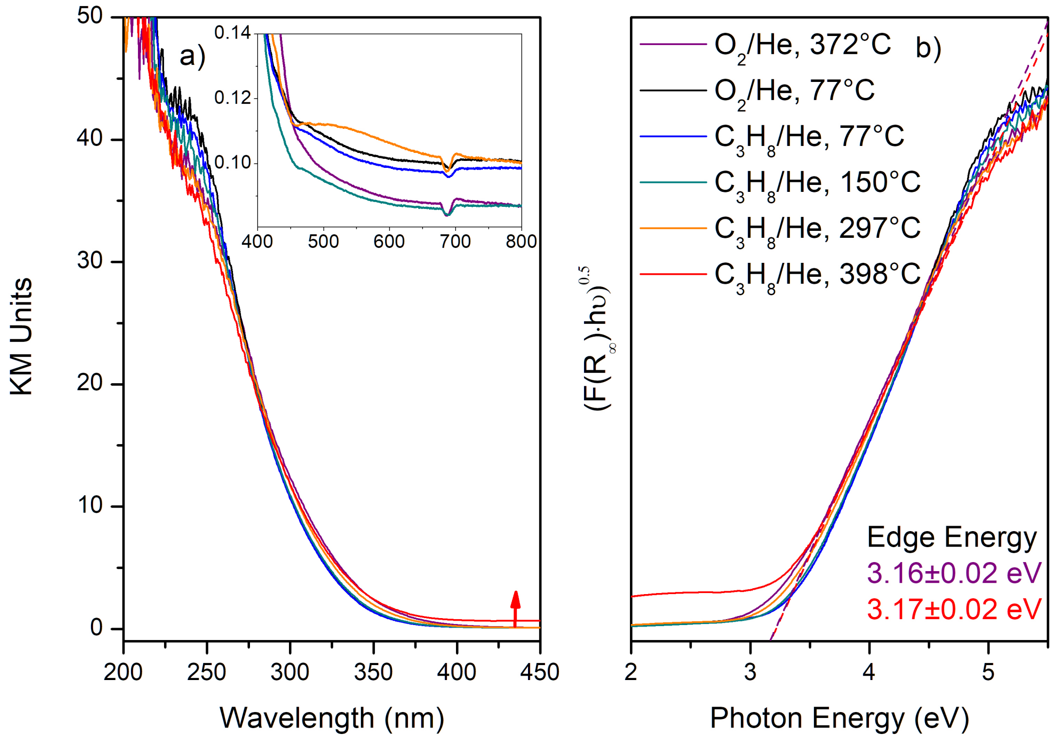

Figure 5.22: *In situ* UV-vis spectra of the 0.6 VO_x/SBA-15 under reductive conditions (12.5% C_3H_8 in He). The temperature was gradually increased from 77 to 398°C.

When interpreting the data, the respective effect of temperature has to be considered. A clear indication of sample reduction in the UV-vis data is the rise in absorption between 450 and 650 nm at 297°C, which intensifies with increasing temperature. A shift in band edge energy is expected, as shown for the interference experiment, however, cannot be separated from the temperature-dependent shift, occurring at the same time. 256.7 nm Raman spectra were conducted starting at a temperature of 152°C. Slight changes are already detected at 152°C under propane reductive conditions. The amount of V-O-V bonds is decreased, and contributions around the vanadyl region indicate an increase at 1063 cm^{-1}. At 446°C, supported vanadium oxide species are clearly affected. SiO-H vibrations arise at 3730 cm^{-1}, and carbon species are

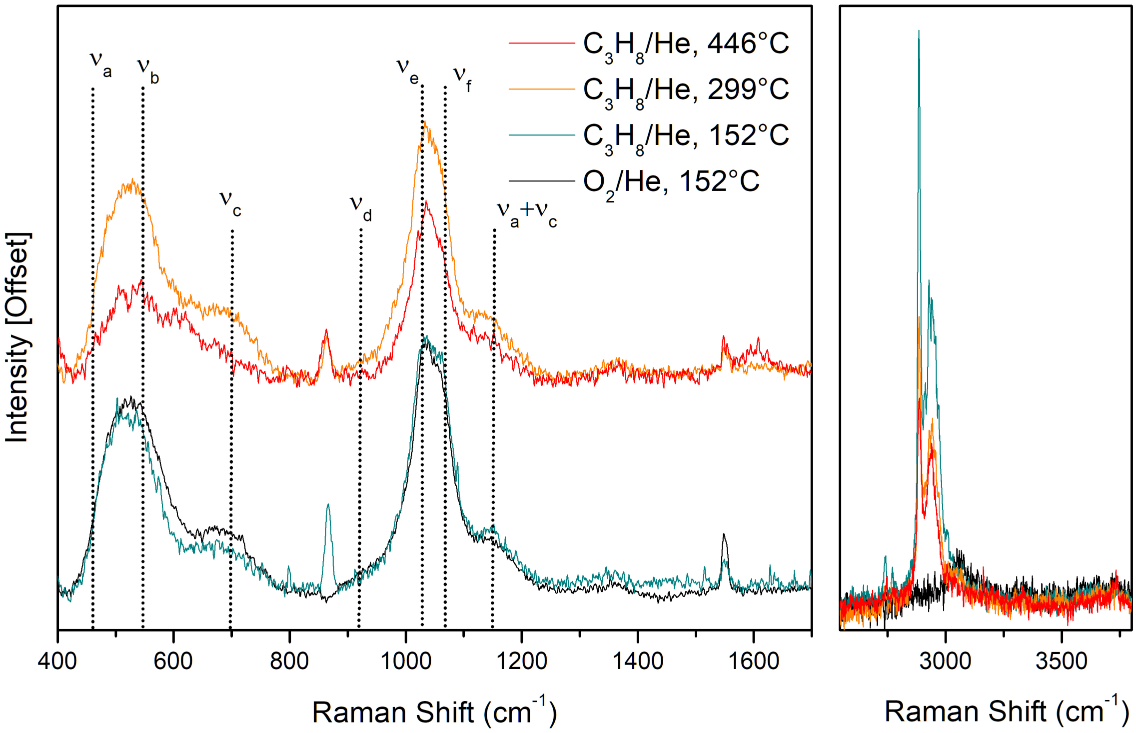

Figure 5.23: *In situ* 256.7 nm Raman spectra of the 0.6 VO_x/SBA-15 under reductive conditions (12.5% C_3H_8 in He). The temperature was gradually increased from 152 to 446°C. Spectra were depicted with an offset.

detected at 1600 cm^{-1}, indicating the burning of propane molecules. The detection of intact V=O and V-O-Si vibrations suggests that supported vanadium oxide species are not fully reduced. Results, obtained at 446°C with an excitation wavelength of 385 nm (see figure S1.5), indicate that low-oligomeric species are affected first under propane reducing conditions. However, the Raman intensity decrease may also be explained by an increasing self-absorption, observable via UV-vis spectroscopy. Highly reduced vanadium oxide species still contain V-O-V bonds as indicated via 256.7 nm Raman spectroscopy.

Hydrogen Reduction

Hydrogen reductive experiments were performed in a similar manner as described for propane. The feed consisted of 7.5% H_2 in Ar at a total flow of 40 ml_n/min. *In situ* UV-vis results are illustrated in figure 5.24. At a temperature of 297°C, the pre-edge absorption in the vis region shows a rise, which indicates the ongoing reduction of vanadium 5+ to 3+/4+. This observation becomes more prominent with increasing temperature. At 445°C, the total area below 350 nm clearly declines, and a decrease of the average amount of V-O-V is assumed. Respective Raman results are presented in figure 5.25.

Spectra are subject to a temperature effect, which makes it difficult to derive the exclusive effects of reduction. At 152°C, the oxidative and reductive Raman spectra overlap almost completely. It is suggested that the sample is already (slightly) reduced around 299°C, however, there are no obvious signs in the 256.7 nm Raman spectrum. The spectrum at 446°C was normalised to 608 cm^{-1} as a reference point. The position includes a contribution of the D_2 defect band of silica.

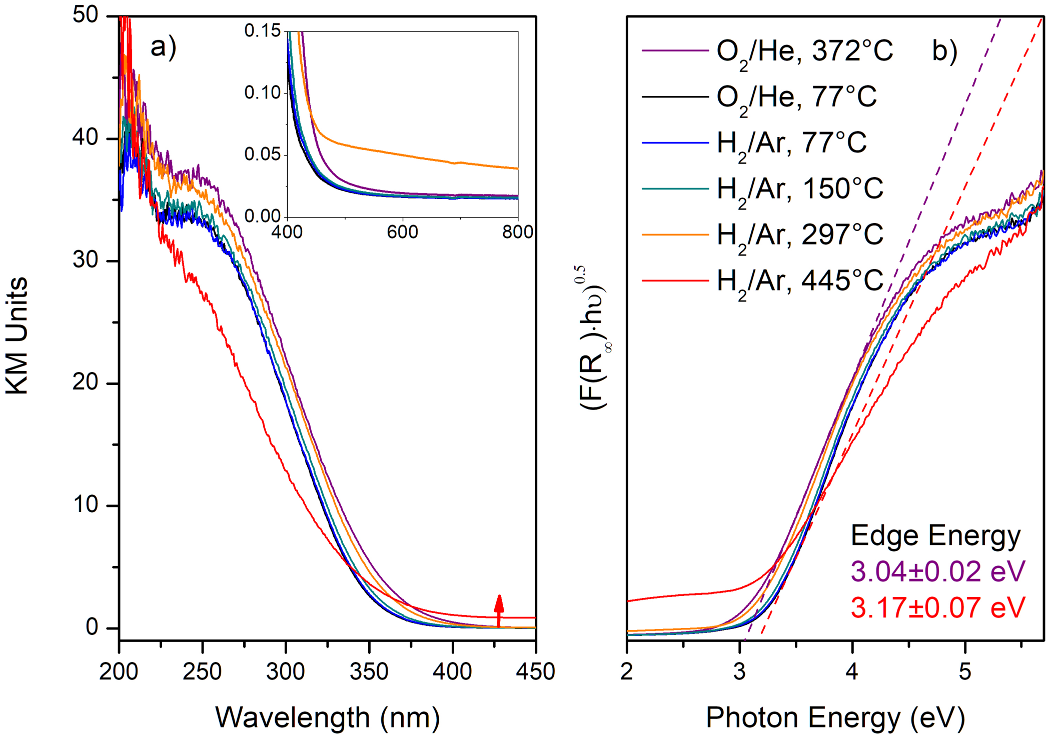

Figure 5.24: *In situ* UV-vis spectra of the 0.6 VO_x/SBA-15 under reductive conditions (7.5% H_2 in Ar). The temperature was gradually increased from 77 to 445°C.

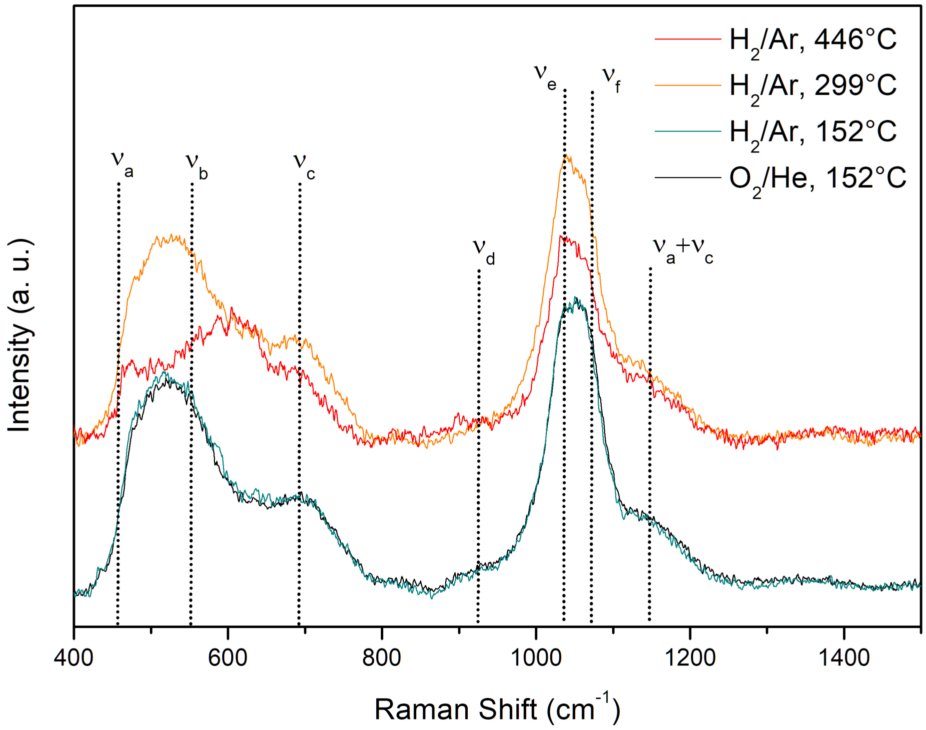

Figure 5.25: *In situ* 256.7 nm Raman spectra of the 0.6 VO_x/SBA-15 under reductive conditions (7.5% H_2 in Ar). The temperature was gradually increased from 152 to 446°C. Spectra were depicted with an offset.

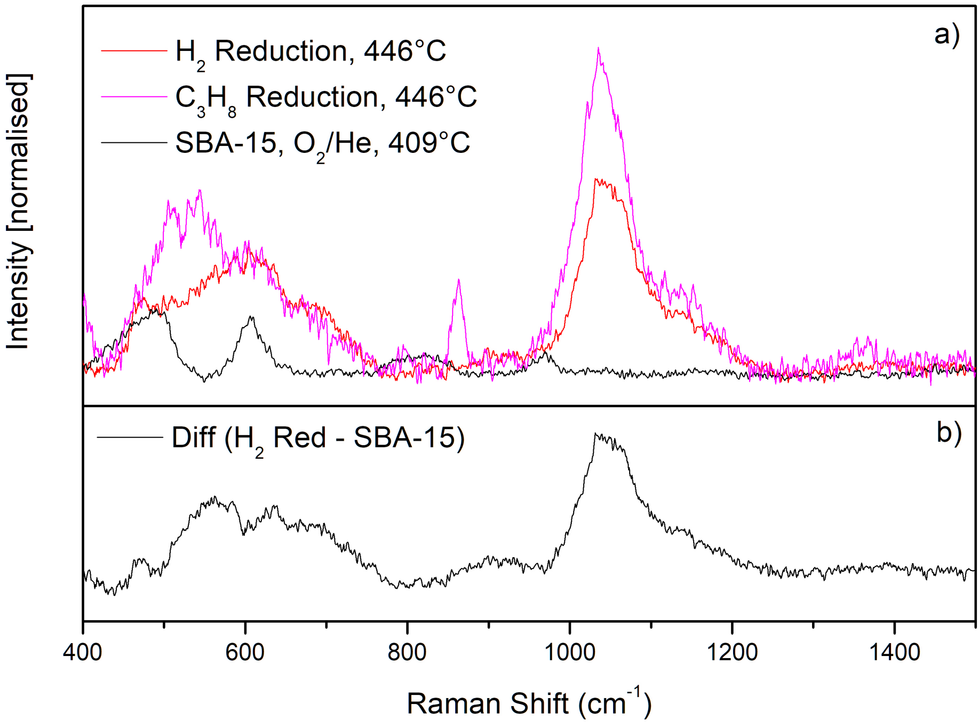

Figure 5.26: a) *In situ* 256.7 nm Raman spectra of the hydrogen and propane reduced VO_x/SBA-15 sample in comparison to SBA-15 (at oxidative conditions). b) Difference spectrum of the hydrogen reduced state and the support SBA-15.

Various peaks are clearly affected under these reductive conditions including V-O-V vibrations and the overall intensity of the vanadyl region. Figure 5.26 compares the hydrogen and propane reduced spectra with blank SBA-15. The hydrogen reduced sample shows a higher degree of reduction than the propane reduced sample, i.e., V-O-V bands and the vanadyl region are more affected under hydrogen. It is proposed that Raman features of the silica support become more prominent in reduced samples, as the shape between 400 and 600 cm^{-1} contains a feature describable as a dent. 491 cm^{-1} was taken as a reference point in order to consider the maximum spectral contribution of the support. The difference spectrum indicates the presence of at least four different components between 400 and 800 cm^{-1}. The narrow feature at 461 cm^{-1} is attributed to V-O-Si bending. Waleska et al. [30] suggested that features at 545 and 692 cm^{-1} contain possible V-O-Si components, but the analysis does not allow a clear identification.

Wu et al. [117] previously reported the redox behaviour for a VO_x/silica sample.The experiment was performed at room temperature after a preliminary hydrogen reduction at different temperatures. Changes are observed around the vanadyl region, whereas peaks at 1032 and 1041 cm^{-1} are attributed to different kinds of V=O species. The results are not directly comparable. However, the shape of the vanadyl also seems to have been affected in the experiments shown here.

5.7.1 Temperature-dependent structural dynamics

The spectroscopic temperature study of dehydrated vanadium oxide samples (see section 5.5) revealed that corresponding Raman spectra change in dependency of the temperature. With rising temperature, V=O and V-O-V peaks increased and V-O-Si bonds declined. Temperature-dependent DRIFT spectroscopy pointed to the presence of V-OH vibrations until <152°C. The feature was already detected at room temperature in oxidative conditions. The presence of propane probably had no affect on its existence. Hence, it is assumed that the observed changes are not only attributed to a Raman-related temperature effect, but also to a structural dynamic.

At a density of 0.6 VO_x atoms per nm^2, the silica surface is covered by 21% considering a monolayer at 2.9 V/nm^2. If two fully dehydrated monomeric species, located in the near vicinity, agglomerate to a dimeric species, the amount of V-O-Si bonds would decrease by 33%. Three dimeric species form two trimeric chains, which changes the amount of V-O-Si from 12 to 10, resulting in a decline of only 16%. The arrangements would also result in a loss of total oxygen (from 21 to 20). In the presence of hydroxylated bonds, the V=O intensity may be affected in its perpendicular orientation resulting in a decreased Raman cross section at low temperatures. Hence, the intensity of V=O would rise with increasing temperature. The assignment of features at 548 and 695 cm^{-1} has already been intended by Waleska et al. [115]. They provided a literature overview of reported positions for V-O-V stretching vibrations. However, the observed spectral features could not be unambiguous assigned. Several possibilities are mentioned like a 2- and 3 fold-coordinated oxygen atom or symmetrical and asymmetrical stretching modes. If the features would correspond to symmetrical and asymmetrical vibrations, both features would show the same behaviour (decline/increase), but possible additional components, like V-O-Si, make the analysis more complex. It is expected that theoretical calculations of resonance Raman spectra may be

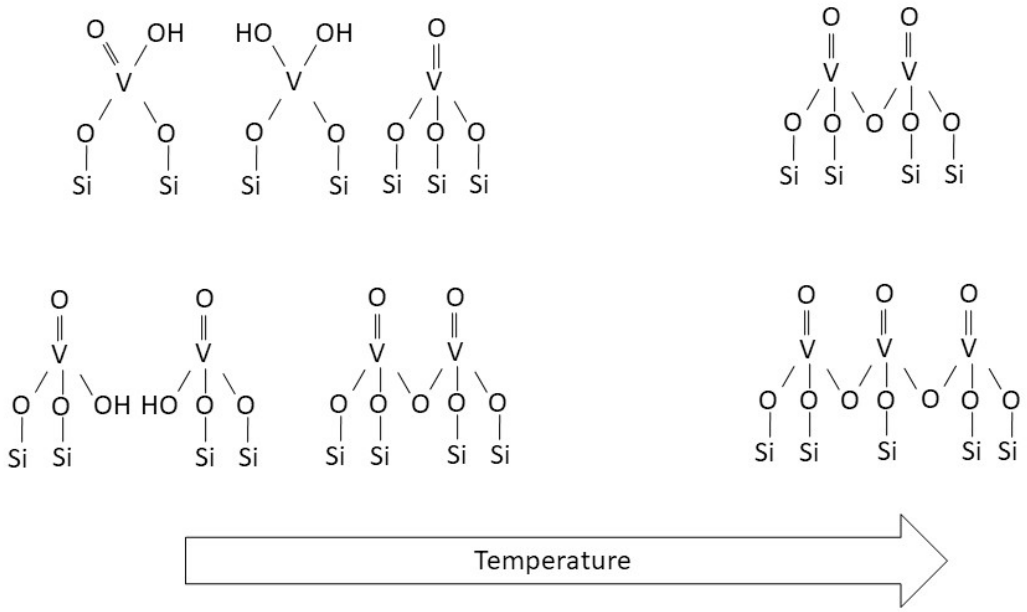

Figure 5.27: Proposed temperature-dependent structural dynamics for silica supported vanadium oxide.

able to elucidate these spectral components in the future.[113] So far, a model is proposed as shown in figure 5.27 based on the assumption that some vanadium oxide species may not be fully-dehydrated at low temperatures. Moreover, an increasing oligomerisation is considered.

5.7.2 Degree of reduction

Based on the experimental results obtained in this work and theoretical calculations reported in the literature [39, 40, 42], a description of the degree of reduction under propane reductive/oxidative and hydrogen reductive conditions is attempted in the following.

Under oxidative conditions, the presence of a mixture of oligomeric, dimeric, and monomeric vanadium oxide species is reasonable. The average amount of V-O-V of around 2 at low loadings indicates the dominance of dimeric, trimeric, and low-oligomeric species. According to Rozanska et al. [40], the activation of propane starts with hydrogen abstraction by a vanadyl group. Propene is formed by a second hydrogen abstraction, either at the same site or at a another one. The final reduced state is described either as V^{III} (d^2), V^{IV} (d^1) or V^{III} (d^2) H_2O. Experimental results do not allow a single monomer or dimer species to be observed. Although, DRIFT spectroscopy could not clearly verify the existence of VO-H bonds under *operando* conditions, HO-V^{IV} (d^1) species are not excluded here. As reoxidation is occurring fast during the reaction, the concentrations of reduced sites may be too low to be observable. *Operando* UV-vis provided the spectroscopic evidence of vanadium with its oxidation state 3+/4+. In the *operando* Raman experiments, the spectral changes can be attributed to a weakly reduced or fully oxidised state, where predominantly V=O sites participate in the reaction cycle. For higher oligomerised species, lower energy barriers are predicted [40]. As theoretically suggested [113, 139], particular vanadium oxide structures are probed depending on the excitation wavelength. Consequently, 515 nm Raman spectra include long-chain or large 2D oligomers. It may be assumed that vanadyl vibrations, detected via 515 nm, are affected first, as observed in the *operando* experiment and further confirmed in the 515 nm interference experiment. The intensity decrease, however, can also be related to a self-absorption effect due the reduction of vanadium to 3+/4+ according to UV-vis spectroscopy. The spectroscopic trends (vanadyl decline + self-absorption) continue for 385 nm Raman spectroscopy, as could be observed for the additional propane-reduction experiment performed with an excitation wavelength of 385 nm (included in the annex). It appears that the vanadyl of vanadium oxide species, detected via 256.7 nm Raman spectroscopy, is still present under strongly reducing conditions in the presence of propane or hydrogen. The spectrum may contain a higher percentage of features attributed to low-oligomeric species like monomers, dimers, and trimers.[113]

With increasing extent of reduction, also V-O-V bonds are affected. These can be especially probed via UV-vis and 256.7 nm Raman spectroscopy. Rozanska et al. [40] proposed several competing pathways, containing an hydrogen atom attached to a bridging oxygen atom. These include the formation of isopropanol or isopropoxide species via a rebounding of the propyl radical, and isomerisation processes. It is further suggested that vanadium oxide is in a strongly reduced state, when SiO-H formations are detected in 256.7 nm Raman spectra, as observable during C_3H_8/He exposure. In order to yield these alternative intermediates with a hydrogen atom attached to oxygen in V-O-Si sites, 11-33 kJ/mol higher energies are necessary than for the intermediate with H attached to V-O-V [40]. The difference in the Raman spectra obtained under hydrogen and propane reducing conditions may be attributed to the respective reducing agent. It might be mentioned that in contrast to hydrogen, the propyl radical can react at a different site, abstracting its hydrogen at a second site. Finally, Rozanska et al. [42] mentioned the formation of a dimer with two V^{III} (d^2) sites to be unlikely. This may represent a fully reduced vanadium state. From a spectroscopic point of view, the vanadyl signal would completely vanish, which has been the case under C_3H_8/He exposure for 515 and 385 nm Raman spectroscopy, predominantly containing a higher percentage of oligomeric species. Interestingly, the decrease of the vanadyl in 256.7 nm Raman spectroscopy is accompanied by a similar decrease of the V-O-Si (out of phase) vibration. This might be an indicator for the absence of a dimer with two V^{III} (d^2) sites. Instead, the spectroscopic information points to the preference of a dimer with one hydrogen atom at the vanadyl and another one at V-O-Si or V-O-V, probably stabilising active V=O sites. V^{III} (d^2) H_2O species might be expected in the O-H region using DRIFT spectroscopy. However, these cannot be clearly identified here. To sum up, V=O sites are highly active, especially of oligomeric vanadium oxide species. With increasing reduction, also V-O-V and V-O-Si sites participate in the abstraction of hydrogen, which results in a lower oligomerisation degree (breakage of V-O-V). Hence, active oxygen sites may, in principal, follow the order: V=O > V-O-V > V-O-Si. Figure 5.28 visualises the made conclusions.

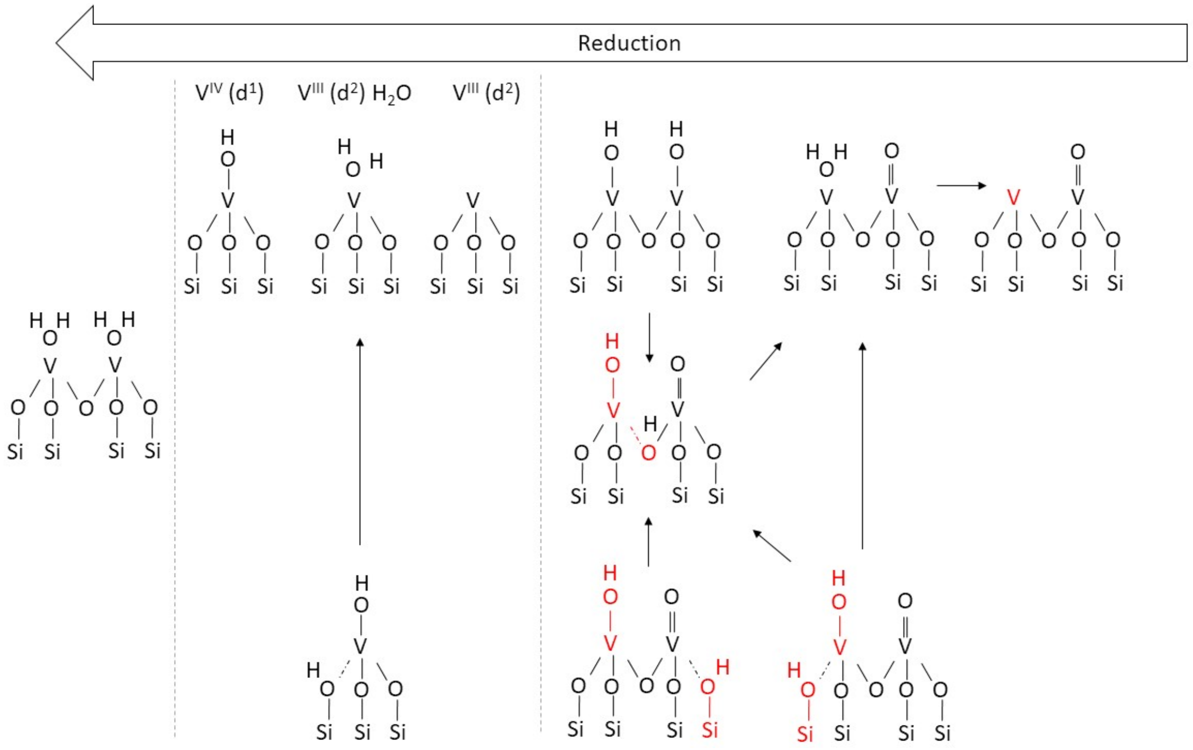

Figure 5.28: Proposed mechanisms for an increasing extent of reduction of silica supported vanadium oxide species. Thin arrows indicate possible isomerisation processes. Red labeled features could be directly verified in this work.

5.7.3 Dependency of structural dynamics on the substrate

Supported vanadium oxide catalysts are known for their unique catalytic properties in ODH reactions. The activation of the C-H bond by the catalyst is considered to be the crucial step and hence, its understanding is of fundamental interest. Therefore, the ODH of alcohols may serve as a prototype reaction, which occurs at low temperatures with high selectivities. As previously discussed, the reaction mechanism of ODH reactions follows a Mars–van Krevelen (MvK) mechanism involving two steps, the reduction of the catalyst by the substrate and a subsequent reoxidation of the catalyst with gas phase oxygen. In 2018, Waleska et al. [30] reported the structural dynamics of a silica supported vanadium oxide catalyst in the ODH with ethanol. Due to the similar *operando* approach as applied in this work, results are directly comparable. It also raises the question, what kind of information *operando* Raman data contain.

Operando UV-vis and UV-Raman spectra show considerable differences to the ODH with ethanol, which indicate a strong dependence of the vanadium oxide structure on the substrate. Major structural arrangements are observed during the reaction. With the breakage of the weak O-H bond, ethoxy species are formed on the surface. Several Raman signals at 657, 922, 1056 and 1095 cm^{-1} indicate the chemisorption of ethoxy species. In comparison to CH_2 and CH_3 stretching vibrations, detected around 2941 cm^{-1}, those signals experience a resonance enhancement effect with excitation in the UV. The gas phase contribution is considered to be negligible at low ethanol concentrations (1% EtOH). The C-C stretching mode at 880 cm^{-1} of liquid ethanol is blue shifted by 42 cm^{-1}, pointing the formation of a V-O-C(-C) bond. The Raman shift value is correlated to the respective bond length, mentioning that the C-C stretch of a gas phase acetaldehyde molecule is located at 1109 cm^{-1} together with its O=C-C mode at 512 cm^{-1}. After a leaching of VO_x units, V-O-V and V-O-Si linkages of remaining (stable) vanadium oxide species are consumed. *Operando* UV-vis data confirm the reduction of the oligomerisation degree, indicating that monomeric and short-chain oligomeric vanadium oxide species are highly active. Moreover, the vanadyl is red shifted, which may refer to the presence of short-oligomeric species. Subsequent C-H activation proceeds on the basis of the adsorbate attached to V, and may occur via the terminal oxygen. The results give a direct evidence of the proposed mechanism by Kilos et al. [83] and Beck et al. [38].

In contrast, propane ODH starts with the physisorption of the propane molecule onto the surface, followed by a subsequent C-H activation. The absence of spectral features of physisorbed propane molecules in the Raman spectra confirms the weak interaction. Furthermore, the intermediate C_3 structure is heavily discussed. Alkoxide and alcohol formation are possible options. The *operando* Raman results did not show any severe structural dynamics. Hence, this can be taken as a direct evidence for the first C-H activation being rate-limiting. Thus, the observed monomeric and oligomeric vanadium oxide species after dehydration are proposed to resemble the active structure. During reduction, possible HO-V (IV) sites may be present at the surface. However, their concentration is probably too low for detection. Moreover, a higher oligomerisation degree is expected to be present before starting the ODH of propane in comparison to ethanol ODH because higher temperatures are applied.

Several attempts have been made in order to obtain an understanding of the active structure in alkane ODH. Although the *in situ/operando* approach has gained immense interest, there are certain challenges to overcome. In the literature, *in situ* experiments have been combined, e.g., with a catalytic testing in a conventional reactor.

In situ UV-vis has been used in order to determine the extent of vanadium reduction. The variation of vanadium oxide loading gives information on oligomeric/isolated structures, and its respective behaviour under steady state or reductive conditions. The dynamic behaviour of supported vanadium oxide catalysts has previously been studied in the selective oxidation of ethane.[124] During steady state conditions, no appreciable reduction was detected for the supported vanadium on an inactive support, as determined in the *in situ* UV-vis experiment. The relative extent of reduction was calculated from the total area of the LMCT bands of V(V). No edge energy shift was observed, even under ethane reductive conditions. The *in situ* Raman experiments also exhibited no notable change under ethane oxidation conditions. The excitation wavelength was specified as 515 nm (Ar^+ line). A selection of reported *in situ/operando* methods in alkane ODH is given in table 5.9.

Table 5.9: Selection of reported *in situ/operando* methods of vanadium oxide supported on inactive supports in alkane ODH. This table is not exhaustive.

Support	Substrate	*In situ/operando* method	Reference
Al_2O_3, SiO_2	ethane	*in situ* UV-vis, Raman	[124]
Al_2O_3	ethane	*in situ* UV-vis, Raman	[140]
Al_2O_3	propane	UV-vis, Raman; online GC	[141]
Al_2O_3	propane	*in situ* UV-vis	[125]
SiO_2, MCM-41, MCM-48	propane	UV-vis; online MS	[43]
SBA-15, Al_2O_3, MCM-48	propane	EPR, UV-vis; online-GC	[142]
SiO_2	hydrogen	*in situ* multiwavelength Raman	[117]

The presented multiwavelength approach included three different wavelengths and exploited the resonance Raman effect in a targeted manner. Nevertheless, in propane ODH, only minor structural arrangements were observed under steady state conditions. This raises two questions:

- Was the catalyst active?
- Was the active species detectable (active species versus spectator)?

The simultaneous catalytic measurement via the GC gives evidence for the activity of the catalyst. The multiwavelength approach was designed in order to probe highly-oligomerised, low-oligomerised, and dimeric/monomeric structures, thus covering the whole range of available vanadium oxide species. Although the presence of spectator species cannot be excluded, the overall results of the *in situ/operando* experiments indicate that the reaction occurred over the catalyst during the *operando* experiment. It might be emphasised that major structural changes are observable in the absence of molecular oxygen. Hence, in propane ODH the first C-H activation may constitute the rate-determining step. The catalyst is mainly in a fully-oxidised state due to the fast reoxidation via molecular oxygen. It is proposed that the vanadyl site contains the active oxygen. At low temperature and low conversion, the second H-abstraction may probably occur on another site. Hence, the propyl radical is converted to propene, while a second V-OH site is left on the surface. With increasing conversion, the amount of participating V=O sites increases. Pathways involving HO-V(d^1) groups for the second H abstraction become also possible, either by the direct formation of propene resulting in V^{III} H_2O or by a rebound mechanism towards an intermediate isopropanol species. V-O-V sites may be able to abstract the hydrogen atom from possible isopropanol or isopropoxide species. The latter species occurs via a rebinding mechanism of the propyl radical to a V=O group. Bridging oxygen sites may also participate in isomerisation processes of hydrogen atoms initially attached as two HO-V(d^1) sites, which may result in the formation and final desorption of water.[40]

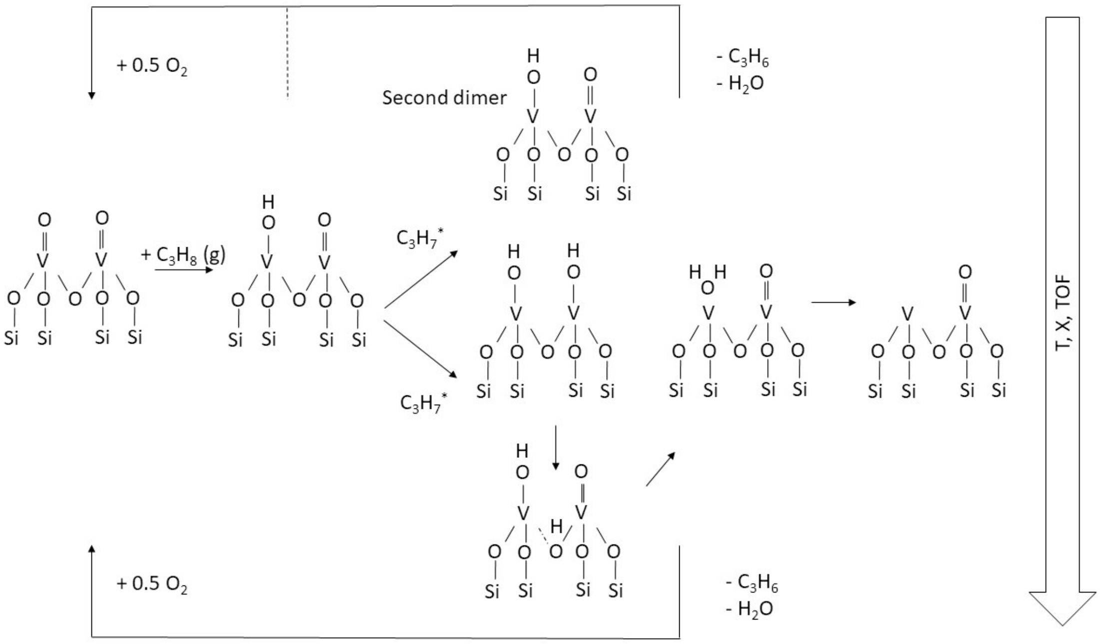

Figure 5.29: Proposed reaction mechanism for propane ODH over a silica supported vanadium oxide catalyst based on the analysis of the *operando* spectroscopic data.

6 Use of carbon dioxide for propane ODH with silica supported vanadium oxide

Recently, carbon dioxide has been utilised as a soft oxidant in high-temperature reactions, such as the dehydrogenation of alkanes.[21, 23] Molecular oxygen effectively suppresses coke formation, which is a major obstacle to the application of thermal dehydrogenation. However, low propene selectivites are obtained with O_2.[10] The use of CO_2 as a mild oxidant is promising as coke formation is alleviated as well as propene selectivity is significantly enhanced. Nevertheless, the role of CO_2 is still not completely understood.

This chapter presents an *operando* approach for a silica supported vanadium oxide catalyst in the ODH of propane with CO_2 as an oxidising agent. First, the catalytic performance is studied in the presence and absence of CO_2. *Operando* Raman experiments using 256.7 and 385 nm excitation wavelengths applied at different temperatures provided a first evaluation of this approach. These allowed the design of a complete *operando* study, comparable to the experimental and theoretical results of Ascoop et al. [35] on a WO_x–VO_x/SiO_2 catalyst in the dehydrogenation of propane with CO_2. Hence, the pretreatment procedure is extended by the reduction of hydrogen and the reoxidation via CO_2. It is expected to generate only active and selective surface oxygen via the reoxidation with CO_2. Ascoop et al. [35] used a partially reduced dimer for their theoretical modeling. Comparable *operando* results are also presented for propane dehydrogenation and the reverse water gas shift reaction. Finally, the results are discussed, considering selectivity and the choice of the oxidising agent.

6.1 Catalytic activity

Figure 6.1 shows the catalytic results of the 0.6 VO_x/SBA-15 catalyst in the propane ODH with CO_2 in comparison to thermal DH. The reaction feed consisted of 12.5% C_3H_8/ 12.5% CO_2/ 75% He and 12.5% C_3H_8/ 87.5% He, respectively, after dehydration in He. For the ODH with CO_2, the background activity of the Linkam cell was measured.

The catalyst shows catalytic activity between 450 and 600°C with a maximum propane conversion of around 3%. The catalyst turned grey during the reaction, which is either related to the reduction of the catalyst, as observable in the hydrogen-reduction experiment above, or to coke deposition. The carbon balance accounts for <3.5 % in DH and <1 % in ODH. Selectivities of higher than 93% are obtained in both experiment. Besides propylene and H_2, ethane, ethylene, and methane were detected during DH. Hence, the significant amounts of CO indicate the participation of CO_2 in the overall ODH reaction. The amount of converted propane exceeds the amount of converted CO_2. This may indicate either that propane dehydrogenation occurs in parallel or a two-step pathway with the RWGS reaction takes place. Moreover, lower propane conversions are noted in the presence of CO_2 than in its absence. It is possible that the temperature in the reactor has been 50°C less in the presence of CO_2 due to the difference in thermal conductivity (CO_2: 0.0164 W/(mK), He: 0.150 W/(mK)). CO_2 may have also prevented a temperature runaway in the catalyst bed [21, 143].

The detection of hydrogen provides a further analysis of possible reaction pathways. A summary of relevant reactivity data is given in table 6.1. The propene to hydrogen ratio of 1.1 and 1.2 in DH points to an adequate measurement of H_2 via the GC. In the ODH with CO_2, the amount of propene is higher than that of H_2 and CO, respectively. In the case that the overall mechanism follows a two-step pathway, propane is converted to propylene and hydrogen (ratio of 1:1). In a second step, H_2 reacts to water via the RWGS reaction. Hence, the amount of remaining H_2 (= detected H_2) plus the amount of detected CO may then be equal to the amount of C_3H_6, which is the case here. The analysis is also valid for the ODH with CO_2, which is accompanied by the direct dehydrogenation.

Takahara et al. [65] reported propene yields of >20 % for a silica supported vanadium oxide catalyst (loading: 5 wt%, VO_x density: 1.7 V/nm^2) in propane dehydrogenation with CO_2 (W/F = 45 g-cat/(mmol-C_3H_8/min)) at 550°C. The reported values with CO_2 were higher than those in the absence of CO_2. In order to calculate the yield of the catalyst, which is defined as the product of propane conversion and propene selectivity, the activity of the Linkam cell was abstracted here. At a reaction temperature of 547°C, a propene yield of 1.2 ± 0.1 % was obtained in the presence of CO_2. In the ODH with O_2, a similar value is determined at a temperature of 502°C (1.8 ± 0.1 %). The corresponding conversion of 2.43 ± 0.08% and selectivity of 73.2 ± 1.8% was taken from the experiment performed with a total flow of 40 ml$_n$/min (see table 5.1). The high discrepancy to >20 % is attributed to their reported W/F value, which is around two hundred times higher.

For the *operando* experiments, reaction temperatures of 547 and 593°C were chosen. Corresponding surface temperatures were calculated to be 446 and 483°C, respectively. These temperatures might represent the limit of the CaF_2 window as breakage has already been occurred at these temperatures. Hence, *operando* experiments at even higher temperatures would be risky, concerning their realisation. The question, if the catalyst is truly “at work” during the spectroscopic measurement, is thus more critical here. At a reaction temperature of 456 and 502°C, e.g, the propane conversion accounts for 0.24 ± 0.01 % and 0.55 ± 0.04 %, respectively.

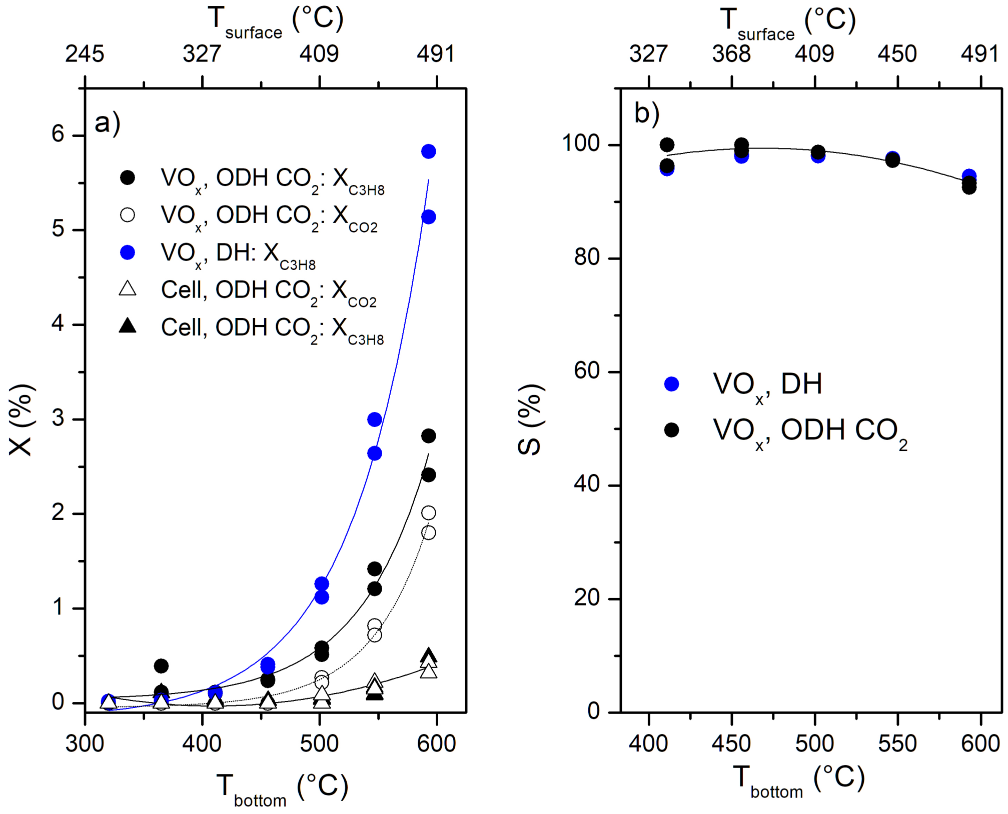

Figure 6.1: Catalytic performance of a 0.6 VO_x/SBA-15 catalyst in the dehydrogenation with and without the assistance of CO_2. a) Propane and CO_2 conversions as a function of temperature. b) Selectivity towards propene as a function of temperature. Gas composition: 12.5% C_3H_8/ 12.5% CO_2/ 75% He and 12.5% C_3H_8/ 87.5% He, respectively; total flow: 40 ml$_n$/min. For the ODH with CO_2, the activity of the empty cell was determined. Lines are to guide the eye.

Table 6.1: Catalytic performance of a 0.6 VO_x/SBA-15 catalyst in the dehydrogenation with and without the assistance of CO_2. The respective molar ratio of C_3H_6, CO, and H_2 is shown for a reaction temperature of 547 and 593°C.

	$\frac{n(C_3H_6)}{n(CO)}$	$\frac{n(C_3H_6)}{n(H_2)}$	$\frac{n(C_3H_6)}{n(H_2)+n(CO)}$
DH, 547°C	x	1.2 ± 0.0	x
DH, 593°C	x	1.1 ± 0.0	x
ODH CO_2, 547°C	1.8 ± 0.0	2.2 ± 0.6	1.0 ± 0.1
ODH CO_2, 593°C	1.4 ± 0.0	1.7 ± 0.0	0.8 ± 0.0

6.2 *Operando* results under reaction conditions

The Raman results obtained with an excitation wavelength of 256.7 nm are depicted in figure 6.2. After dehydration in Helium at 502°C, Raman measurements were performed in He at 593°C, in the presence of CO_2 (30% CO_2 / 70% He, total flow: 45 ml_n/min; after 20 min), and subsequently under reaction conditions (11% C_3H_8/ 15% CO_2 / 74% He, total flow: 47 ml_n/min; after 20 min). The surface temperature was calculated to be 483°C. The catalytic data revealed that the activity of the catalyst dropped with time, probably due to catalyst deactivation. The comparison of the Raman spectra in pure He and in a mixture with CO_2 implies a possible oxygen loss during the Helium pretreatment. Moreover, CO_2 features are detected at 1264, 1285, 1388, and 1409 cm^{-1}. The symmetric stretching mode of CO_2 is expected at approximately 1330 cm^{-1}. The doubly degenerate bending mode is Raman forbidden, but IR-active. It appears at 667 cm^{-1}. Its overtone is expected at 1334 cm^{-1}, which is close to the fundamental of the symmetric stretching mode. As a result, a Fermi resonance occurs, and the coupling leads to a band splitting and an energy shift. Hence, two modes appear at 1285 and 1388 cm^{-1}. The remaining peaks at 1264 and 1409 cm^{-1} are attributed to their respective hot band.[144] During the reaction, the sample turned grey after several minutes in the reductive environment, leading to a decrease of the overall Raman intensity and the signal-to-noise ratio. In order to compare the peak ratios, the spectrum was normalised to the vanadyl band. As a result, the CO_2 signals increase, which may be misleading in this case. V-O-V features at around 548 cm^{-1} and 695 cm^{-1} are comparatively reduced. It may indicate a breakage of V-O-V and a reduction in oligomerisation. Features at around 2900 and 3738 cm^{-1} are attributed to gas phase propane and SiO-H vibrations, respectively. The region between 1500 and 2500 cm^{-1} is not shown here as the vanadyl overtone at 2054 cm^{-1} completely vanished. Furthermore, no carbonaceous species could be detected.

The temperature effect of gas phase CO_2 (undiluted, 40 ml_n/min, empty cell) was studied by applying temperatures between room temperature and 600°C. In the first instance, the experiment proves the detection of CO_2 gas phase signals. Furthermore, the CO_2 signature observed in the *operando* Raman spectrum corresponds to a temperature between 400 and 600°C, as expected.

Further *operando* Raman experiments were performed with 385 nm excitation. For dehydration, the sample was heated to 502°C in He for one hour. Oxidative conditions consisted of 12.5% CO_2 / 87.5% He at a total flow of 40 ml_n/min, reactive conditions of 12.5% C_3H_8 / 12.5 % CO_2 / 75 % He (data recording after 15 min). A reaction temperature of 547°C was chosen, which corresponds to a surface temperature of 446°C. After the reaction, a gas flow of 12.5% CO_2 in He was set in order to study the reoxidation behaviour of the catalyst. In this case, Raman spectra were taken in the following order

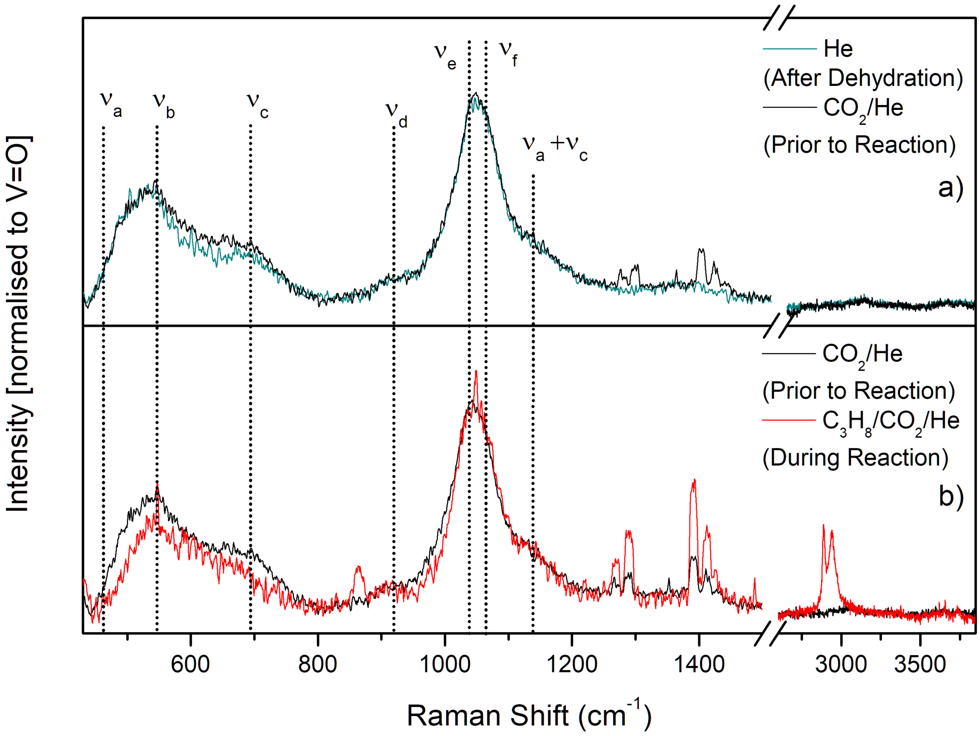

Figure 6.2: *Operando* 256.7 nm Raman spectra of the 0.6 VO_x/SBA-15 catalyst. The feed during oxidative conditions consisted of 30% CO_2 / 70% He; the feed during *operando* conditions consisted of 11% C_3H_8/ 15% CO_2 / 74% He. The surface temperature was calculated to be 483°C. a) Direct comparison of the dehydrated state with the oxidative conditions before the reaction. b) Direct comparison of the spectra obtained prior to reaction and during reaction. Spectra were normalised to V=O. Features attributed to supported vanadium oxide are marked (for assignments see section 5.2).

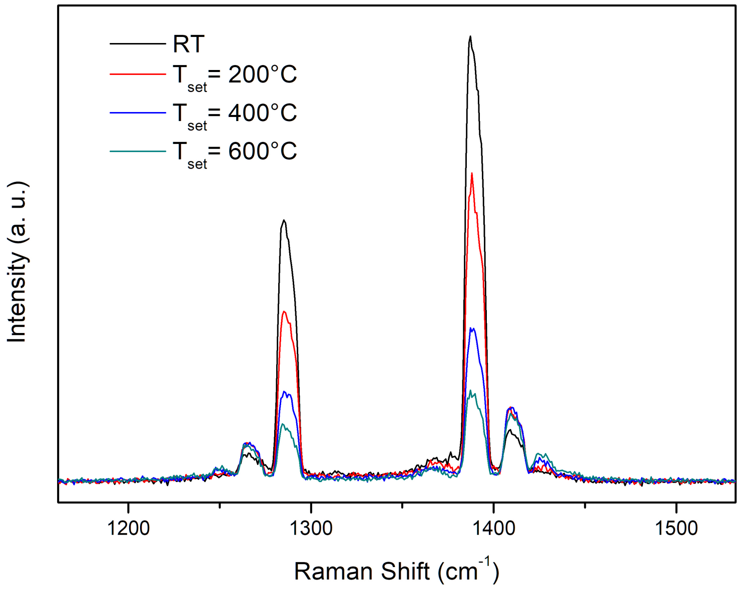

Figure 6.3: Temperature dependency of gas phase CO_2 (undiluted, 40 ml_n/min). The experiment was performed with an excitation wavelength of 256.7 nm.

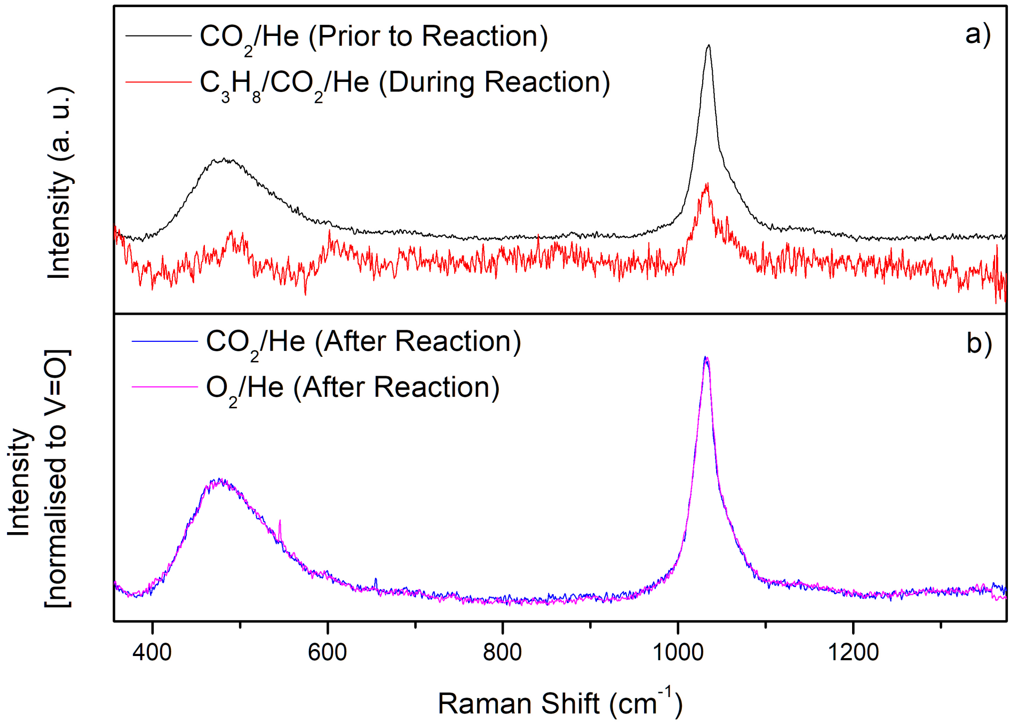

Figure 6.4: *Operando* 385 nm Raman spectra of the 0.6 VO_x/SBA-15 catalyst. The feed during oxidative conditions consisted of 12.5% CO_2 / 87.5% He or 12.5% O_2 / 87.5% He (as indicated); the feed during *operando* conditions consisted of 12.5% C_3H_8 / 12.5 % CO_2 / 75 % He. The reoxidation with CO_2 was performed after the reaction. Afterwards, CO_2 was replaced by O_2. The surface temperature was calculated to be 446°C. a) Direct comparison of the spectra prior to reaction and during reaction. Spectra were normalised to V=O. b) Direct comparison of the spectra obtained after the reaction in the presence of CO_2 and O_2. The *operando* spectrum was multiplied by a factor and plotted with an offset.

(central wavenumber): 2820 cm^{-1} (1h), 1820 cm^{-1} (30 min), and 880 cm^{-1} (30 min). Hence, the low wavenumber Raman region was recorded after 1.5 h in CO_2/He. The final gas composition consisted of 12.5% O_2/ 87.5 % He. The results are shown in figure 6.4.

The Raman spectrum during *operando* conditions decreased significantly in intensity. As normalisation may not be reasonable here, the spectrum was multiplied by a factor for comparison. Peaks at 492 and 608 cm^{-1} are most probably assignable to the support SBA-15. The vanadyl stretching mode is still present at 1032 cm^{-1}. The vibration at 1064 cm^{-1} may be attributed to the TO vibration of the silica support, although the V-O-Si interface mode is also located in this region. No CO_2 gas phase signals are observable. Consumed V-O-V bonds are apparently restored after the reaction. Although no CO is detected via the GC during the reoxidation of the catalyst, it is proposed that CO_2 is able to reoxidise reduced vanadium oxide species, based on the Raman results. In the presence of molecular oxygen, the Raman spectrum did not change.

The corresponding reactivity data is summarised in table 6.2. For the *operando* experiment at 256.7 nm, the activity data was not reproducible. It is assumed that the Linkam cell was contaminated. As will be shown in the following chapter, large amounts of CO are produced in the presence of ceria. Consequently, a certain amount of CO may be attributed to the formation of coke, and thus to propane, according to the Boudouard reaction. As a result, the calculated conversion of CO_2 according to equation 3.15 is incorrect. In contrast, the activity data for the second *operando* experiment shows comparable results to the activity study. Similarly, the amount of detected H_2 and CO equals the amount of propene.

Table 6.2: Summary of the catalytic performance of the 0.6 VO_x/SBA-15 catalyst during *operando* conditions in the 256.7 and 385 nm Raman experiment.

Experiment	$X_{C_3H_8}$ (%)	X_{CO_2} (%)	S (%)	CB (%)	$\frac{n(C_3H_6)}{n(CO)}$	$\frac{n(C_3H_6)}{n(H_2)}$	$\frac{n(C_3H_6)}{n(H_2)+n(CO)}$
256.7 nm, 593°C	1.9 ± 0.3	11.8 ± 0.6	91 ± 2	<3	0.03± 0.00	0.05± 0.01	0.02 ± 0.00
385 nm, 547°C	1.3 ± 0.3	0.9 ± 0.2	96.4 ± 0.2	<4	1.44±0.03	3.9 ± 0.5	1.05 ± 0.04

Based on the experiments, the *operando* and multiwavelength approach is evaluated in the ODH with CO_2. Although a direct comparison of results is not possible, both *operando* experiments showed a highly reduced vanadium oxide catalyst under reaction conditions. It demonstrates the sensitivity of UV Raman spectroscopy for the detection of vanadium oxide structures present under highly reductive conditions. As shown in the 515 nm interference experiment above, the vanadyl mode completely vanished under C_3H_8/He exposure. No information on the structure of vanadium oxide had been available. Moreover, as the catalyst deactivates with time, the ODH with CO_2 does not reach a “steady state”. Hence, the time when a Raman measurement is recorded might play a role here. The contribution of CO_2 during the reaction cannot be easily identified, although CO_2 showed its oxidising capability in the subsequent reoxidation procedure. While using molecular oxygen as an oxidising agent, the vanadium oxide structure is maintained. So far it may be proposed that CO_2 induces a slow reoxidation behaviour.

6.3 *Operando* results under reaction conditions with hydrogen pretreatment

The present section includes a more detailed *operando* study of the propane ODH with CO_2. The previous results served as a basis for the design of the following experiments. Moreover, in order to compare the results with the literature, a pretreatment procedure, as previously reported by Ascoop et al. [35], was included. A reaction temperature of 547°C was chosen, which corresponds to a surface temperature of 446°C.

Operando UV-vis

Nitrogen was used as an inert gas in order to obtain the desired temperature. The procedure follows, in principal, the description in the experimental part. Due to the shortness of the measurements, also UV-vis spectra under oxidative conditions with O_2 were recorded after the reaction. The results are shown in figure 6.5. Spectra prior to the reaction were taken under oxidative conditions (12.5 % O_2/ 87.5% N_2, total flow: 40 ml_n/min), under H_2 reductive conditions (7.5% H_2 in Ar) and in the presence of CO_2 (12.5 % CO_2/87.5% N_2). Reaction conditions consisted of 12.5 % C_3H_8/ 12.5 % CO_2/ 75 % N_2. After the reaction, the reoxidation behaviour was studied under CO_2 and O_2 oxidative conditions (12.5 % CO_2/ 87.5% N_2 and 12.5 % O_2/ 87.5% N_2. The surface temperature was determined to be 445°C.

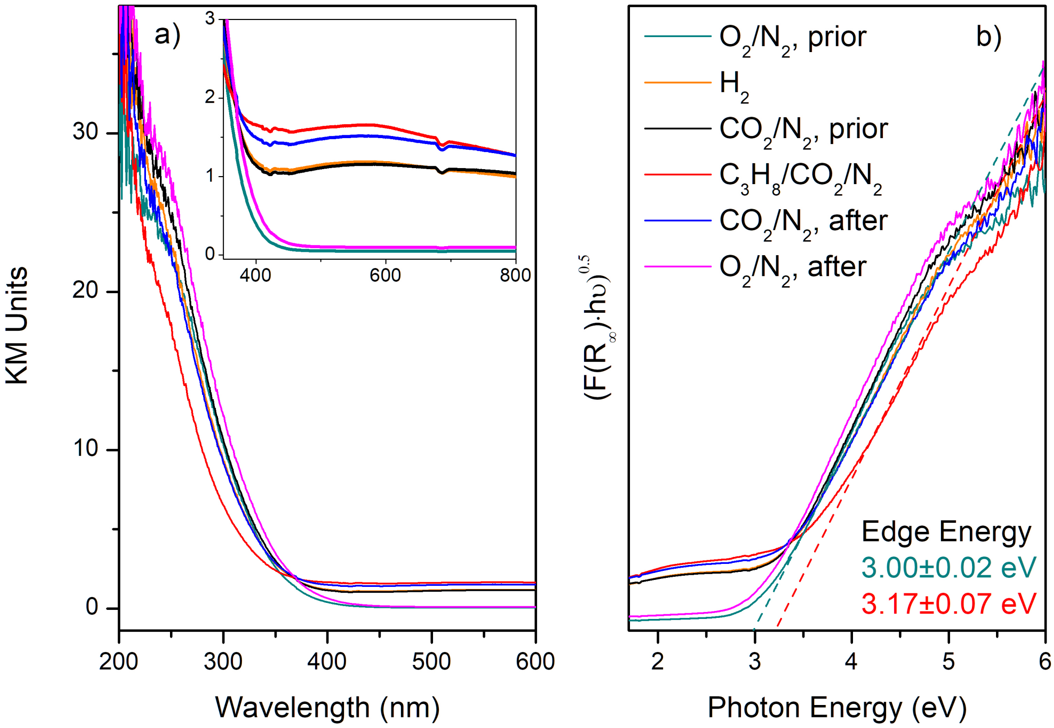

Figure 6.5: *Operando* UV-vis spectra of the 0.6 VO_x/SBA-15 catalyst. The experiment consisted of a pretreatment procedure with 7.5% H_2 in Ar. Reaction conditions consisted of 12.5 % C_3H_8/ 12.5 % CO_2/ 75 % N_2. The catalyst was reoxidised with 12.5 % CO_2/ 75 % N_2 before and after the reaction. The surface temperature was determined to be 445°C.

The conversion of propane accounted for 2.1 ± 0.2 % with a propene selectivity of 81.0 ± 0.9 %. The carbon balance value corresponds to <9 %. The burning of propane molecules may be indicated by the comparably higher amount of CO ($n(C_3H_6)/n(CO) = 0.31 \pm 0.01$). The ratio between C_3H_6 to H_2 was 1.3 ± 0.1.

During the hydrogen pretreatment, the absorption increases at wavelengths below 250 nm, and a slight red shift of the band edge energy is observable. The rise in the vis region clearly indicates the reduction of V to 4+ and/or 3+. In the presence of CO_2, the absorption rises at around 250 nm and a small blue shift is detectable. However, no noticeable decline of V(4+)/V(3+) species is observable. During reaction conditions, the prereduced catalyst is further reduced in the presence of propane. V-O-V bonds are apparently consumed and the amount of V(4+)/V(3+) species increases. The edge energy shifted from 3.00 ± 0.02 eV (after dehydration) to 3.17 ± 0.07 eV, and the average amount of V-O-V linkages decreased from approximately 2.5 to 2.0. After the reaction, the band edge energy shifts back to 2.96 ± 0.02 eV. The amount of reduced vanadium V(4+)/V(3+) decreases slightly. Finally, oxygen reoxidises the catalyst completely.

So far, the results are not consistent with the already obtained *operando* Raman experiments. First of all, it may be mentioned here that the measuring periods are not comparable to the previous Raman experiments. Each Raman spectrum takes in total 2 h, which is a multiple of a UV-vis spectrum. The time, until the measurement starts, was kept the same (20 to 30 min).

Operando UV-Raman

The *operando* 256.7 nm Raman experiments were conducted as described in 3.3.2. The procedure included dehydration (12.5% O_2/ 87.5% He), H_2 reduction (7.5% H_2 in Ar), CO_2 reoxidation (12.5% CO_2/ 87.5% He) or O_2 reoxidation (12.5% O_2/ 87.5% He), reaction conditions (12.5 % C_3H_8/ 12.5 % CO_2/ 75 % He), and regeneration (12.5% CO_2/ 87.5% He). The Raman results for the CO_2 reoxidised catalyst are illustrated in figure 6.6, providing an overview of the obtained spectra in the order from the bottom to the top.

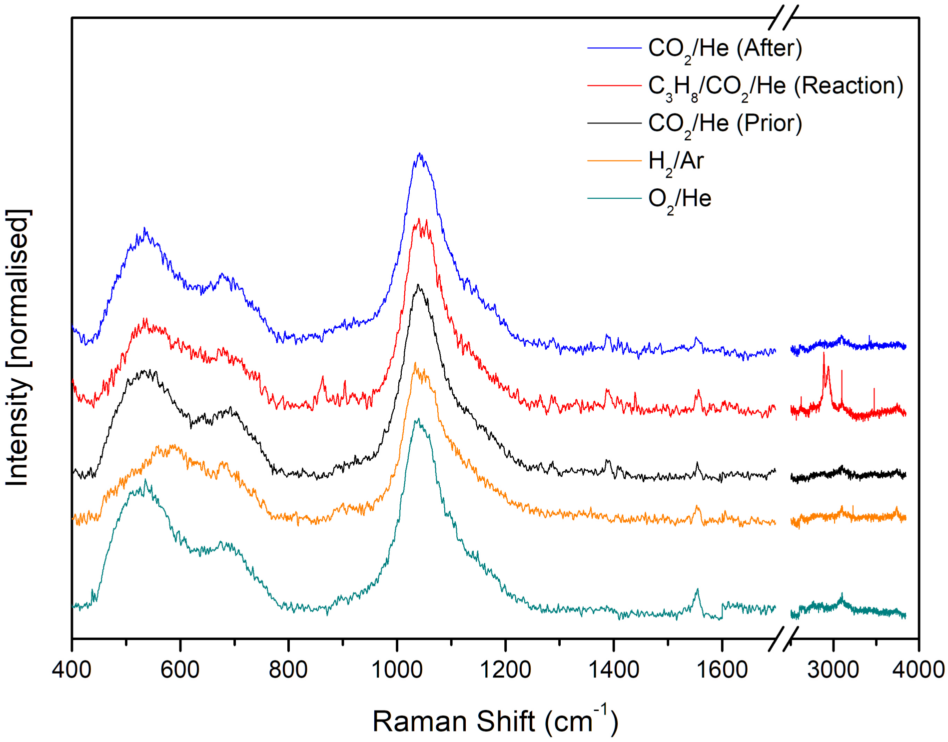

Figure 6.6: *Operando* 256.7 nm Raman spectra of the 0.6 VO_x/SBA-15 catalyst. The experiment consisted of a pretreatment procedure with 7.5% H_2 in Ar. Reaction conditions consisted of 12.5 % C_3H_8/ 12.5 % CO_2/ 75 % He. The catalyst was reoxidised with 12.5 % CO_2/ 75 % He before and after the reaction. The surface temperature was calculated to be 446°C. Spectra were normalised and plotted with an offset.

The catalytic activity is shown in table 6.3. Both experiments revealed that the catalyst deactivates with time. The conversion drops slightly, which is represented by the standard deviation. The CB values indicate a possible leak, as the CaF_2 window could not be closed tightly. Similar conversions were obtained for the O_2 and CO_2 preoxidised catalyst. In both experiments, significant amounts of CO were detected during the reaction, pointing to the successful activation of CO_2.

In the top panel of figure 6.7, the Raman results before and after each reductive environment (H_2 pretreatment and *operando* conditions) are plotted. Spectra were normalised to the V=O band, with the result that no major structural rearrangements are observable. In order to compare both reduced states, the intensity around 608 cm^{-1} was taken as a

Table 6.3: Summary of the catalytic performance of the CO_2 and O_2 preoxidised VO_x/SBA-15 catalyst during *operando* conditions at a reaction temperature of 547°C.

Experiment	$X_{C_3H_8}$ (%)	X_{CO_2} (%)	S (%)	CB (%)	$\frac{n(C_3H_6)}{n(CO)}$	$\frac{n(C_3H_6)}{n(H_2)}$	$\frac{n(C_3H_6)}{n(H_2)+n(CO)}$
ODH CO_2, CO_2 preox.	1.3 ± 0.2	1.1 ± 0.2	97.1 ± 0.2	<6	1.1 ± 0.0	2.4 ± 0.2	0.8 ± 0.0
ODH CO_2, O_2 preox.	1.3 ± 0.3	1.1 ± 0.2	97.2 ± 0.3	<7	1.1 ± 0.1	1.5±0.5	0.6 ± 0.1

reference point (see bottom panel of figure 6.7). The Raman peak probably contains a contribution of the D_2 defect band of silica.

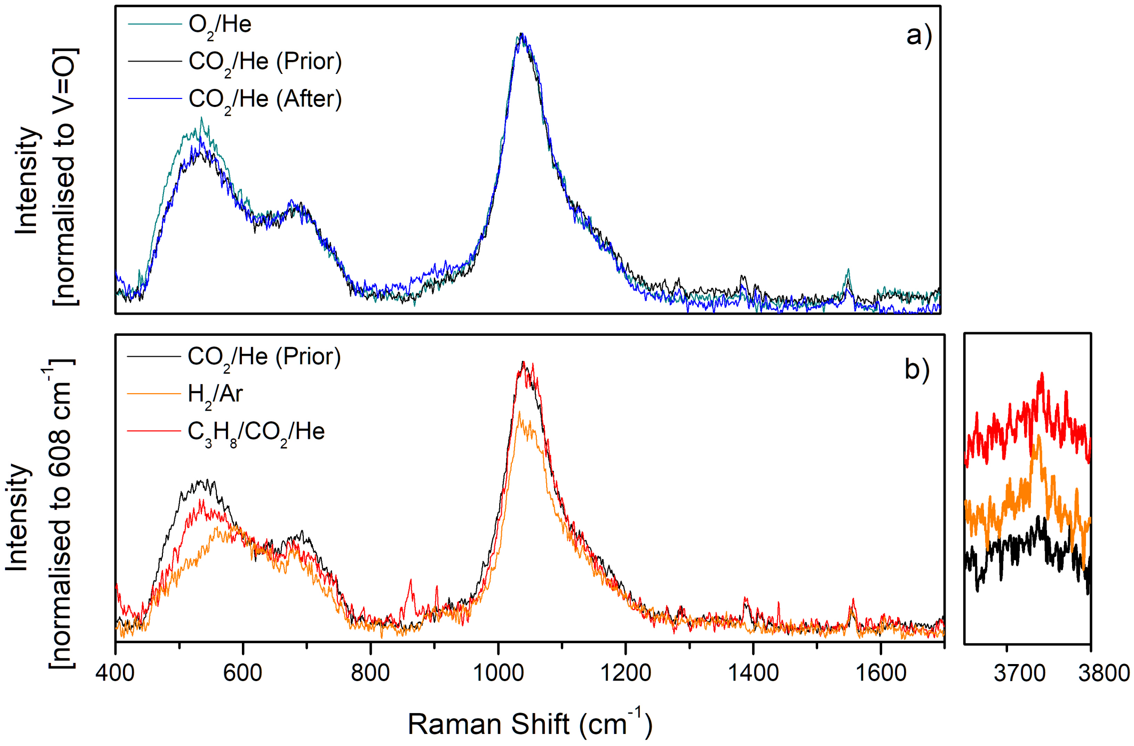

Figure 6.7: *Operando* 256.7 nm Raman spectra of the 0.6 VO_x/SBA-15 catalyst. a) Direct comparison of the dehydrated state with the conditions before and after the reaction. Spectra were normalised to V=O. b) Direct comparison of the hydrogen-reduced state with the Raman spectrum obtained under *operando* conditions. 608 cm^{-1}, the position of the D_2 band of SBA-15, was used as a reference point for normalisation.

During the hydrogen pretreatment, the catalyst reveals a highly reduced state as previously demonstrated in the H_2-reduction experiment. CO_2 gas phase features are present, but do not show the same intensities as demonstrated before, which may be attributed to a different focus position. Interestingly, the spectrum during reaction conditions represents an intermediate reduced state. The degree of reduction is further confirmed by the peak intensity of formed SiO-H bonds. It is noted here that despite the normalisation, the amount of SiO-H bonds is higher for the hydrogen-reduced state (see also the V=O peak in comparison). The degree of reduction may be attributed to the respective reducing agent, H_2 or C_3H_8, and/or to the presence of CO_2 as an oxidant. The presence of CO in the outlet gas phase suggests that CO_2 is constantly reoxidising the catalyst during the reaction, even though slowly. By comparing the *operando* Raman spectrum to an oxidised state (here “prior to reaction”), vanadium oxide species exhibit less V-O-V vibrations, indicating a lower oligomerisation degree. After the reaction, the catalyst appears to be a fully oxidised. It may be mentioned that the sample becomes already more whitish during the intermediate He flow. Carbonaceous species could not be detected during the entire experiment via Raman spectroscopy. The change in colour may be attributed to a reduction of the catalyst. However, the sensitivity towards the detection of carbon deposits by UV Raman spectroscopy is unknown.

In the corresponding Raman experiment with the O_2 preoxidised catalyst, similar observations were made. As the spectra were taken with a sapphire window, a direct comparison of Raman spectra is not possible. Despite the disturbing sapphire Raman signals in the region between 550 and 800 cm^{-1}, the spectrum obtained under *operando* conditions also clearly represents an intermediate reduced state in comparison to the H_2-reduced state.

6.4 *Operando* results for propane dehydrogenation and the reverse water gas shift reaction

Complementary Raman experiments were conducted for the DH and RWGS reaction. *Operando* conditions for DH consisted of 12.5 % C_3H_8/ 87.5 % He, for the RWGS reaction of 6.5% H_2/ 12.50% CO_2 /81% Ar, at a total flow of 40 ml_n/min. Table 6.4 summarises the respective catalytic performance. During the RWGS reaction, the amount of detected/unconverted H_2 is reduced, which goes along with a detection of CO molecules. The conversion of CO_2, calculated via the amount of detected CO, is determined to show a similar magnitude as that of converted H_2 molecules (3.3 ± 0.4 %). These are indicators that the reaction occurred over the catalyst. However, gas phase contributions cannot be excluded here. For direct dehydrogenation, a higher conversion of propane molecules was observed as in the presence of CO_2.

Table 6.4: Summary of the catalytic performance of the CO_2-preoxidised VO_x/SBA-15 catalyst in propane DH and RWGS reaction.

Experiment	$X_{C_3H_8}$ (%)	X_{CO_2} (%)	S (%)	CB (%)	$\frac{n(C_3H_6)}{n(H_2)}$
RWGS		3.5 ± 0.2			
DH	2.6 ± 0.3		95 ± 4	<8	1.2 ± 0.1

Raman spectra of the DH experiment were plotted in a similar way as for the ODH with CO_2 (see figure 6.8). By comparing the hydrogen-reduced state with the spectrum obtained under DH conditions, no major structural differences are detectable. Both conditions lead to a highly reduced vanadium oxide species. Even the amount of SiO-H species is comparable for both reducing environments. In contrast, in the presence of CO_2 an intermediate reduced structure has been observed. The extent of reduction during C_3H_8/He exposure may also be attributed to the higher conversion of propane molecules. Moreover, carbon deposits are detected at around 1600 cm^{-1}. In the subsequent reoxidation step with CO_2, the deposited coke largely disappears, which points to its reaction with CO_2 according to the Boudouard reaction. The RWGS experiment allows the comparison of the hydrogen-reduced state with and without CO_2 (see figure 6.9). Similarly to the ODH with CO_2, the catalyst shows an intermediate behaviour, which is further confirmed by SiO-H vibrations. It is proposed that CO_2 constantly reoxidises the catalyst during the RWGS reaction. These complementary

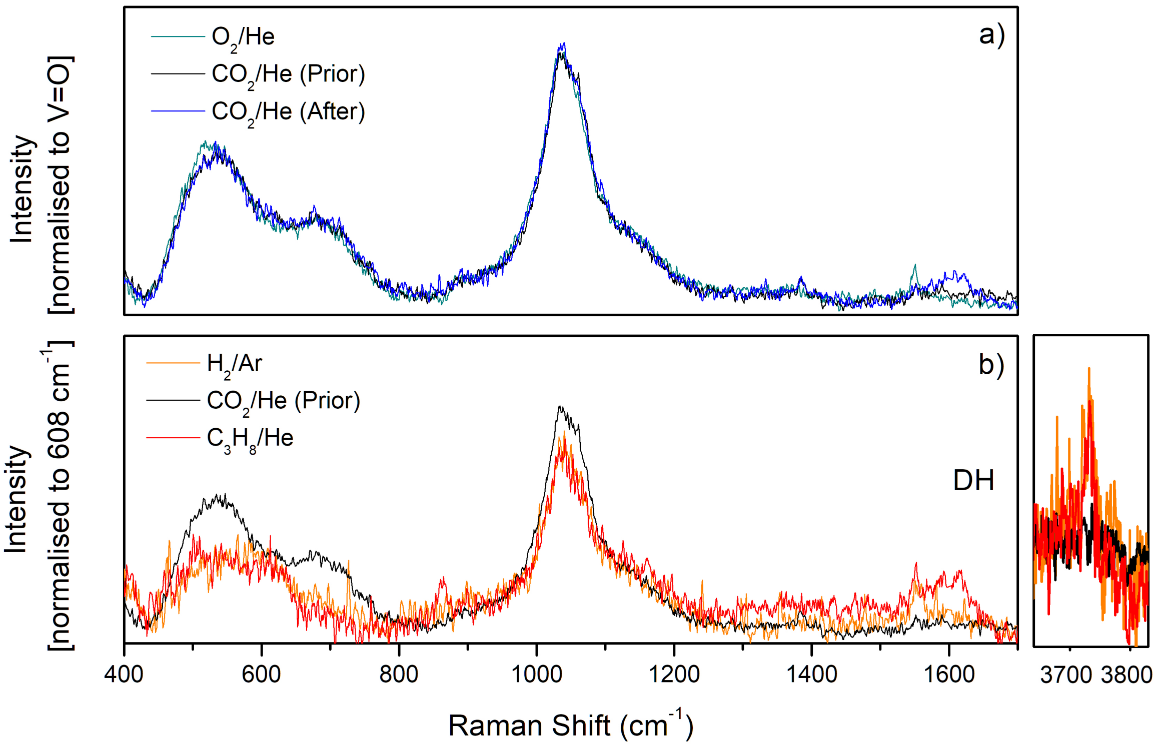

Figure 6.8: *Operando* 256.7 nm Raman spectra of the 0.6 VO_x/SBA-15 catalyst in propane DH. a) Direct comparison of the dehydrated state with the conditions before and after the reaction. Spectra were normalised to V=O. b) Direct comparison of the hydrogen-reduced state with the Raman spectrum obtained under *operando* conditions (12.5 % C_3H_8 / 87.5 % He). 608 cm^{-1}, the position of the D_2 band of SBA-15, was used as a reference point for normalisation.

experiments confirm that CO_2 participates in the overall reaction network of the ODH with CO_2, although no spectral feature allows the two reaction pathways, i.e. ODH and DH and/or RWGS, to be distinguished from each other.

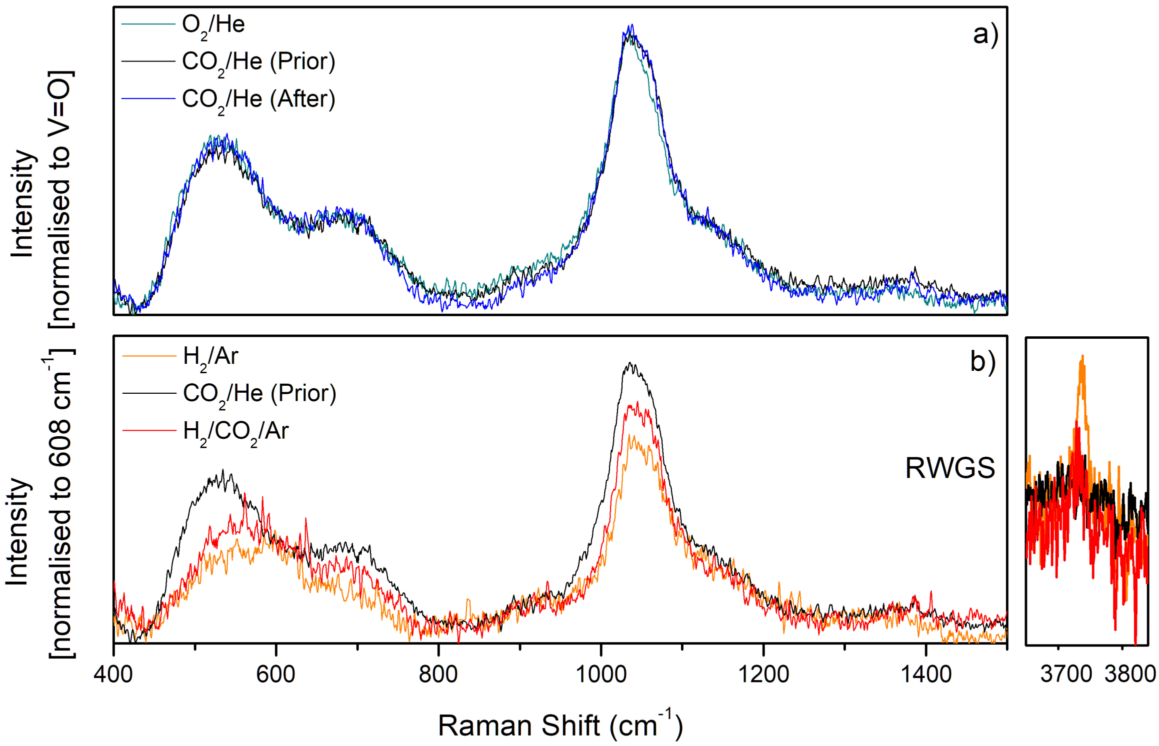

Figure 6.9: 256.7 nm Raman spectra of the VO_x/SBA-15 catalyst in the RWGS reaction. a) Direct comparison of the dehydrated state with the conditions before and after the reaction. Spectra were normalised to V=O. b) Direct comparison of the hydrogen-reduced state with the Raman spectrum obtained under *operando* conditions. 608 cm^{-1}, the position of the D_2 band of SBA-15, was used as a reference point for normalisation.

6.5 Discussion

6.5.1 Reaction mechanism

The discussion addresses the following two questions, previously raised in the literature: Is the reaction mechanism a one-step (ODH) or a two-step pathway (DH and RWGS), and what is the role of CO_2.

The catalytic data indicate that CO_2 successfully participated in the overall ODH mechanism of the VO_x/SBA-15 catalyst. During the dehydrogenation without the assistance of CO_2, no CO was detected. Hence, the observed CO production is associated with an activation of CO_2. Moreover, the amount of detected H_2 was significantly reduced, indicating that either ODH and DH occur in parallel or the mechanism follows a two step pathway with a subsequent RWGS reaction. The Raman experiment during the RWGS conditions demonstrated the catalytic activity of the present catalyst, however, the conditions were not completely comparable. Previously, Nederlof et al. [145] reported a low activity for alumina supported vanadium oxide catalysts in the RGWS reaction. CO may also be attributed to an ongoing decoking process, which was shown by the comparable DH experiment.

The *operando* experiments were performed in the following order: dehydration with O_2/He and subsequent reduction via hydrogen, reoxidation via CO_2, *operando* conditions, and reoxidation with CO_2. The individual steps will be discussed and interpreted in the following. Finally, a reaction mechanism is proposed based on the observed spectroscopic results.

The hydrogen-reduced state can be described as a highly reduced state, as specified in the previous chapter. It is proposed that it consists of a certain mixture of reduced structures with H attached to vanadyl, bridging oxygen, and interface oxygen sites (V-O-Si). The subsequent reoxidation with CO_2 might occur relatively fast in comparison to the timescale of a GC measurement. This would explain the absence of CO detection during the reoxidation. Rozanska et al. [42] reported that N_2O is not able to reoxidise V(+4) sites, which might be transferable to CO_2.

Surprisingly, the corresponding Raman results (CO_2/He, Prior to reaction) indicate that CO_2 is able to reoxidise the catalyst completely. Previously, Freund and Messmer [51] have proposed that CO_2 activation occurs via an electron transfer from the surface to CO_2, resulting in a strong Lewis acid site via its lone pair on the oxygen site. Haija et al. [146] studied the carbon dioxide adsorption on V_2O_3(0001) via temperature programmed desorption (TPD) and infrared reflection absorption spectroscopy (IRAS). Below 200 K, CO_2 adsorbed molecularly on vanadyl terminated V_2O_3(0001). Electron irradiaton led to the removal of vanadyl oxygen and subsequently to a binding of CO_2 to vanadium, forming surface CO_2^- species with the result of producing vanadyl groups and CO. Hence, it may be reasonable that reoxidation occurs over vanadium in its oxidation state 3+ for reduced supported vanadium oxide species.[35] Consequently, in order to recover V-O-V and V-O-Si bonds, adsorbed hydrogen atoms may migrate towards available vanadyl sites as part of an isomerisation process, and either desorb as H_2 or H_2O. UV-vis spectra pointed to a recovery of V-O-V bonds in the presence of CO_2, but not to a decreased vanadium reduction. Although CO_2 activation may be possible at these temperatures [146], a further requirement for the reoxidation via CO_2 may be a water-free vanadium 3+ site.[42] In contrast, for the Raman measurements, the fluidised bed mode was employed in the Linkam cell. It may be possible that reoxidation occurred for particles flowing through the hotter sample bed. Consequently, the spectroscopic information obtained via UV-vis and via Raman spectroscopy is not comparable as apparently, reoxidation did not take place at the sample surface in the Harrick cell. So far, the analysis has emphasised structures which correspond to reduced vanadium oxide species and the possible reoxidation process via CO_2. In the following, these findings are transferred to the reaction, allowing to propose a reaction mechanism based on the analysis of the *operando* spectroscopic data (see figure 6.10). Propane dehydrogenation starts with an extrinsic relaxation until a steady state is reached, as previously shown [35].

$$C_3H_8 + V^{5+}(V=O) \rightarrow C_3H_6 + H_2O + V^{3+} \tag{6.1}$$

$$C_3H_8 \overset{V^{3+}}{\rightarrow} C_3H_6 + H_2 \tag{6.2}$$

Hence, in the DH reaction a highly reduced vanadium oxide catalyst is created, which is involved in a catalytic cycle of V(5+)/V(3+). Theoretical modelling considered the bridging oxygen for the second H-abstraction from the propyl radical.[35] When CO_2 is present, CO_2 can adsorb on vanadium 3+, recovering the vanadyl bond. The comparison to a fully oxidised state indicates that the peak ratio of V=O and V-O-V features differs. During reaction conditions, the amount of V-O-V is comparatively decreased, pointing to the presence of deposited hydrogen atoms on bridging oxygen sites. *Operando* UV-vis results confirmed the resulting decrease of the oligomerisation degree. The observation of SiO-H bonds turned out to be a spectral marker for the additional consumption of interface sites. The redox mechanism of the RWGS reaction requires the (re-)adsorption of H_2 on vanadium. In the presence of reduced vanadium sites, H_2 may bind to vanadium in its oxidation state 3+, similarly to CO_2.[35] Hence, a hydrogen migration towards a V(5+) species may lead to the formation of H_2O. This mechanism requires at least a partially-reduced dimeric structure. Subsequently, CO_2 reoxidation may occur on the available vanadium 3+ site.

After the reaction, isomerisation processes may be responsible for the recovery of V-O-V and V-O-Si bonds, as observable in UV Raman spectroscopy. In CO_2/He exposure, the vanadyl is restored over a water-free vanadium (3+) sites. It might be possible that V-OH bands are residual. UV-vis spectroscopy indicates that O_2 is able to completely reoxidise a reduced catalyst. It has been proposed that O_2 is able to reoxidise V^{III}, $H_2O{\cdot}V^{III}$, as well as HO-V^{IV} species.[42]

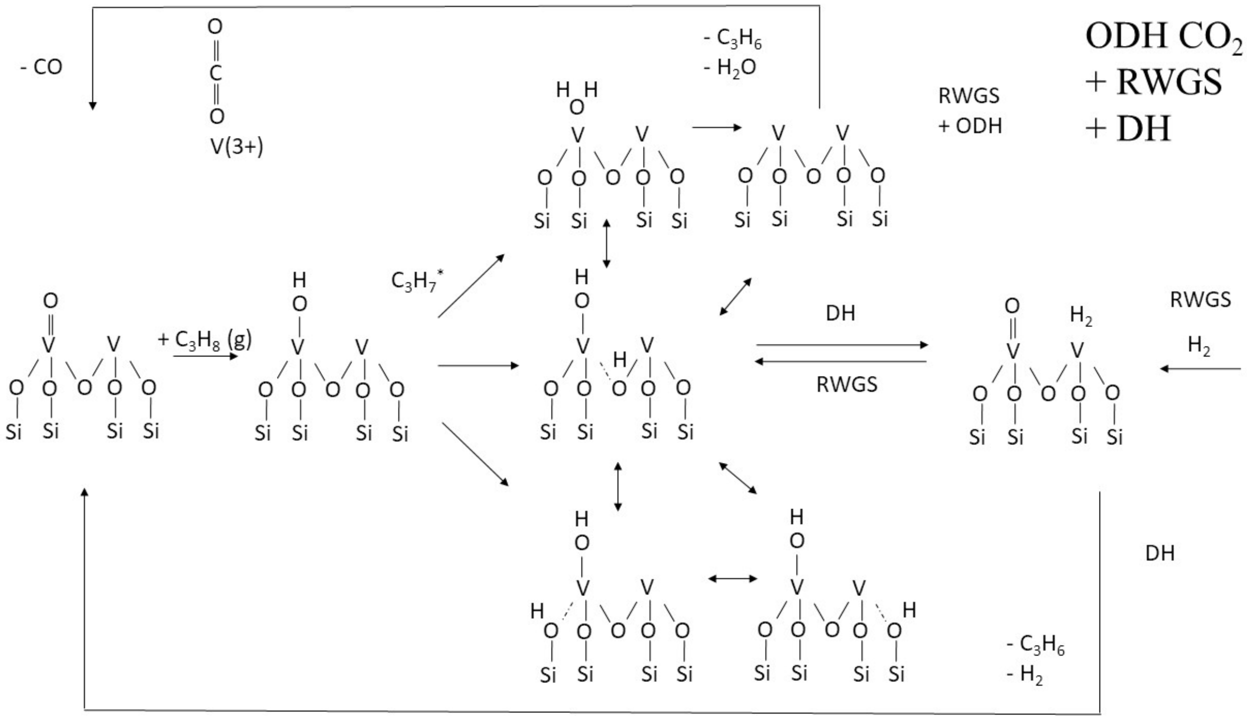

Figure 6.10: Proposed reaction mechanism for a VO_x/SBA-15 catalyst in propane ODH with CO_2 based on the analysis of the *operando* spectroscopic data presented in this work.

6.5.2 Selectivity determining factors

Catalyst selectivity in ODH reactions is a widely discussed topic in the literature [10]. Several factors have been identified, which can be related to the control of total oxidation reactions: the active oxygen (V=O, V-O-V, V-O-M) [40, 41], the degree of oligomerisation, the degree of reduction [34], and the oxidising agent [34, 42, 43, 147, 148]. Dehydrogenation reactions with and without the presence of CO_2 exhibit good selectivity in comparison to the ODH with O_2. Callahan and Grasselli [149] were the first to publish the hypothesis that active site isolation is of great importance. Only one to two oxygen atoms are necessary in an active site for selective propene formation, whereas 7-10 oxygen atoms are required for CO_x production [43]. Ovsitser et al. [43] determined that highly dispersed VO_x species are favourable for selective propene formation. *In situ* UV-vis spectroscopy verified a higher reduction degree when using N_2O as an oxidising agent. It was concluded that N_2O reoxidises reduced VO_x species more slowly than O_2. The findings complemented the previous results made by Kondratenko et al. [34]. The improving effect of N_2O was related to a spatial separation of active lattice oxygen species, which is obtained by a reduction of the surface density of active oxygen species. In 2008, Rozanska et al. [42] reported the differences between N_2O and O_2 for the reoxidation of reduced vanadium oxide sites. The reoxidation via molecular oxygen may occur via the formation of peroxovanadate oxygen species, which were considered to be highly reactive for propene oxidation. While the ODH with O_2 occurs via a V^{5+}/V^{4+} and/or a V^{5+}/V^{3+} redox couple, N_2O is only able to reoxidise the V^{3+} oxidation state. On the other hand, Dai et al. [41] have shown theoretically over a V_2O_5 surface that the formation of isopropoxide is responsible for deep oxidation reactions. Terminal oxygen sites turned out to be highly active for side reactions, whereas bridging oxygen sites were selective towards propene formation.

The presented *operando* approach has revealed, in principle, highly reduced vanadium oxide species during the DH with and without CO_2. This was accompanied with a decrease in oligomerisation. Hence, the number of active sites was reduced. One may assume that a large number of oxygen species participated in the reaction cycle, naming V=O, V-O-V and V-O-Si. In contrast, for the ODH with O_2, the catalyst was in a low reduced/fully oxidised state, which might be the reason for unselective side reactions.

7 Support effect of cerium oxide

Ceria has been known experimentally and theoretically [33, 150] for its unique redox properties due to its capability to store/release oxygen. However, a full understanding of how it interacts as an active support in the elementary steps of ODH reactions is still missing. This chapter provides an experimental *operando* study including the application of multiwavelength Raman spectroscopy to VO_x/ceria catalysts.

First, the catalytic performance of VO_x/CeO_2 and bare ceria is studied in the ODH of propane with O_2 and CO_2. Secondly, a multiwavelength Raman approach is established, allowing to obtain information on ceria bulk, surface and vanadium oxide-related features, similar to Wu et al. [151], but with *operando* capabilities. The benefits of (resonance) Raman enhancement effects are subsequently explored under *operando* conditions for EtOH ODH, as recently demonstrated for a silica supported vanadium oxide catalyst [30]. The experimental results give a direct evidence for the active support participation in ODH reactions.

7.1 Catalytic activity of VO_x/CeO_2 for propane ODH with O_2 and CO_2

Figure 7.1 shows the catalytic performance of 1.2 VO_x/CeO_2, 0.6 VO_x/CeO_2, and bare ceria (70 mg, particle sizes: 200 - 300 μm). The gas composition consisted of 14% C_3H_8/ 13% O_2/ 73% He at a total flow of 37 ml_n/min. The reaction was performed in a fluidised bed mode. CeO_2 shows high activity already at low temperatures. At temperatures above 350°C, molecular oxygen is completely consumed, which is accompanied with a poor selectivity towards C_3H_6. Carbon dioxide constitutes the main product indicating the overoxidation of propane and/or propylene. The vanadium oxide impregnation leads to a decrease of converted propane molecules and an increase in selectivity at temperatures below 400°C. For the 1.2 VO_x/CeO_2 catalyst, a maximum selectivity of 29.1 ± 0.2 % is obtained at 320°C ($X = 9 \pm 1$ %). As shown above, the silica supported vanadium oxide catalyst exhibited hardly any conversion at this temperature. The results indicate that reactive/unselective oxygen species are covered with vanadium oxide species, which, in turn, limit the activity of the ceria support. Dinse et al. [44] previously reported high activity of ceria in propane ODH. Likewise, the activity of bare ceria exceeded the loaded sample. CeO_2 is an oxidation catalyst itself, and its catalytic contribution cannot be neglected in comparison to other (active/inactive) supports. Dinse et al. studied the catalytic behaviour of a 1.5 VO_x/CeO_2 catalyst at temperatures between 350 and 400°C. Even at low propane conversion, the selectivity did not exceed 60%. At 8 to 9 % of converted propane ($T = 375$°C), the selectivity accounted for around 30%, which is comparable to the results of this work.

0.6 VO_x/CeO_2 and bare ceria were tested in the ODH with CO_2 at a reaction temperature of 550°C after dehydration with He. The reaction was performed for 5h in a fluidised bed mode in order to obtain information on the catalyst stability. The gas composition consisted of 14% C_3H_8/ 13% CO_2/ 73% He at a total flow of 37 ml_n/min. Table 7.1 summarises the measured activity data. Figure 7.2 shows the gas phase contributions detected via the GC for the 0.6 VO_x/CeO_2 catalyst over time, revealing a high amount of produced CO molecules. After starting the reaction, the deposition of coke was observed through the quartz window. Applying equations 3.12 to 3.16, the conversion of CO_2 would account for around 7%, whereas only 1% of propane was converted. Considering that CO_2 may participate via the Boudouard reaction, only half of these CO molecules may actually come from CO_2. The remaining carbon source may be attributed to deposited

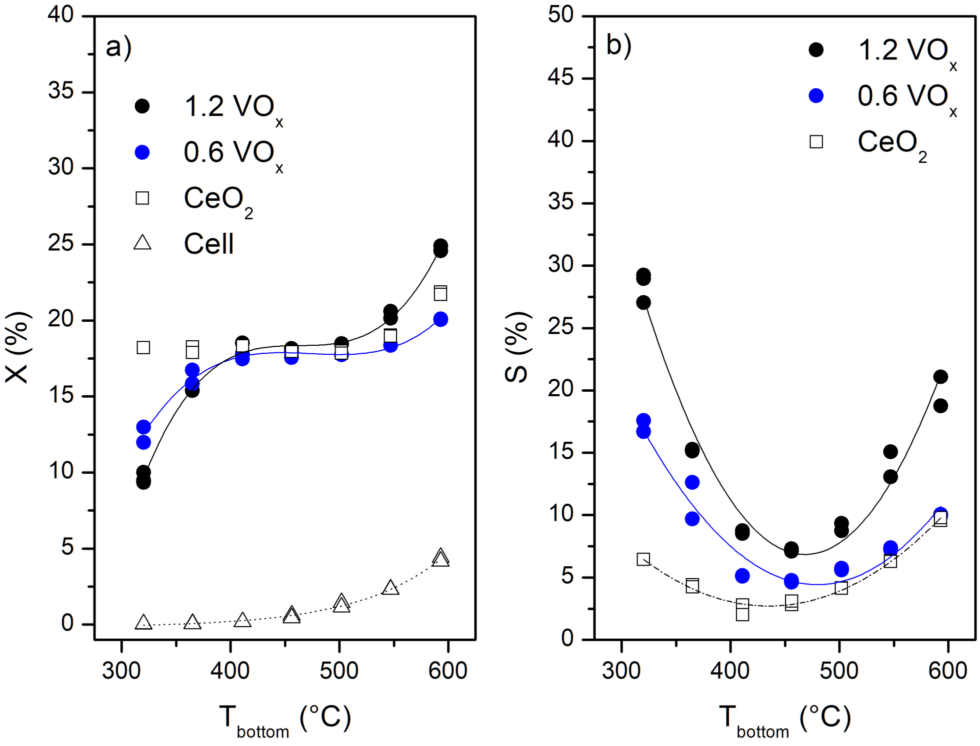

Figure 7.1: Catalytic performance of 1.2 and 0.6 VO_x/CeO_2 catalysts in comparison to bare CeO_2 and the empty cell. a) Propane conversion as a function of temperature. b) Selectivity towards propene; Reaction conditions: 14% C_3H_8 /13% O_2/ 73% He, total flow: 37 ml_n/min. Lines are to guide the eye.

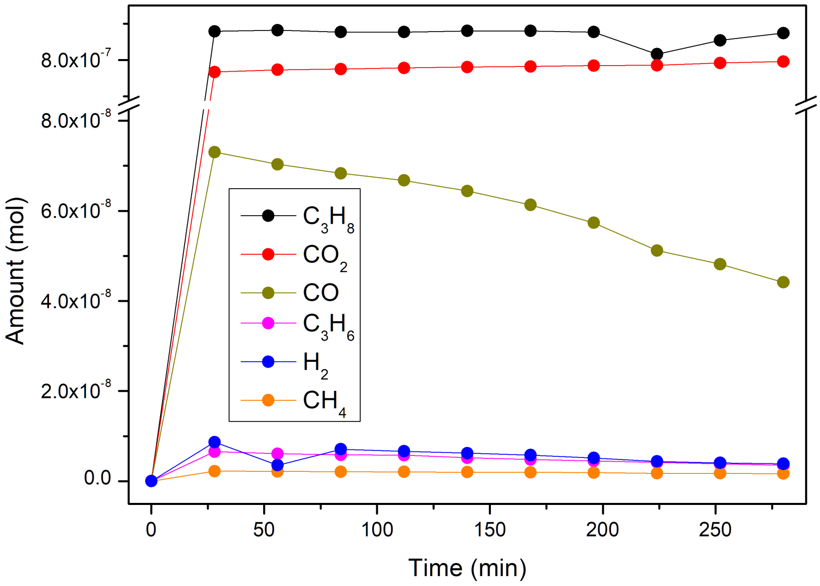

Figure 7.2: Catalytic performance of the 0.6 VO_x/CeO_2 catalyst in propane ODH with CO_2. The amount of respective gas phase contributions is plotted versus time. The gas composition consisted of 14% C_3H_8/ 13% CO_2/ 73% He at a total flow of 37 ml_n/min.

coke, and thus to propane. In the case of bare ceria, the amount of converted propane molecules may be determined to be 3.94 ± 1.64 % via using the amount of propane obtained via the MFC mixing. Previously, Zhang et al. [76] reported the presence of graphite-like coke for the ODH of ethylbenzene over ceria in the absence of CO_2, which is effectively removed in the presence of CO_2. Furthermore, the ratio of C_3H_6 to H_2 indicates that propylene is mainly attributed to (thermal) dehydrogenation. It is suggested that a predominantly reduced catalyst is present. CO_2 activation and reoxidation of the catalyst seem to be the bottleneck over the ceria-based catalyst. Staudt et al. [67] demonstrated that, in principle, ceria is able to activate the CO_2 molecule. However, Nowicka et al. [70] did not observe CO_2 dissociation on a (nonreduced) $CeZrAlO_x$ catalyst without a noble metal.

Table 7.1: Catalytic performance of 0.6 VO_x/CeO_2 and CeO_2 in propane ODH with CO_2; Reaction conditions: 14% C_3H_8/ 13% CO_2/ 73% He, total flow: 37 ml_n/min. The conversion of CO_2 could not be correctly determined.

Catalyst	$X_{C_3H_8}$ (%)	S (%)	CB (%)
0.6 VO_x/CeO_2	0.8 ± 0.2	69 ± 3	<8
CeO_2	1.2 ± 0.3	62 ± 5	<3

Table 7.2: Respective molar ratios of C_3H_6, CO, and H_2.

Catalyst	$\frac{n(C_3H_6)}{n(CO)}$	$\frac{n(C_3H_6)}{n(H_2)}$	$\frac{n(C_3H_6)}{n(H_2)+n(CO)}$
0.6 VO_x/CeO_2	0.08 ± 0.00	1.0 ± 0.3	0.08 ± 0.00
CeO_2	0.10 ± 0.01	1.4 ± 0.5	0.09 ± 0.01

7.2 Characterisation of VO_x/CeO_2: multiwavelength Raman approach

Ceria samples with a vanadium density of 0.6, 1.2, and 2.3 V/nm^2 were characterised via DR UV-vis and Raman spectroscopy. Here, only spectra of the 1.2 VO_x/CeO_2 sample will be discussed.

The DR UV-vis spectrum under dehydrated conditions at 100°C is illustrated in figure 7.3. The shape is largely dominated by the self-absorption of ceria below 400 nm with a maximum at 265 nm and a shoulder at 330 nm, which is attributed to the band gap absorption (O 2p(filled) → Ce 4f(empty) transition) (see Figure S1.6 for comparison with bare ceria).[151, 152] Vanadium oxide absorption features arising from ligand-to-metal charge transfer (LMCT) are hardly observable in this region. The vis region is related to oligomeric vanadium oxide species and/or 2D aggregates of (see inset).[38, 105] The determination of the band edge energy reveals a slight shift from 2.97 eV (0.6 V/nm^2) to 2.86 eV (2.3 V/nm^2) with increasing VO_x density. The amount of V-O-V numbers corresponds to 2.5 and 3, respectively. Excitation wavelengths used for the subsequent Raman study are marked. The respective Raman spectroscopic results are shown in figure 7.4 for the 1.2 VO_x/CeO_2 sample.

As previously demonstrated, the excitation at 256.7 nm was well suited to exploit the resonance effect for VO_x species supported on silica. For ceria samples, however, low Raman peak intensities are obtained at this wavelength, which is related to the strong self-absorption of the support ceria. On the other hand, with excitation at 385 nm, ceria-related modes can be enhanced, whereas vanadium oxide-related features are accessible at excitation wavelengths in the visible. The Raman spectrum at 385 nm consists of two surface ceria modes, the longitudinal (250 cm^{-1}) and transversal Ce-O stretching (405 cm^{-1}). A contribution of the 2TA of CeO_2(111) bulk may also be present at around 250 cm^{-1}.[150] Peaks at around 595 cm^{-1} are assigned to oxygen vacancies in the vicinity of Ce^{3+} ions.[150] Molecular oxygen adsorbed onto a surface oxygen vacancy of ceria, forming a peroxide species, is detected at 830 cm^{-1}.[96, 150, 151, 153] Vibrations at around 710 cm^{-1} arise for VO_x/CeO_2 samples only and are attributed to the V-O-Ce interface bond.[151] In addition, at 515 nm the vanadyl stretch is clearly visible. When zooming in, several contributions are identified. In the case of ceria, V=O exhibits a perpendicular orientation leading to dipole-dipole coupling. Hence, vibrations at 1015, 1030, and 1040 cm^{-1} are associated with dimers, trimers, and oligomers, respectively.[48, 151] The mode at 465 cm^{-1} is the characteristic ceria bulk mode (F_{2g}), which especially dominates the Raman spectra in the pre-resonant (515 nm) and off-resonant regime (633 nm). Furthermore, the 2LO from the ceria bulk is identified at 1170 cm^{-1}.[150] Consequently, the choice of 515 nm and 385 nm excitation wavelenghts allows the dedicated monitoring of ceria surface and bulk modes, as well as vanadium oxide-related Raman features. The excitation at 633 nm does not provide any additional information.

Furthermore, several correlations can be derived in dependency of the loading. The corresponding Raman spectra are not shown here for brevity. With increasing VO_x density, topmost Ce-O vibrations show a linear decrease. At the same time, the peak area below the V-O-Ce and vanadyl band rises linearly. It is reasonable to assume, that the anchoring of vanadium oxide species results in the decline of Ce-O vibrations. Additionally, ceria may be reduced to Ce^{3+}, as previously determined (one Ce^{3+} per VO_2 and three Ce^{3+} per VO)[154]. Popa et al. [155] studied monomeric vanadium oxide adspecies on the CeO_2(111) surface by DFT calculations. Several stable vanadium oxide systems were proposed, named V, VO, VO_2, VO_3, and VO_4. Hereby, the number of oxygen atoms represents the respective amount of oxygen provided by the vanadium oxide phase. They calculated the theoretical frequencies of the normal vibrational modes of the different supported VO_x species. While V-O-Ce (out of phase) vibrations are located at frequencies <676 cm^{-1}, the V-O-Ce (in phase) mode may appear between 701 and 891 cm^{-1}. However, the experimental Raman results can not be unambiguously assigned. Furthermore, no features can be attributed to V-O-V vibrations.

Table 7.3: Summary of assigned Raman features for VO_x/CeO_2 samples

Position (cm^{-1})	Assignment		References
250	Ce-O longitudinal stretch, 2TA	CeO_2(111) surface, CeO_2(111) bulk	[150]
405	Ce-O transversal stretch	CeO_2(111) surface	[150]
465	F_{2g}	CeO_2(111) bulk	[96, 150]
595	Oxygen vacancies	Reduced CeO_{2-x} bulk	[150]
710	V-O-Ce	Interface	[151]
830	O-O	Peroxides	[98, 150, 151, 153]
1015	V=O	Dimer	[48, 151]
1030	V=O	Trimer/Oligomers	[48, 151]
1170	2LO	CeO_2(111) bulk	[96, 150]

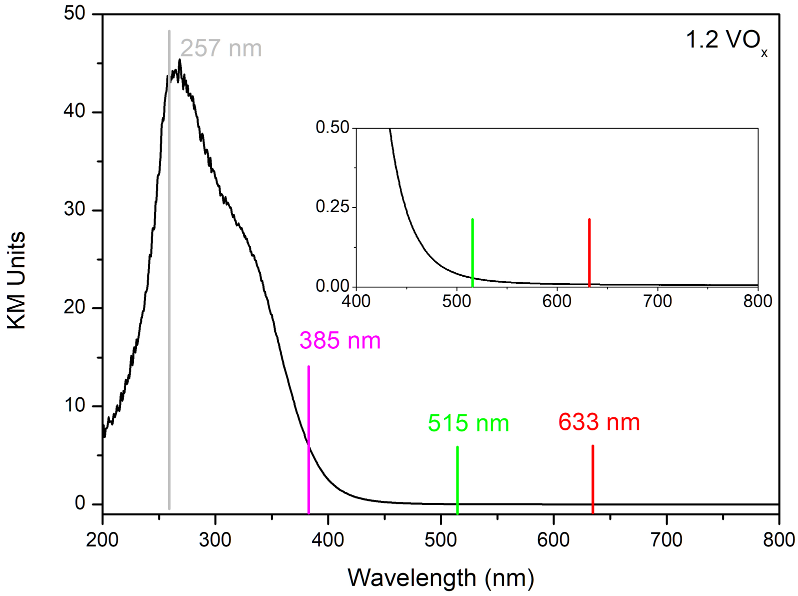

Figure 7.3: *In situ* UV-vis spectrum of the 1.2 VO$_x$/CeO$_2$ catalyst recorded in 8% O$_2$/ 92% N$_2$ flow at 100°C. The excitation wavelengths (257, 385, 515 and 633 nm) used for the Raman experiments are marked. The inset gives an enlarged view of the visible region of the spectrum.

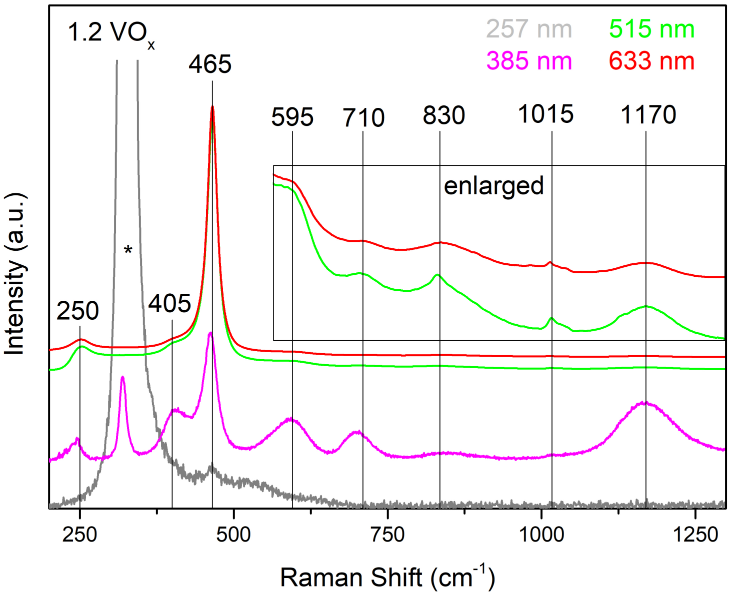

Figure 7.4: Wavelength-dependent Raman spectra of dehydrated 1.2 VO$_x$/CeO$_2$ using 257 nm (grey), 385 nm (magenta), 515 nm (green) and 633 nm (red) wavelength laser excitation. The artefact (marked with an asterisk) at 320 cm^{-1} is due to the CaF$_2$ window of the reaction cell. For 515 and 633 nm excitation, the inset shows an enlarged view of the spectral region between 525 and 1300 cm^{-1}. Spectra are offset for clarity and scaled to allow for the 465 cm^{-1} F$_{2g}$ band to be seen.

The *operando* study for the ODH with ethanol is divided into three parts. First, the catalytic activity is presented for the 1.2 VO_x/CeO_2 and the blank CeO_2 catalyst. On the basis of these results, suitable *operando* conditions were chosen. Secondly, *operando* DR UV-vis and Raman spectra obtained at 385 and 515 nm excitation are analysed. The final mechanistic discussion is intended to provide a direct evidence of active support participation, as previously proposed for VO_x/CeO_2 in methanol ODH [156–158].

Activity study

Figure 7.5 shows the catalytic performance of the 1.2 VO_x/CeO_2 in comparison to blank CeO_2 (reaction conditions: 1% EtOH/ 8% O_2/ 91% N_2). As described in the experimental part, conversion and selectivity were determined on the basis of FTIR gas phase analysis.

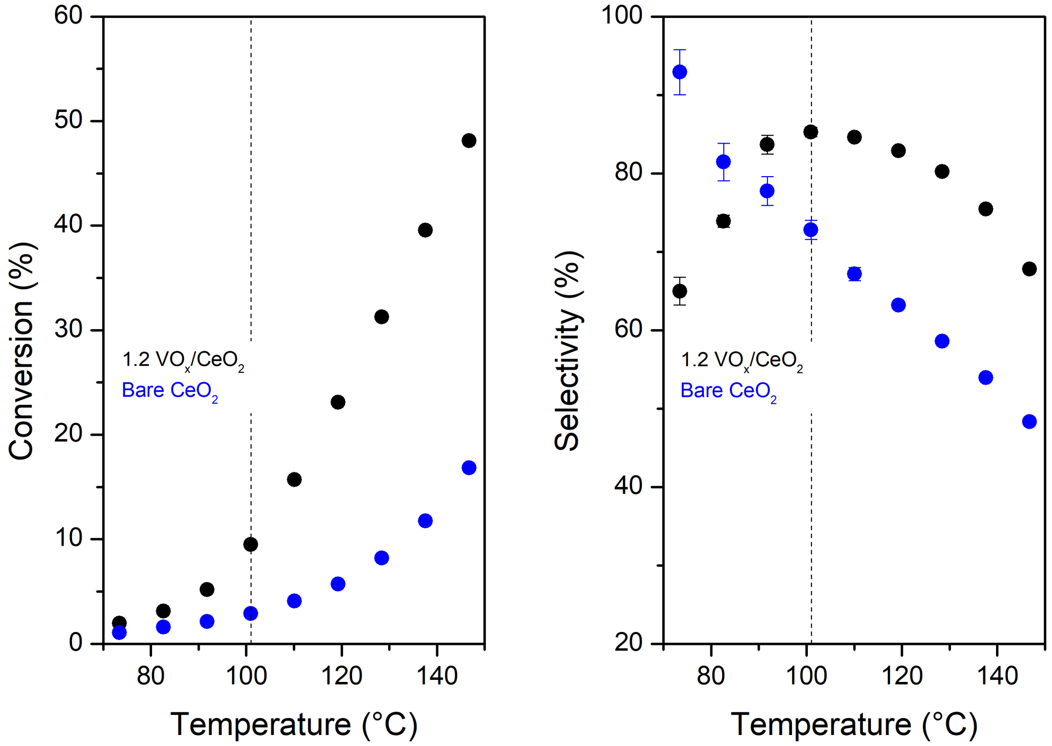

Figure 7.5: Catalytic performance of 1.2 VO_x/CeO_2 (black) as compared to bare CeO_2 (blue) in the ODH of ethanol (gas composition: 1% EtOH/ 8% O_2/ 91% N_2 ; total gas flow: 50 mL_n/min). Left: Ethanol conversion as a function of temperature. Right: Selectivity toward acetaldehyde as a function of temperature. The dashed lines indicate the temperature chosen for the *operando* experiments.

As previously reported [159], bare ceria shows high intrinsic activity at temperatures below 138°C. With increasing temperature, the selectivity towards acetaldehyde drops due to a rising amount of CO_2 and CO. The activity of the impregnated sample is more than doubled. At around 100°C the selectivity shows its maximal value of 85.3 ± 0.6% at a conversion of 9.5 ± 0.0%. When comparing with data for silica supported vanadium oxide [30], it is noted that the total catalytic performance exceeds the contribution of the individual participants. Below 100°C, vanadium oxide deposited on silica shows hardly any ethanol conversion. For the subsequent *operando* study, a reaction temperature of 100°C was chosen. The temperature corresponds to a surface temperature of 92°C as directly measured via a thermocouple in CeO_2 powder.

Operando results under reaction conditions

Figure 7.6 depicts the *operando* UV-vis spectra of 1.2 VO_x/CeO_2 and bare CeO_2 under oxidative (8% O_2 / 92% N_2) and reaction conditions (1% EtOH / 8% O_2 / 91% N_2). Below 400 nm, bare ceria does not show any notable changes. In the case of VO_x/CeO_2, the rather uniform decrease in absorption is attributed to a difference in reflectance conditions. The increase in absorption at around 500 nm for bare ceria indicates its reduction in the presence of ethanol.[150, 160, 161] The feature is even more apparent for the impregnated sample, which points to a higher extent of ceria reduction. Although, d-d transitions of reduced vanadium oxide species are also located in the vis region, a participation of vanadium oxide is unlikely. This would be consistent with the results of theoretical calculations, which propose that CeO_2 changes its oxidation state, but surface vanadium is stabilised to +5.[33, 48]

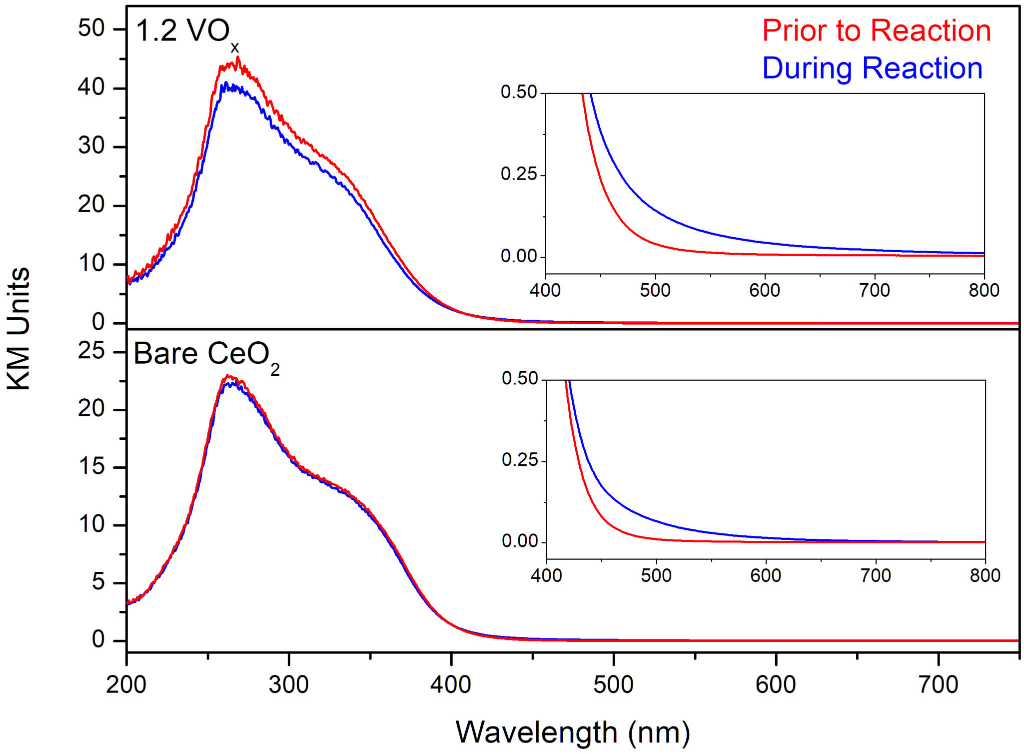

Figure 7.6: *Operando* UV-Vis spectra of the 1.2 VO_x/CeO_2 and CeO_2 catalyst prior to (red) and during (blue) ethanol ODH recorded at a reaction temperature of 100°C. The feed during *in situ* conditions consisted of 8% O_2 / 92% N_2; the feed during *operando* conditions consisted of 1% EtOH / 8% O_2 / 91% N_2. The inset gives an enlarged view of the spectra at longer wavelengths.

The wavelength-dependent Raman results are presented in figure 7.7 and 7.8. *Operando* spectra are depicted for 1.2 VO_x/CeO_2 and bare ceria prior to (8% O_2 / 92% N_2) and during reaction conditions (1% EtOH / 8% O_2 / 91% N_2). Ceria surface, interface and oxygen adsorbate features experience noticeable changes upon switching to reaction conditions, for 385 nm excitation. Surface phonon modes attributed to Ce-O longitudinal and transversal stretching vibrations decrease for both samples, which indicates the reduction of surface ceria, i.e., the consumption of surface lattice oxygen.[150, 152] Additionally, spectra at 515 nm (inset) reveal the reduction of ceria subsurface via the F_{2g} red shift.[150, 152] The larger displacement for VO_x/CeO_2 confirms the observed higher degree of ceria reduction by UV-vis spectroscopy. The V-O-Ce interface peak at 710 cm^{-1} decreases by approximately 50%. Together with the apparent blue shift, a consumption and modification of V-O-Ce linkages during the reaction is assumed. Peroxide features at around 830 cm^{-1}, which are considered as an indicator for surface oxygen vacancies, narrow and red shift. According to previous DFT calculations [150, 162], the changes are interpreted as a transformation of aggregated into more isolated peroxide species. The redistribution is observable for both samples upon switching to reaction conditions.

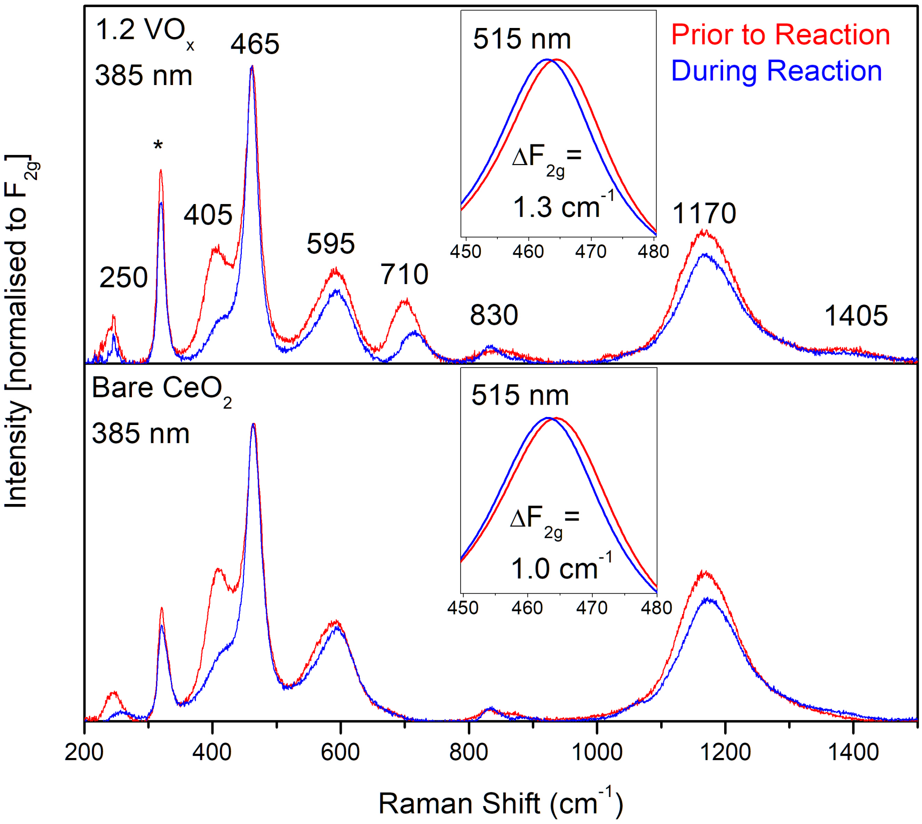

Figure 7.7: *Operando* 385 nm Raman spectra of the 1.2 VO_x/CeO_2 (top panel) as compared to bare ceria (bottom panel) prior to (red) and during (blue) ethanol ODH recorded at 100°C at a total flow rate of 50 mL_n /min. The feed during *in situ* conditions consisted of 8% O_2 / 92% N_2; the feed during *operando* conditions consisted of 1% EtOH / 8% O_2 / 91% N_2. Spectra were normalised to the F_{2g} band.

The Raman results at an excitation wavelength of 515 nm allow the detection of chemisorbed ethanol species within the C-C, C-O, and C-H stretching region. Upon its chemisorption, vanadyl vibrations at 1015 and 1030 cm^{-1} experience a substantial loss in intensity and a downward shift to 1000 cm^{-1}. It is suggested that a coordination of ethanol and/or water to the vanadium oxide structure is responsible for the lengthening of the V=O bond.[131, 133, 151, 163–166]

Previously [167], Raman studies on VO_x/CeO_2 reported a a shift of the terminal V=O bond under hydrated conditions. In this case, 1% V_2O_5/CeO_2 (3% V_2O_5/CeO_2) experienced a red shift of 15 cm^{-1} (9 cm^{-1}) in the presence of water at 170°C, attributed to hydrogen-bonded surface VO_x species solvated by water molecules. The effect of moisture on the V=O stretching frequency was also confirmed by DFT calculations [168, 169] performed for VO_x/titania with a loading of 0.84 VO_x/nm^{-2}, which leads to the conclusion that the experimentally observed red shift may result from hydrogen bonding between the vanadyl bond and surface hydroxyl group (V-OH, Ti-OH) or water molecules. As a result of the coordination, the local structure of the vanadium centre is expected to undergo changes, which may give rise to changes in the orientation of the V=O bonds and leads to a decrease in Raman intensity. This has been previously discussed in the context of IR spectra.[156]

The vibrational signature of adsorbed ethanol species appears to be quite similar for both samples, indicating the primary binding of ethoxy species to the ceria surface. Peaks at 2870, 2930, and 2970 cm^{-1} are assigned to $v_s(CH_2)$, $v_s(CH_3)$, and $v_{as}(CH_3)$ modes, respectively.[170–172] For the VO_x/CeO_2 sample, the vibration at 2930 cm^{-1} is comparatively enhanced. As detected for bare ceria, peaks at 1040, 1050, and 1060 cm^{-1} can be attributed to C-O stretching modes of adsorbed ethoxy species.[172–174] Vibrations detected at 880, 905, 930, and 950 cm^{-1} are located in the C-C stretching region and suggest the presence of different ethoxy species. Previously, IR bands detected at 1050 and 885 cm^{-1} after ethanol exposure to $CeO_2(111)$ were assigned to C-O and C-C stretching vibrations of bidentate ethoxide or ethoxide in an oxygen vacancy, and bands at 1096 and 905 cm^{-1} to the corresponding vibrations of monodentate species.[174, 175] The joint decrease of C-C and C-O vibrations points to the reduction of adsorbed ethoxy species on the ceria surface. Such a behaviour is expected based on the coverage of the ceria support by vanadium oxide ($\approx$ 12% of vanadium oxide monolayer at 10 V/nm^2). In contrast, C-H vibrations indicate an increase in the total amount of adsorbed ethoxy species for the impregnated sample. Moreover, an additional feature arises at around 950 cm^{-1}. Recently, Waleska et al. [30] reported bands at 922 and 1056 cm^{-1} for a silica supported vanadium oxide catalyst, which have been attributed to C-C and C-O stretching vibrations of ethoxy directly attached to vanadium. However, a contribution of ceria-bound ethoxy cannot be excluded here as there is some overlap with the broad 930 cm^{-1} ceria feature. After turning off the EtOH feed, adsorbed ethoxy species do not completely vanish after the reaction (not shown here). In the case of bare ceria, C-C and C-H vibrations appear with a signature including a vibration at around 940 cm^{-1}. Consequently, the vanadium oxide-related C-C feature at 950 cm^{-1} cannot be unambiguously identified so far.

Raman spectra obtained at 515 nm show the presence of hydroxyl groups at 3640 and 3680 cm^{-1} on the ceria surface, prior to reaction. During the reaction, a broad OH-related band between 3300 and 3700 cm^{-1} appears, which is assignable to hydrogen bonding interactions of OH groups with adsorbed ethoxy species and/or water. It is noted that water is formed as a reaction product during the reaction.[176] A summary of features, which appeared during the reaction, is given in table 7.4.

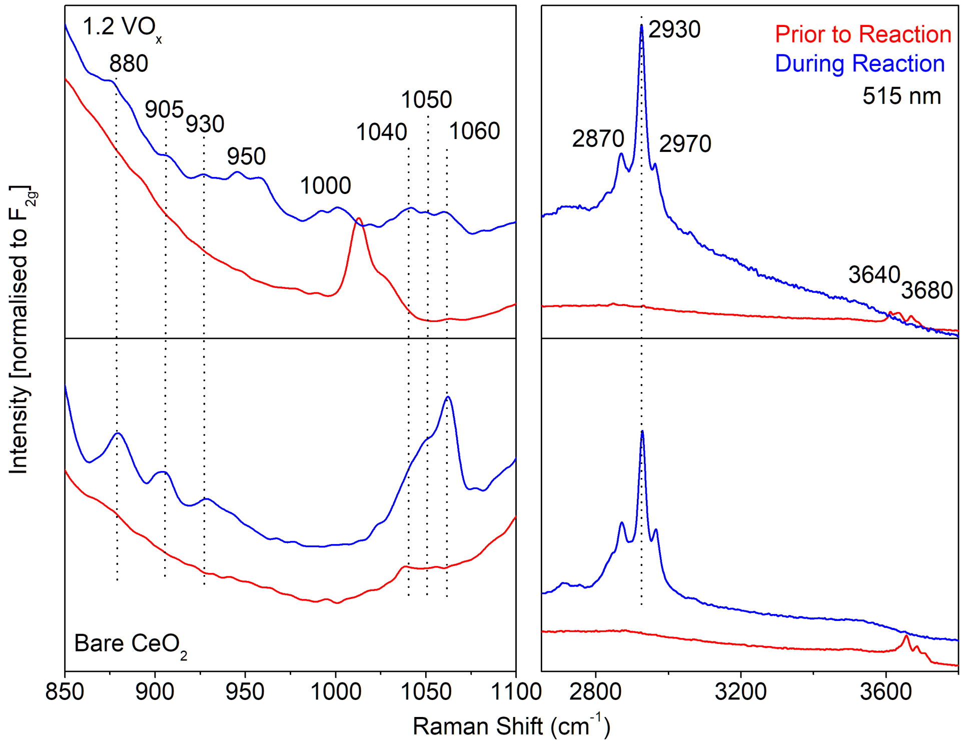

Figure 7.8: *Operando* 515 nm Raman spectra of the 1.2 VO$_x$/CeO$_2$ catalyst (top panel) as compared to bare ceria (bottom panel) prior to (red) and during (blue) ethanol ODH recorded at 100°C at a total flow rate of 50 mL$_n$/min.The feed during *in situ* conditions consisted of 8% O$_2$ / 92% N$_2$; the feed during *operando* conditions consisted of 1% EtOH / 8% O$_2$ / 91% N$_2$. Spectra were normalised to the F$_{2g}$ band and offset for clarity.

Table 7.4: Summary of assigned Raman features for VO$_x$/CeO$_2$ samples during the reaction

Position (cm^{-1})	Assignment		References
880	C-C	Ethoxy	[174]
905	C-C	Ethoxy	[174]
930	C-C	Ethoxy	this work
950	C-C	Ethoxy	this work
1000	V=O	Vanadyl coordinated with water/ethanol	[167]
1040	C-O	Ethoxy	this work
1050	C-O	Ethoxy	[174, 175]
1060	C-O	Ethoxy	this work
2870	$\nu_s(CH_2)$	Ethoxy	[174]
2930	$\nu_s(CH_3)$	Ethoxy	[174]
2970	$\nu_{as}(CH_3)$	Ethoxy	[174]

Mechanistic discussion

The findings from *operando* spectroscopy enable the proposal of a reaction mechanism for the ODH with ethanol (see figure 7.9).

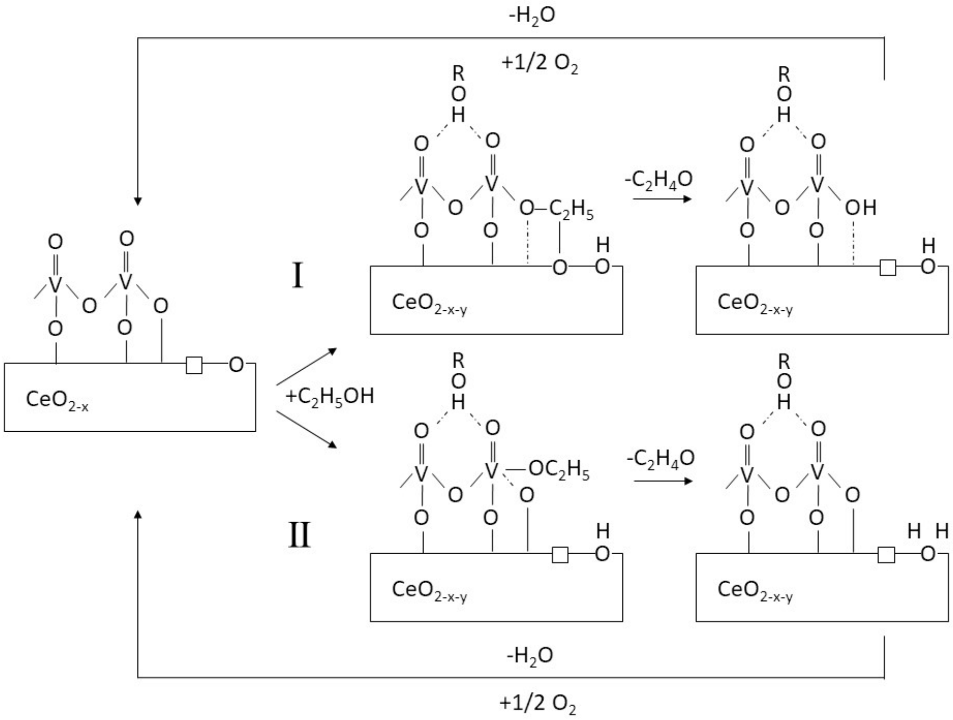

Figure 7.9: Proposed reaction mechanism for a VO_x/CeO_2 catalyst based on the analysis of the *operando* spectroscopic data presented in this work.

For bare ceria, the reaction cycle starts with the formation of chemisorbed ethoxy species on the surface, which is indicated by the reduction of the surface phonon signal at 405 cm $^{-1}$. C-C stretching vibrations indicate the presence of at least three different ethoxy formations on ceria surface, which goes along with a hydrogen transfer to a lattice oxygen. Acetaldehyde may then proceed by another hydrogen transfer to a hydroxyl group, leading to water formation, as suggested by the changes in the O-H stretching region. Kropp et al. [177] studied the oxidative dehydrogenation of methanol at the pristine and O-defective ceria (111) surfaces via DFT calculations. A higher intrinsic barrier was determined for the the reduced surface. Furthermore, Wu et al. [178] determined that the on-top methoxy species (type I) is the only one for ceria octahedra (111). At a reaction temperature of 100°C, the red shift of the F_{2g} points to the formation of oxygen vacancies in the ceria subsurface. Consequently, it is proposed that ceria bulk and subsurface serve as an oxygen buffer. However, the reaction mechanism for bare ceria cannot be completely understood so far, based on the insufficient assignment of the adsorbed ethoxy species.

For VO_x/CeO_2 two different pathways may be proposed. According to the band edge analysis and the Raman results of the dehydrated VO_x/CeO_2 sample, the predominant vanadium oxide structures are dimers and trimers. The deposition of vanadium oxide onto the ceria surface covers active ceria surface oxygen. Nonetheless, conversion values increased significantly, which points to a synergetic effect. Wu and Gong [158] proposed that oxygen of the interface V-O-Ce group is catalytically more active than the O of the VO_x and the ceria support. Pathway I starts with the chemisorption of ethoxy species on the ceria surface in vicinity to surface vanadium oxide, which goes along with a blue shift of the V-O-Ce interface bond. Hence, a subsequent hydrogen transfer to V-O-Ce is facilitated, consistent with predictions from theory [156]. The spectral changes of the vanadyl are no indicative for a significant reduction of vanadium, which is in agreement with the DFT literature [156, 158]. Thus, vanadium oxide appears to play a coordinative role rather than that of a redox system. In pathway II, ethoxy is directly attached to vanadium by the breakage of the V-O-Ce interface. As a result, a vanadium-bound ethoxy species is formed, which is accompanied by a hydrogen transfer to lattice oxygen. The subsequent conversion to acetaldehyde may then involve another hydrogen transfer to lattice oxygen or to a hydroxyl group leading to water formation, which is observed in the O-H stretching region.

7.4 Conclusion and outlook

The proposed mechanism demonstrates the support effect of CeO_2 in the ODH with EtOH. It is the first direct evidence of oxide support participation, as previously proposed in the literature [33, 38, 44, 47, 48, 124]. To sum up, vanadium oxide does not experience any notable reduction. Instead, ceria becomes reduced while stabilising vanadium to +5. The ceria bulk acts as an oxygen buffer. It is suggested that the V-O-Ce interface bond plays a crucial role for the selective formation of acetaldehyde. On an inactive support like, e.g., silica, vanadium oxide species experience a high degree of reduction upon the chemisorption of ethoxy species. V-O-V and V-O-Si linkages are consumed, and the oligomerisation degree decreases strongly as observed by UV-vis spectroscopy. The electronic exchange occurs between VO_x species and ethoxy species without the participation of the support. The terminal oxygen is considered to be the active oxygen.[30]

The developed multiwavelength approach may also be applicable to propane ODH, giving access to the dynamic of the V-O-Ce interface, Ce-O surface modes and bulk behaviour (F_{2g}) under reaction conditions. The activity study in section 7.1 showed that ceria itself is highly active. The low selectivity towards propylene may be attributed to unselective ceria surface oxygen. The amount of deposited vanadium oxide seems to tune obtained selectivity values at low temperatures. Hence, unselective oxygen species may be covered with vanadium oxide. Huang et al. [179] studied the C-H activation of propane on VO_3/CeO_2 (111) via DFT calculations. Isopropoxide is either dissociatively adsorbed at O-Ce-O or V-O-Ce. The pathway over V-O-Ce is favoured, which leaves the abstracted hydrogen at a nearby surface Ce-O-Ce. The following C-H activation may occur with a relatively higher barrier at a nearby free V-O-Ce resulting in the formation and desorption of propene. The study pointed to the importance of the so-called characteristic new empty localised states (NELS), which are created by the deposition of VO_3 and VO_4 clusters on the ceria surface [158].

The performance of ceria also shows a strong dependency on the oxidising agent. At 550°C, CO_2 did not effectively participate in the reoxidation of ceria. To obtain a better understanding of the ODH with CO_2, the reaction should be studied by varying the reaction temperature, C_3H_8:CO_2 ratio, vanadium oxide loading, and in the absence of CO_2. Moreover, the effect of morphology might be of interest.[75]

At last, the calculation of Raman spectra should be emphasised in the future.[150]

8 Conclusion and outlook

In this work, a novel *operando* setup was successfully established, which allowed the investigation of ODH reactions in dependency of the substrate and the oxidising agent. Catalytic measurements combined with multiwavelength Raman, DR UV-vis, or DRIFT spectroscopy could either be monitored via gas chromatography or FTIR gas phase analysis. Two different commercial *in situ* cell were used. The *in situ* cells by Linkam Scientific Instruments Ltd. in combination with the fluidised bed mode was particularly suitable for the *operando* approach studying high-temperature reactions. The fluidised bed method was successfully implemented for a silica supported vanadium oxide sample. The activity data obtained in the *in situ* cell was in agreement with values achieved in a conventional reactor for propane ODH.[10, 36] There are only a few *operando* studies available in the literature, where this is the case.[110] While using CO_2 as an oxidising agent, reoxidation of the catalyst could (at least) be guaranteed in the hotter bottom due to the constant particle mixing in the sample bed. An important question in this context is: Which temperature do the particles during the spectroscopic measurement exactly have? One may use the shift of the ceria F_{2g} bulk feature to determine the actual temperature in dependency of the set temperature. For that, reference data is needed including the Raman shift value at room temperature in order to consider the respective Raman shift calibration.[180] The spectroscopic window CaF_2 turned out to show high sensitivity towards the temperature gradient from the inside to the outside of the Raman reactor causing shearing. In the future, alternative windows like magnesium fluoride (MgF_2) might be considered.

Previously, Waleska et al. [30] reported time-resolved UV Raman data combined with FTIR spectroscopy. This kind of approach might be of further interest in the future. The setup would already allow the simultaneous operation of GC-MS and GC-FTIR. Furthermore, kinetic data might be measured in a common reactor in order to obtain a better understanding of the catalytic performance of the catalyst.

Multiwavelength Raman spectroscopy, which allowed the resonance Raman effect to be exploited in a targeted manner, was combined with UV-vis and DRIFT spectroscopy and applied under reaction conditions. The absence of significant structural dynamics led to the conclusion that the catalyst is in a low reduced/fully oxidised state. This strongly indicates that the first C-H activation of the propane molecule is the rate-determining step. So far, only kinetic studies and isotope labelling experiments have led to this suggestion.[10] In the absence of molecular oxygen, the catalyst was highly reduced, resulting in an increase in d-d transition related to V(3+)/V(4+). The rise in self-absorption in the vis region may be (partly) responsible for the signal loss in 515 nm Raman spectra. In contrast, 256.7 nm Raman spectra provided information on the highly reduced state. Redox properties were studied in a complementary reduction experiment using propane and hydrogen. At a temperature of 446°C, V=O, V-O-V, and V-O-Si are significantly affected. While including the observation of SiO-H vibrations, the spectroscopic data indicate that, in principle, all pathways, calculated for dimeric and monomeric structures, are possible. The experimental observations give a direct evidence of theoretical calculations proposed in the literature [39, 40]. With a fully oxidised catalyst, the terminal oxygen is responsible for the first hydrogen abstraction from the propane molecule. The second C-H activation of the propyl radical may proceed at the same vanadium site or at another one. For a quantification of the degree of reduction via a Raman TPR experiment, a fast and reliable hydrogen detection would be necessary in the future. However, the results already allowed a classification of the extent of reduction based on UV Raman and UV-vis experiments into low and high reduction. Ethanol ODH has been used to serve as a prototype reaction in the past. *Operando* results reported in the literature [30] successfully verified the chemisorption of ethoxy species on vanadium oxide sites. Respective Raman spectra demonstrated that ethoxy-related features experience resonance enhancement triggered by the VO_x moiety while exciting in the UV. Neither UV Raman nor DRIFT spectroscopy clearly identified isopropoxide and isopropanol intermediate structures in propane ODH. Also VO-H vibrations could not be observed under reaction conditions. These results strongly suggested that reoxidation occurs fast in propane ODH with O_2. However, in order to obtain a better understanding of *operando* data and resonance Raman effects, the calculation of theoretical absorption and Raman spectra [113] might be helpful to confirm the assignment of several Raman vibrations of supported vanadium species.

As a third part of this work, propane ODH was studied using CO_2 as an oxidising agent. The generation of a significant amount of CO was ascribed to the successful activation of CO_2 molecules. The *operando* experiment was extended with a hydrogen pretreatment procedure including hydrogen reduction followed by subsequent CO_2 reoxidation. The silica supported vanadium oxide catalyst was in a highly reduced state during *operando* conditions. However, V=O features declined comparatively less than V-O-V vibrations. This might be an indication that CO_2 forms Lewis acid sites via the lone pair of oxygen on vanadium 3+. Hence, the redox cycle was described as V(5+)/V(3+). Possible reoxidation of other oxygen bonds might proceed via hydrogen migration processes. As the reaction performs at high selectivity, several selectivity-determining factors were discussed. The high reduction of the present catalyst resulted in a decrease of oligomerisation and a spatial separation of active oxygen sites. In the future, chromium oxide might be of interest as a redox system for propane ODH with CO_2.[61–63]

Finally, the catalytic performance of ceria supported vanadium oxide was studied. Ceria, as considered an active support, shows high activity in propane ODH already itself, however, with low selectivity. In order to obtain an insight into the support effect of CeO_2, ethanol ODH was chosen as a prototype reaction. Beforehand, a multiwavelength approach (385 nm and 515 nm) for the detection of ceria bulk, surface and vanadium oxide-related modes was successfully established. The *operando* setup was complemented with FTIR gas phase analysis. Active support participation could be successfully verified. While ceria becomes reduced, vanadium is stabilised in its oxidation state 5+. The results demonstrated the relevance of V-O-Ce interface bonds, which are consumed by 50% during the reaction. Moreover, several ethoxy species adsorbed on the ceria surface were identified by their shifted C-C stretching vibration. The results indicate that ceria is serving as an oxygen buffer for reduced vanadium species. Hence, it would be of great interest to transmit the gained knowledge to propane ODH experiments with O_2 and CO_2 in the future. Furthermore, a generalisability might be derived for the performance of active (e.g. TiO_2) and inactive supports (e.g. Al_2O_3). In principle, the presented approach is also applicable in combination with different redox systems like, e.g., molybdenum and chromium oxides when taking their absorption behaviour into account.

References

[1] Intergovernmental Panel on Climate Change, *Climate change 2013: The physical science basis*, Cambridge University Press, New York, NY, USA, **2014**.

[2] Intergovernmental Panel on Climate Change, *Global warming of 1.5°C*, IPCC, Geneva, Switzerland, **2018**.

[3] United Nations Climate Change, Paris Agreement, **2015**.

[4] International Energy Agency, *Energy technology perspectives: Scenarios & strategies to 2050 : in support of the G8 Plan of action*, OECD, IEA, Paris, **2006-2012**.

[5] IEA, Technology Roadmap Energy and GHG Reductions in the Chemical Industry via Catalytic Processes, **2013**.

[6] F. Schüth, *ChiuZ* **2006**, *40*, 92–103.

[7] E. Roduner, W. Kaim, B. Sarkar, V. B. Urlacher, J. Pleiss, R. Gläser, W.-D. Einicke, G. A. Sprenger, U. Beifuß, E. Klemm, C. Liebner, H. Hieronymus, S.-F. Hsu, B. Plietker, S. Laschat, *ChemCatChem* **2013**, *5*, 82–112.

[8] Peter Eisele, Richard Killpack, *Ullmann's Encyclopedia of Industrial Chemistry*, Wiley, Weinheim, Germany, **2000**.

[9] J. Bricker, History and State of the Art of Ethane/Propane Dehydrogenation Catalysis. Washington, DC, **2016-03-07**.

[10] C. A. Carrero, R. Schloegl, I. E. Wachs, R. Schomaecker, *ACS Catal.* **2014**, *4*, 3357–3380.

[11] F. Cavani, N. Ballarini, A. Cericola, *Catal. Today* **2007**, *127*, 113–131.

[12] G. Centi, F. Cavani, F. Trifirò, *Selective Oxidation by Heterogeneous Catalysis*, Springer, Boston, MA, **2001**.

[13] B. M. Weckhuysen, D. E. Keller, *Catal. Today* **2003**, *78*, 25–46.

[14] G. Ertl, *Handbook of heterogeneous catalysis*, Wiley-VCH, Weinheim and Chichester, **2008**.

[15] C. Hess, *Chemphyschem* **2009**, *10*, 319–326.

[16] C. Hess, *Nanostructured catalysts: Selective oxidations*, RSC, Cambridge, **2011**.

[17] I. E. Wachs, *Dalton Trans.* **2013**, *42*, 11762–11769.

[18] M. Aresta, A. Dibenedetto, *Dalton Trans.* **2007**, 2975–2992.

[19] M. Aresta, A. Dibenedetto, A. Angelini, *J. CO2 Util.* **2013**, *3-4*, 65–73.

[20] A. Al-Mamoori, A. Krishnamurthy, A. A. Rownaghi, F. Rezaei, *Energy Technol.* **2017**, *5*, 834–849.

[21] M. B. Ansari, S.-E. Park, *Energy Environ. Sci.* **2012**, *5*, 9419.

[22] G. Raju, B. M. Reddy, S.-E. Park, *Indian J. Chem.* **2012**.

[23] S. Kawi, Y. Kathiraser, *Front. Energy Res.* **2015**, *3*, 21.

[24] M. A. Atanga, F. Rezaei, A. Jawad, M. Fitch, A. A. Rownaghi, *Appl. Catal. B* **2018**, *220*, 429–445.

[25] D. Mukherjee, S.-E. Park, B. M. Reddy, *J. CO_2 Util.* **2016**, *16*, 301–312.

[26] B. M. Weckhuysen, *Phys. Chem. Chem. Phys.* **2003**, *5*, 4351.

[27] M. A. Bañares, *Catal. Today* **2005**, *100*, 71–77.

[28] M. A. Bañares, *Adv. Mater.* **2011**, *23*, 5293–5301.

[29] A. Chakrabarti, M. E. Ford, D. Gregory, R. Hu, C. J. Keturakis, S. Lwin, Y. Tang, Z. Yang, M. Zhu, M. A. Bañares, I. E. Wachs, *Catal. Today* **2017**, *283*, 27–53.

[30] P. Waleska, S. Rupp, C. Hess, *J. Phys. Chem. C* **2018**, *122*, 3386–3400.

[31] J. P. Thielemann, F. Girgsdies, R. Schlögl, C. Hess, *Beilstein J. Nanotechnol.* **2011**, *2*, 110–118.

[32] M. V. Ganduglia-Pirovano, *Catal. Today* **2015**, *253*, 20–32.

[33] M. V. Ganduglia-Pirovano, C. Popa, J. Sauer, H. Abbott, A. Uhl, M. Baron, D. Stacchiola, O. Bondarchuk, S. Shaikhutdinov, H.-J. Freund, *J. Am. Chem. Soc.* **2010**, *132*, 2345–2349.

[34] E. V. Kondratenko, M. Cherian, M. Baerns, *Catal. Today* **2006**, *112*, 60–63.

[35] I. Ascoop, V. V. Galvita, K. Alexopoulos, M.-F. Reyniers, P. van der Voort, V. Bliznuk, G. B. Marin, *J. Catal.* **2016**, *335*, 1–10.

[36] A. Dinse, S. Khennache, B. Frank, C. Hess, R. Herbert, S. Wrabetz, R. Schlögl, R. Schomäcker, *J. Mol. Catal. Chem.* **2009**, *307*, 43–50.

[37] C. Doornkamp, V. Ponec, *J. Mol. Catal. A: Chem.* **2000**, *162*, 19–32.

[38] B. Beck, M. Harth, N. G. Hamilton, C. Carrero, J. J. Uhlrich, A. Trunschke, S. Shaikhutdinov, H. Schubert, H.-J. Freund, R. Schlögl, J. Sauer, R. Schomäcker, *J. Catal.* **2012**, *296*, 120–131.

[39] X. Rozanska, R. Fortrie, J. Sauer, *J. Phys. Chem. C* **2007**, *111*, 6041–6050.

[40] X. Rozanska, R. Fortrie, J. Sauer, *J. Am. Chem. Soc.* **2014**, *136*, 7751–7761.

[41] G.-L. Dai, Z.-H. Li, J. Lu, W.-N. Wang, K.-N. Fan, *J. Phys. Chem. C* **2011**, *116*, 807–817.

[42] X. Rozanska, E. Kontratenko, J Sauer, *J. Catal.* **2008**, *256*, 84–94.

[43] O. Ovsitser, M. Cherian, E. V. Kondratenko, *J. Phys. Chem. C* **2007**, *111*, 8594–8602.

[44] A. Dinse, B. Frank, C. Hess, D. Habel, R. Schomäcker, *J. Mol. Catal. A: Chem.* **2008**, *289*, 28–37.

[45] I. E. Wachs, *Catal. Today* **2005**, *100*, 79–94.

[46] A. Lemonidou, L. Nalbandian, I. Vasalos, *Catal. Today* **2000**, *61*, 333–341.

[47] H. Tian, E. I. Ross, I. E. Wachs, *J. Phys. Chem. B* **2006**, *110*, 9593–9600.

[48] M. Baron, H. Abbott, O. Bondarchuk, D. Stacchiola, A. Uhl, S. Shaikhutdinov, H.-J. Freund, C. Popa, M. V. Ganduglia-Pirovano, J. Sauer, *Angew. Chem. Int. Ed.* **2009**, *48*, 8006–8009.

[49] H. L. Abbott, A. Uhl, M. Baron, Y. Lei, R. J. Meyer, D. J. Stacchiola, O. Bondarchuk, S. Shaikhutdinov, H. J. Freund, *J. Catal.* **2010**, *272*, 82–91.

[50] H.-J. Freund, M. W. Roberts, *Surf. Sci.* **1996**, *25*, 225–273.

[51] H.-J. Freund, R. P. Messmer, *Surf. Sci.* **1986**, *172*, 1–30.

[52] W. Taifan, J.-F. Boily, J. Baltrusaitis, *Surf. Sci.* **2016**, *71*, 595–671.

[53] G. Busca, V. Lorenzelli, *J. Mater. Chem.* **1982**, *7*, 89–126.

[54] T. Shishido, K. Shimamura, K. Teramura, T. Tanaka, *Catal. Today* **2012**, *185*, 151–156.

[55] Y. Cheng, F. Zhang, Y. Zhang, C. Miao, W. Hua, Y. Yue, Z. Gao, *Chin. J. Catal.* **2015**, *36*, 1242–1248.

[56] M. A. Botavina, Y. A. Agafonov, N. A. Gaidai, E. Groppo, V. Cortés Corberán, A. L. Lapidus, G. Martra, *Catal. Sci. Technol.* **2016**, *6*, 840–850.

[57] K. Nakagawa, C. Kajita, K. Okumura, N.-o. Ikenaga, M. Nishitani-Gamo, T. Ando, T. Kobayashi, T. Suzuki, *J. Catal.* **2001**, *203*, 87–93.

[58] G. Raju, B. M. Reddy, B. Abhishek, Y.-H. Mo, S.-E. Park, *Appl. Catal. A* **2012**, *423-424*, 168–175.

[59] M. Setnička, P. Čičmanec, E. Tvarůžková, R. Bulánek, *Top. Catal.* **2013**, *56*, 662–671.

[60] G. Sun, Q. Huang, S. Huang, Q. Wang, H. Li, H. Liu, S. Wan, X. Zhang, J. Wang, *Catalysts* **2016**, *6*, 41.

[61] P. Michorczyk, J. Ogonowski, P. Kuśtrowski, L. Chmielarz, *Appl. Catal. A* **2008**, *349*, 62–69.

[62] P. Michorczyk, J. Ogonowski, M. Niemczyk, *Appl. Catal. A* **2010**, *374*, 142–149.

[63] P. Michorczyk, J. Ogonowski, K. Zeńczak, *J. Mol. Catal. A: Chem.* **2011**, *349*, 1–12.

[64] P. Michorczyk, P. Pietrzyk, J. Ogonowski, *Microporous Mesoporous Mater.* **2012**, *161*, 56–66.

[65] I. Takahara, M. Saito, M. Inaba, K. Murata, *Catal. Lett.* **2005**, *102*, 201–205.

[66] S. Wang, K. Murata, T. Hayakawa, S. Hamakawa, K. Suzuki, *Appl. Catal. A* **2000**, *196*, 1–8.

[67] T. Staudt, Y. Lykhach, N. Tsud, T. Skála, K. C. Prince, V. Matolín, J. Libuda, *J. Catal.* **2010**, *275*, 181–185.

[68] K. Chang, H. Zhang, M.-j. Cheng, Q. Lu, *ACS Catal.* **2019**, *10*, 613–631.

[69] R. X. Valenzuela, G. Bueno, V. Cortés Corberán, Y. Xu, C. Chen, *Catal. Today* **2000**, *61*, 43–48.

[70] E. Nowicka, C. Reece, S. M. Althahban, K. M. H. Mohammed, S. A. Kondrat, D. J. Morgan, Q. He, D. J. Willock, S. Golunski, C. J. Kiely, G. J. Hutchings, *ACS Catal.* **2018**, *8*, 3454–3468.

[71] E. Gomez, S. Kattel, B. Yan, S. Yao, P. Liu, J. G. Chen, *Nat. Commun.* **2018**, *9*, 1398.

[72] J. Ogonowski, E. Skrzyńska, *React. Kinet. Catal. Lett.* **2006**, *88*, 293–300.

[73] G. Raju, B. M. Reddy, S.-E. Park, *J. CO_2 Util.* **2014**, *5*, 41–46.

[74] K. N. Rao, B. M. Reddy, B. Abhishek, Y.-H. Seo, N. Jiang, S.-E. Park, *App. Catal. B* **2009**, *91*, 649–656.

[75] M. Kovacevic, S. Agarwal, B. L. Mojet, J. G. van Ommen, L. Lefferts, *Appl. Catal. A* **2015**, *505*, 354–364.

[76] L. Zhang, Z. Wu, N. C. Nelson, A. D. Sadow, I. I. Slowing, S. H. Overbury, *ACS Catal.* **2015**, *5*, 6426–6435.

[77] Z.-W. Liu, C. Wang, W.-B. Fan, Z.-T. Liu, Q.-Q. Hao, X. Long, J. Lu, J.-G. Wang, Z.-F. Qin, D. S. Su, *ChemSusChem* **2011**, *4*, 341–345.

[78] C. Hess, *Top. Catal.* **2013**, *56*, 1593–1600.

[79] F. C. Meunier, *React. Chem. Eng.* **2016**, *1*, 134–141.

[80] H. Li, M. Rivallan, F. Thibault-Starzyk, A. Travert, F. C. Meunier, *Phys. Chem. Chem. Phys.* **2013**, *15*, 7321–7327.

[81] Y. T. Chua, P. C. Stair, *J. Catal.* **2000**, *196*, 66–72.

[82] P. Beato, E. Schachtl, K. Barbera, F. Bonino, S. Bordiga, *Catal. Today* **2013**, *205*, 128–133.

[83] B. Kilos, A. T. Bell, E. Iglesia, *J. Phys. Chem. C* **2009**, *113*, 2830–2836.

[84] H. Nair, J. E. Gatt, J. T. Miller, C. D. Baertsch, *J. Catal.* **2011**, *279*, 144–154.

[85] H. Kim, K. M. Kosuda, Van Duyne, Richard P., P. C. Stair, *Chem. Soc. Rev.* **2010**, *39*, 4820–4844.

[86] Z. Wu, *Chin. J. Catal.* **2014**, *35*, 1591–1608.

[87] Y. T. Chua, P. C. Stair, I. E. Wachs, *J. Phys. Chem. B* **2001**, *105*, 8600–8606.

[88] E. Smith, G. Dent, *Modern Raman spectroscopy: A practical approach*, J. Wiley, Hoboken NJ, **2005**.

[89] T. Dieing, O. Hollricher, J. Toporski, *Confocal Raman microscopy*, Springer, Heidelberg Germany and New York, **2010**.

[90] D. A. Long, *The Raman effect: A unified treatment of the theory of Raman scattering by molecules*, Wiley, Chichester and New York, **2002**.

[91] B. Schrader, D. Bougeard, *Infrared and Raman spectroscopy: Methods and applications*, VCH, Weinheim and New York, **1995**.

[92] G. Mestl, *J. Mol. Catal. A: Chem.* **2000**, *158*, 45–65.

[93] Z. Hong, S. A. Asher, *J. Appl. Spectrosc.* **2015**, *69*, 75–83.

[94] M. Dieterle, Dissertation, Technischen Universität Berlin, Berlin, **2001**.

[95] P. Ruff, S. Lauterbach, H.-J. Kleebe, C. Hess, *Microporous Mesoporous Mater.* **2016**, *235*, 160–169.

[96] A. Filtschew, K. Hofmann, C. Hess, *J. Phys. Chem. C* **2016**, *120*, 6694–6703.

[97] G. H. Vogel, G. Kaibel, *Verfahrensentwicklung: Von der ersten Idee zur chemischen Produktionsanlage*, Wiley-VCH, Weinheim, **2007**.

[98] A. Filtschew, Dissertation, Technische Universität Darmstadt, Darmstadt, **2018**.

[99] R. Herbert, Di Wang, R. Schomäcker, R. Schlögl, C. Hess, *Chemphyschem* **2009**, *10*, 2230–2233.

[100] P. Waleska, Dissertation, Technische Universität Darmstadt, Darmstadt, **2018**.

[101] A. Filtschew, C. Hess, *J. Phys. Chem. C* **2017**, *121*, 19280–19287.

[102] C. Hess, *J. Catal.* **2007**, *248*, 120–123.

[103] Positive Light, Indigo-S: All-solid-state, tunable narrow linewidth ultra-violet laser, **2003**.

[104] R. L. McCreery, *Raman spectroscopy for chemical analysis*, John Wiley & Sons, New York, **2000**.

[105] D. Nitsche, C. Hess, *J. Phys. Chem. C* **2016**, *120*, 1025–1037.

[106] M. V. Martínez-Huerta, G. Deo, J. L. G. Fierro, M. A. Bañares, *J. Phys. Chem. C* **2008**, *112*, 11441–11447.

[107] Korth Kristalle GmbH, Calciumfluorid / RAMAN (CaF2).

[108] B. M. Weckhuysen, R. A. Schoonheydt, *Catal. Today* **1999**, *49*, 441–451.

[109] F. C. Meunier, *Chem. Soc. Rev.* **2010**, *39*, 4602–4614.

[110] M. Bañares, S. Khatib, *Catal. Today* **2004**, *96*, 251–257.

[111] K. Snavely, B. Subramaniam, *J. Chromatogr. Sci.* **1998**, *36*, 191–196.

[112] Agilent Technologies, Understanding Your ChemStation, **0007–0009**.

[113] D. Maganas, A. Trunschke, R. Schlögl, F. Neese, *Faraday Discuss.* **2016**, *188*, 181–197.

[114] D. Nitsche, C. Hess, *J. Raman Spectrosc.* **2013**, *44*, 1733–1738.

[115] P. S. Waleska, C. Hess, *J. Phys. Chem. C* **2016**, *120*, 18510–18519.

[116] D. Shee, G. Deo, *Catal. Today* **2019**, *325*, 25–32.

[117] Z. Wu, S. Dai, S. H. Overbury, *J. Phys. Chem. C* **2009**, *114*, 412–422.

[118] P. Gruene, T. Wolfram, K. Pelzer, R. Schlögl, A. Trunschke, *Catal. Today* **2010**, *157*, 137–142.

[119] Y.-M. Liu, Y. Cao, N. Yi, W.-L. Feng, W.-L. Dai, S.-R. Yan, H.-Y. He, K.-N. Fan, *J. Catal.* **2004**, *224*, 417–428.

[120] S. A. Karakoulia, K. S. Triantafyllidis, G. Tsilomelekis, S. Boghosian, A. A. Lemonidou, *Catal. Today* **2009**, *141*, 245–253.

[121] G. Martra, F. Arena, S. Coluccia, F. Frusteri, A. Parmaliana, *Catal. Today* **2000**, *63*, 197–207.

[122] O. Ovsitser, E. V. Kondratenko, *Catal. Today* **2009**, *142*, 138–142.

[123] C. Hess, J. D. Hoefelmeyer, T. D. Tilley, *J. Phys. Chem. B* **2004**, *108*, 9703–9709.

[124] M. Bañares, M. Martınez-Huerta, X. Gao, J. Fierro, I. Wachs, *Catal. Today* **2000**, *61*, 295–301.

[125] M. D. Argyle, K. Chen, C. Resini, C. Krebs, A. T. Bell, E. Iglesia, *Chem. Commun.* **2003**, 2082–2083.

[126] D. Nitsche, C. Hess, *Catal. Commun.* **2014**, *52*, 40–44.

[127] *Metal Oxide Catalysis*, (Eds.: S. D. Jackson, J. S. J. Hargreaves), Wiley-VCH Verlag GmbH & Co. KGaA, Weinheim, Germany, **2008**.

[128] D. Nitsche, Dissertation, Technische Universität Darmstadt, Darmstadt, **2014**.

[129] C. Resini, T. Montanari, G. Busca, J.-M. Jehng, I. E. Wachs, *Catal. Today* **2005**, *99*, 105–114.

[130] J. Martin, *J. Raman Spectrosc.* **1985**, *16*, 139–142.

[131] X. Gao, S. R. Bare, B. M. Weckhuysen, I. E. Wachs, *J. Phys. Chem. B* **1998**, *102*, 10842–10852.

[132] S. Xie, E. Iglesia, A. T. Bell, *J. Phys. Chem. B* **2001**, *105*, 5144–5152.

[133] M. Schraml-Marth, A. Wokaun, M. Pohl, H.-L. Krauss, *J. Chem. Soc. Faraday Trans.* **1991**, *87*, 2635.

[134] R. L. Flurry, *J. Mol. Spectrosc.* **1975**, *56*, 88–92.

[135] T. Shimanouchi, *Tables of Molecular Vibrational Frequencies Consolidated. Volume I,* **1972**.

[136] G. Magnotti, U. KC, P. L. Varghese, R. S. Barlow, *J. Quant. Spectrosc. Radiat. Transf.* **2015**, *163*, 80–101.

[137] *Characterization and chemical modification of the silica surface*, 2. impr, (Eds.: E. F. Vansant, P. van der Voort, K. C. Vrancken), Elsevier, Amsterdam, **1997**.

[138] A. Kämper, A. Auroux, M. Baerns, *Phys. Chem. Chem. Phys.* **2000**, *2*, 1069–1075.

[139] S. Klokishner, O. Reu, G. Tzolova-Müller, R. Schlögl, A. Trunschke, *J. Phys. Chem. C* **2014**, *118*, 14677–14691.

[140] M. V. Martínez-Huerta, X. Gao, H. Tian, I. Wachs, J. Fierro, M. Bañares, *Catal. Today* **2006**, *118*, 279–287.

[141] G. G. Cortez, M. A. Bañares, *J. Catal.* **2002**, *209*, 197–201.

[142] A. Brückner, P. Rybarczyk, H. Kosslick, G.-U. Wolf, M. Baerns, *Stud. Surf. Sci. Catal.* **2002**, *142*, 1141–1148.

[143] K. Wang, S. Ji, X. Shi, J. Tang, *Catal. Lett.* **2009**, *129*, 156–162.

[144] H. E. Howard-Lock, B. P. Stoicheff, *J. Mol. Spectrosc.* **1971**, *37*, 321–326.

[145] C. Nederlof, G. Talay, F. Kapteijn, M. Makkee, *Appl. Catal. A* **2012**, *423-424*, 59–68.

[146] M. A. Haija, Y. Romanyshyn, A. Uhl, H. Kuhlenbeck, H.-J. Freund, *Top. Catal.* **2017**, *60*, 413–419.

[147] J. Liu, F. Mohamed, J. Sauer, *J. Catal.* **2014**, *317*, 75–82.

[148] A. Held, J. Kowalska-Kuś, K. Nowińska, *J. Catal.* **2016**, *336*, 23–32.

[149] J. L. Callahan, R. K. Grasselli, *AIChE J.* **1963**, *9*, 755–760.

[150] C. Schilling, A. Hofmann, C. Hess, M. V. Ganduglia-Pirovano, *J. Phys. Chem. C* **2017**, *121*, 20834–20849.

[151] Z. Wu, A. J. Rondinone, I. N. Ivanov, S. H. Overbury, *J. Phys. Chem. C* **2011**, *115*, 25368–25378.

[152] C. Schilling, C. Hess, *J. Phys. Chem. C* **2018**, *122*, 2909–2917.

[153] V. V. Pushkarev, V. I. Kovalchuk, J. L. d'Itri, *J. Phys. Chem. B* **2004**, *108*, 5341–5348.

[154] C. Penschke, J. Paier, J. Sauer, *The Journal of Physical Chemistry C* **2013**, *117*, 5274–5285.

[155] C. Popa, M. V. Ganduglia-Pirovano, J. Sauer, *J. Phys. Chem. C* **2011**, *115*, 7399–7410.

[156] T. Kropp, J. Paier, J. Sauer, *J. Am. Chem. Soc.* **2014**, *136*, 14616–14625.

[157] T. Kropp, J. Paier, J. Sauer, *J. Catal.* **2017**, *352*, 382–387.

[158] X.-P. Wu, X.-Q. Gong, *J. Am. Chem. Soc.* **2015**, *137*, 13228–13231.

[159] A. Beste, S. H. Overbury, *J. Phys. Chem. C* **2015**, *119*, 2447–2455.

[160] A. Laachir, V. Perrichon, A. Badri, J. Lamotte, E. Catherine, J. C. Lavalley, J. El Fallah, L. Hilaire, F. Le Normand, E. Quéméré, G. N. Sauvion, O. Touret, *J. Chem. Soc. Faraday Trans.* **1991**, *87*, 1601–1609.

[161] C. Schilling, C. Hess, *ACS Catal.* **2019**, *9*, 1159–1171.

[162] C. Schilling, M. V. Ganduglia-Pirovano, C. Hess, *J. Phys. Chem. Lett.* **2018**, *9*, 6593–6598.

[163] L. Abello, E. Husson, Y. Repelin, G. Lucazeau, *J. Solid State Chem.* **1985**, *56*, 379–389.

[164] Y. Repelin, E. Husson, L. Abello, G. Lucazeau, *Spectrochim. Acta A* **1985**, *41*, 993–1003.

[165] S. Xie, E. Iglesia, A. T. Bell, *Langmuir* **2000**, *16*, 7162–7167.

[166] C. Hess, *Surf. Sc.* **2006**, *600*, 3695–3701.

[167] J.-M. Jehng, G. Deo, B. M. Weckhuysen, I. E. Wachs, *J. Mol. Catal. A: Chem.* **1996**, *110*, 41–54.

[168] A. E. Lewandowska, M. Calatayud, F. Tielens, M. A. Bañares, *J. Phys. Chem. C* **2011**, *115*, 24133–24142.

[169] A. E. Lewandowska, M. Calatayud, F. Tielens, M. A. Bañares, *J. Phys. Chem. C* **2013**, *117*, 25535–25544.

[170] A. Badri, C. Binet, J.-C. Lavalley, *J. Chem. Soc. Faraday Trans.* **1997**, *93*, 1159–1168.

[171] C. Yang, F. Bebensee, A. Nefedov, C. Wöll, T. Kropp, L. Komissarov, C. Penschke, R. Moerer, J. Paier, J. Sauer, *J. Catal.* **2016**, *336*, 116–125.

[172] H. Song, X. Bao, C. M. Hadad, U. S. Ozkan, *Catal. Lett.* **2011**, *141*, 43–54.

[173] D. R. Mullins, S. D. Senanayake, T.-L. Chen, *J. Phys. Chem. C* **2010**, *114*, 17112–17119.

[174] M. Li, Z. Wu, S. H. Overbury, *J. Catal.* **2013**, *306*, 164–176.

[175] A. Yee, S. J. Morrison, H. Idriss, *J. Catal.* **1999**, *186*, 279–295.

[176] A. Siokou, R. M. Nix, *J. Phys. Chem. B* **1999**, *103*, 6984–6997.

[177] T. Kropp, J. Paier, *J. Phys. Chem. C* **2014**, *118*, 23690–23700.

[178] Z. Wu, M. Li, D. R. Mullins, S. H. Overbury, *ACS Catal.* **2012**, *2*, 2224–2234.

[179] C. Huang, Z.-Q. Wang, X.-Q. Gong, *Chin. J. Catal.* **2018**, *39*, 1520–1526.

[180] S. Dogra Pandey, J. Singh, K. Samanta, N. Dilawar Sharma, A. K. Bandyopadhyay, *J. Nanomater.* **2015**, *2015*, 1–6.

List of abbreviations

$\mathbf{Al_2O_3}$	aluminium oxide
C	carbon
$\mathbf{CaF_2}$	calcium fluoride
CCD	charge-coupled device
$\mathbf{CeO_2}$	cerium dioxide
$\mathbf{CH_4}$	methane
$\mathbf{C_2H_5}$	ethane
$\mathbf{C_2H_4}$	ethene
$\mathbf{C_3H_8}$	propane
$\mathbf{C_3H_6}$	propene
$\mathbf{CO_2}$	carbon dioxide
CO	carbon monoxide
DFT	density functional theory
DH	dehydrogenation
DRIFT	diffuse reflectance infrared Fourier-transform spectroscopy
EPR	electron paramagnetic resonance
FB	fluidised bed
FCC	fluid-catalytic-cracking
FID	flame ionization detector
FTIR	Fourier-transform infrared spectroscopy
GC	gas chromatography
GHG	greenhouse gas
GHSV	gas hourly space velocity
$\mathbf{H_2}$	hydrogen
He	helium
IPCC	Intergovernmental Panel on Climate Change
KBr	potassium bromide
KM	Kubelka-Munk
$\mathbf{N_2}$	nitrogen
$\mathbf{O_2}$	oxygen
ODH	oxidative dehydrogenation
RR	resonance Raman
RT	room temperature
SBA-15	Santa Barbara Amorphous-15

SHG	second harmonic generation
SiO_2	silicon dioxide
TCD	thermal conductivity detector
THG	third harmonic generation
TiO_2	titanium dioxide
TOF	turn over frequency
UV	ultraviolet
V	vanadium
vis	visible
XPS	x-ray photoelectron spectroscopy
ZrO_2	zirconium dioxide

List of symbols

CB	carbon balance
$\vec{E}$	electric field
h	Planck constant
$\hbar$	Dirac constant
n	amount of substance
q	normal coordinate
S	selectivity
X	conversion
α	polarisability
λ	wavelength
μ	dipole moment
ν	frequency
Ψ	electronic wavefunction
ω	angular frequency

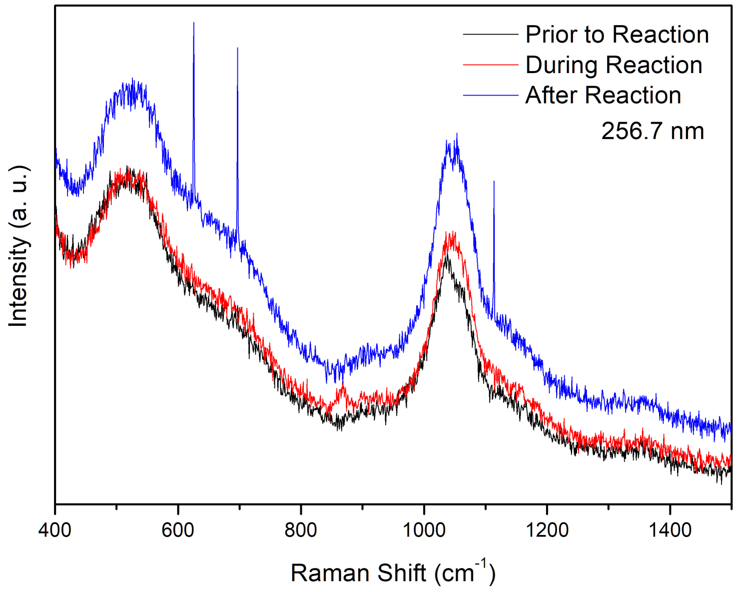

Figure 1.1: Raw data of the 256.7 nm *operando* Raman experiment for the 0.6 VO_x/SBA-15 catalyst prior to (black), during (red), and after (blue) propane ODH recorded at 409°C. Reaction conditions consisted of 14% C_3H_8 / 12% O_2/ 74% He at a total flow of 36 ml_n/min.

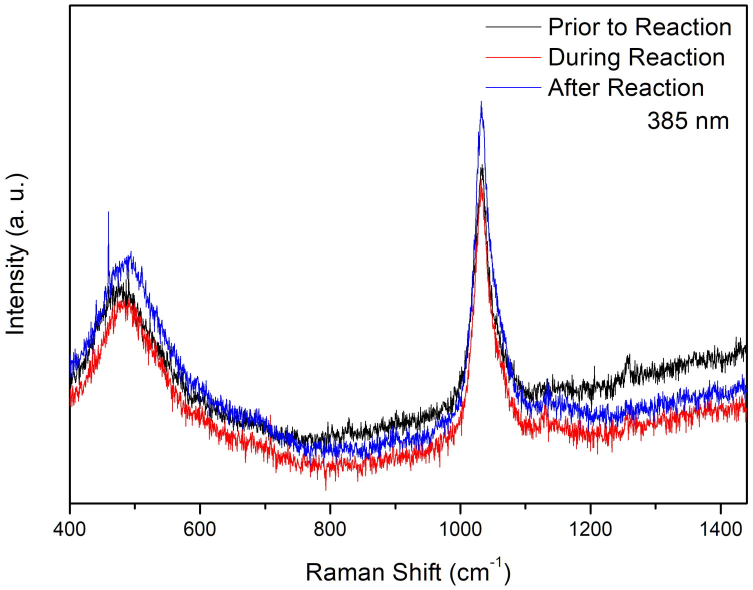

Figure 1.2: Raw data of the 385 nm *operando* Raman experiment for the 0.6 VO_x/SBA-15 catalyst prior to (black), during (red), and after (blue) propane ODH recorded at 409°C. Reaction conditions consisted of 14% C_3H_8 / 12% O_2/ 74% He at a total flow of 36 ml_n/min.

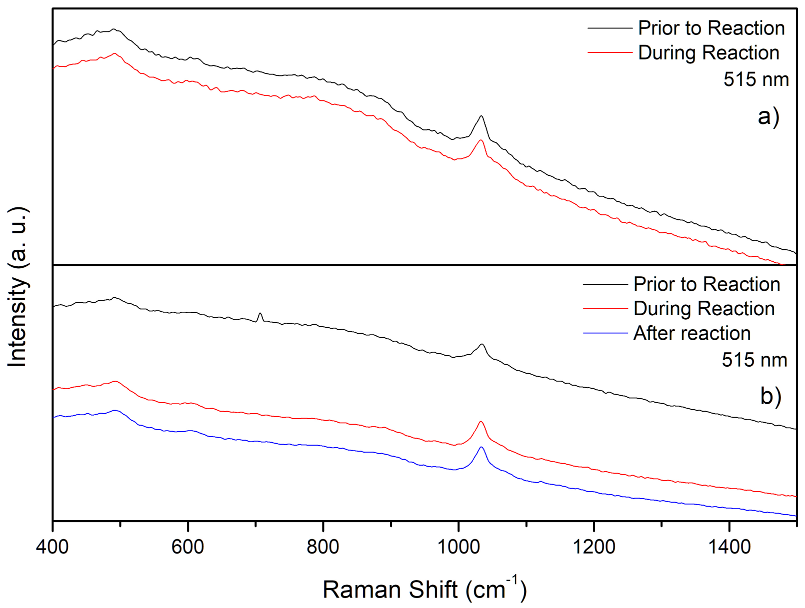

Figure 1.3: Raw data of the a) 515 nm interference experiment and b) *operando* Raman experiment for the 0.6 VO_x/SBA-15 catalyst prior to (black), during (red), and after (blue) propane ODH recorded at 409°C. The feed during the *operando* Raman experiment consisted of of 14% C_3H_8 / 12% O_2/ 74% He at a total flow of 36 ml$_n$/min, during the interference experiment of 12.5% C_3H_8 / 12.5% O_2 /75% He at a total flow: 40 ml$_n$/min.

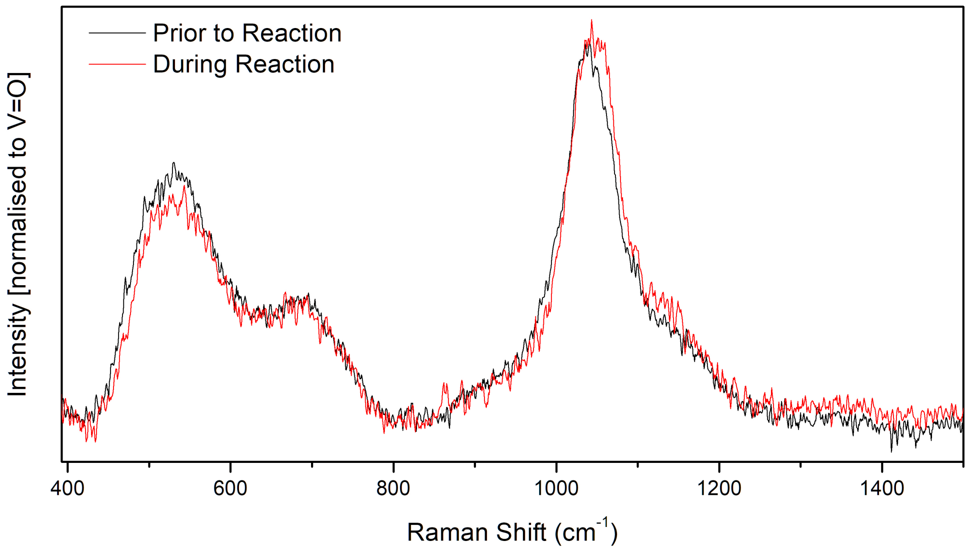

Figure 1.4: *Operando* Raman spectra of the 0.6 VO_x/SBA-15 catalyst prior to (black) and during (red) propane ODH recorded at 409°C. Spectra were taken from the interference experiment and normalised to V=O. The feed during reaction conditions consisted of 12.5% C_3H_8 / 12.5% O_2 /75% He. The spectra point to the reproducibility of results obtained under *operando* conditions.

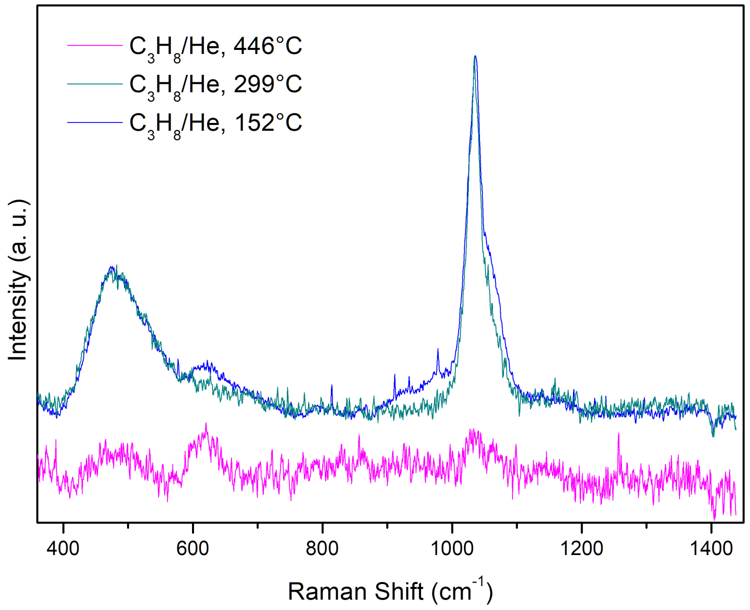

Figure 1.5: *In situ* 385 nm Raman spectra of the 0.6 VO_x/SBA-15 catalyst under propane reducing conditions at different temperatures. The feed consisted of 12.5% C_3H_8/ 87.5% He. Spectra were depicted with an offset. The spectral changes between 152 and 299°C are probably due to the presence of water.

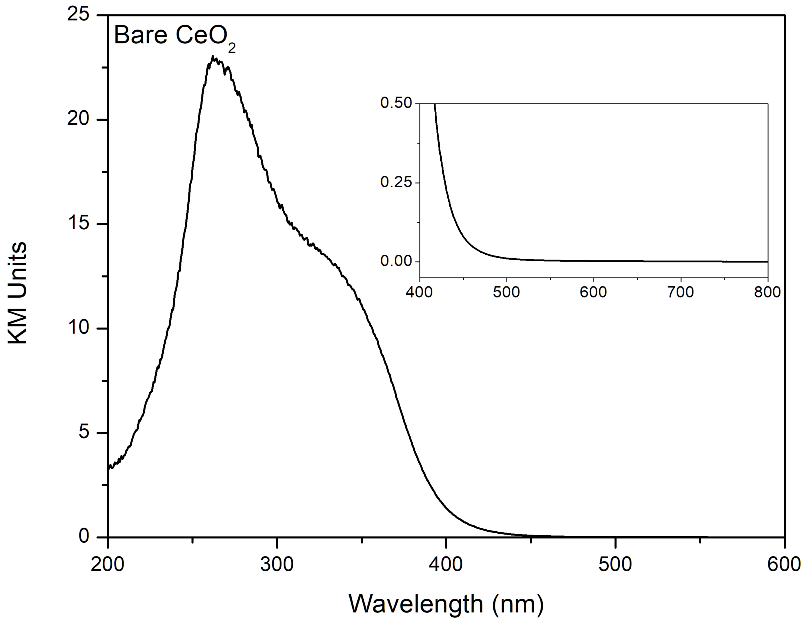

Figure 1.6: *In situ* UV-vis spectrum of the CeO_2 catalyst recorded in 8% O_2/ 92% N_2 flow at 100°C. The inset gives an enlarged view of the visible region of the spectrum.

B Curriculum vitae

Personal Details

Name:	Simone Erika Rogg
Date of Birth:	11.08.1990
Place of Birth:	Würzburg, Germany

Education

01/2017-04/2020	Technische Universität Darmstadt PhD in Physical Chemistry
03/2014-03/2016	University of Applied Sciences RheinMain Master of Science programme in Applied Physics
10/2009-03/2014	University of Applied Sciences Munich Bachelor of Science programme in Engineering Physics
09/2000-07/2009	St.-Ursula Schule Würzburg High School Graduation Certificate (Abitur)

Professional Experience

10/2012-06/2013	Internship in the R&D Department of the Medium Voltage and Systems Division of Siemens Queretaro, Mexico. Supported with the scholarship from the Federal Ministry of Education and Research, GIZ (Deutsche Gesellschaft für internationale Zusammenarbeit).

(S. Rogg)